ROMA TRE
UNIVERSITÀ DEGLI STUDI

SCUOLA DOTTORALE IN INGEGNERIA MECCANICA E INDUSTRIALE

XXIII CICLO

Experimental Investigation of the Near-Field Pressure Fluctuations of a Compressible Round Jet

Silvano Grizzi

A.A. 2010/2011

Tutor: Prof. Roberto Camussi

Coordinatore: Prof. Edoardo Bemporad

Index

1 Introduction

The commercial airline industry is one of the largest global industries and affects many aspects of daily life. The air transport has a significant environmental impact on the residential zones and the continuous expansion of the urban areas near the airports makes necessary the limitations of the noise pollution. The problem of noise generation by turbulent compressible jets has been of great interest since the early 1950s with the introduction of jet engines in commercial aircraft and even later with the adoption of high by-pass ratio turbofan engines. Since that time, considerable research activity has been undertaken to understand the generation and propagation of jet noise, as well as to devise techniques for its reduction. The noise that affects the inhabitants of the urban areas around the airports is called as Community Noise (see Figure 1) and is submitted to strictly laws; the noise that affects the passengers is called Cabine Noise (see Figure 1) and is also a critical parameter that forces a massive use of acoustic-absorbent materials inside the aircrafts. These strict limitations bring to a more accurate investigation of the jet noise production mechanisms evolving equally theoretical, experimental and numerical aeroacoustics research. Deeper jet noise knowledge brings to the realization of less noisy aircrafts; this topic becomes also fundamental for the newest realization of aircrafts using composite materials that protects less the passengers from the noise than the metals.

The term “Jet Noise” is frequently used to describe the total noise emanating from an aircraft exhaust system; studies have shown that this total noise is composed of several parts. The most fundamental of these is due to the turbulent mixing of the jet exhaust with the ambient fluid downstream of the nozzle exit section. This “Jet Mixing Noise” is the most difficult component to control and to eliminate.

The jet mixing noise is one of the main sources of the aircraft engine total noise (see Figure 2) and it has historically received the most attention since the Lighthill’s works (Lighthill 1952

& 1954). The Lighthill's papers have marked the beginning of jet noise research and the birth of the "Aeroacoustics" research area. In the Lighthill's analogy the exact equations of fluid motion are recast as an inhomogeneous wave equation, with the inhomogeneous part that comprises all the non-linearities. Lighthill recognized that this formulation is particularly appropriate to describe the jet noise; the flow is described using this analogy as a freely propagating sound-field driven by a confined region of intense rotational motion.

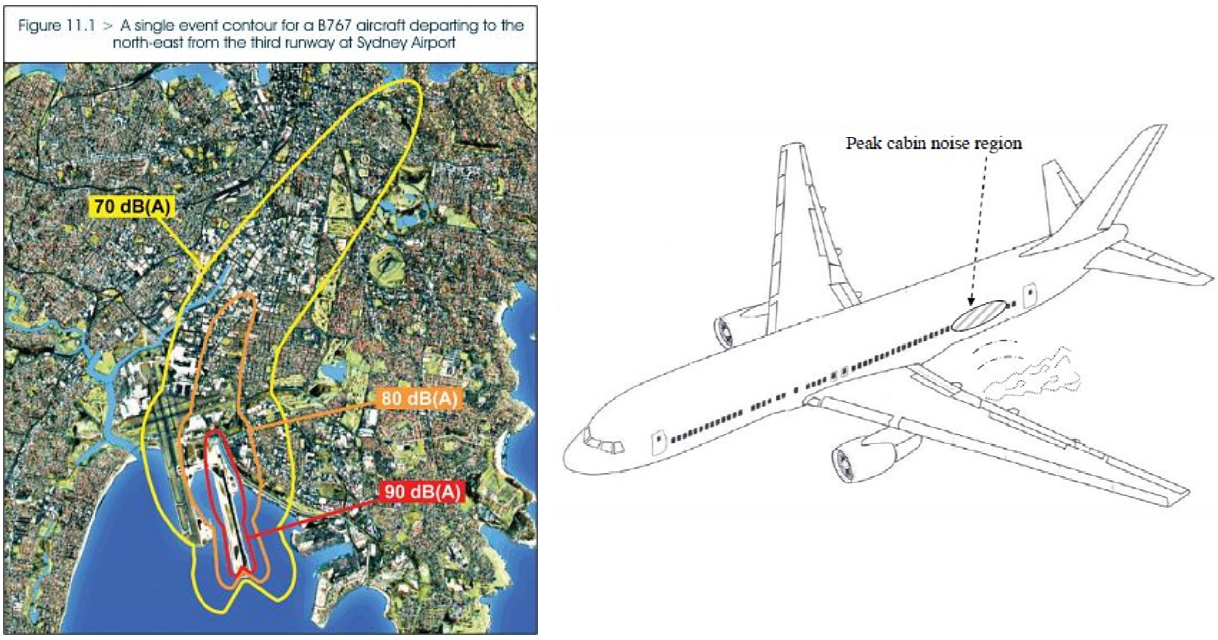

Figure 1: Community Noise distribution for a single takeoff (Left) and Cabine Noise peak region (Right)

The community noise is also defined as far-field noise and is well described by the mentioned acoustic models. In the jet noise the convection of the sources downstream the flow has the effect to give a significant directivity to the jet noise. In fact, the far-field noise presents a maximum angular direction, with a maximum direction around 140 - 150° (defining 180° downstream the jet axis).

As pointed out by Michalke and Fuchs (1975), the knowledge of the near field pressure, intimately related to the hydrodynamic velocity fluctuations, can clarify the process underlying the propagation of acoustic waves to the far field. However, as reported in many review papers (e.g. those by Lilley, 1995, Tam, 1998, and the recent one by Jordan & Gervais,

2008), considerable efforts have been devoted to the characterization, prediction and modeling of the far-field noise along with the attempt of relating the far field acoustics with the hydrodynamic near-field.

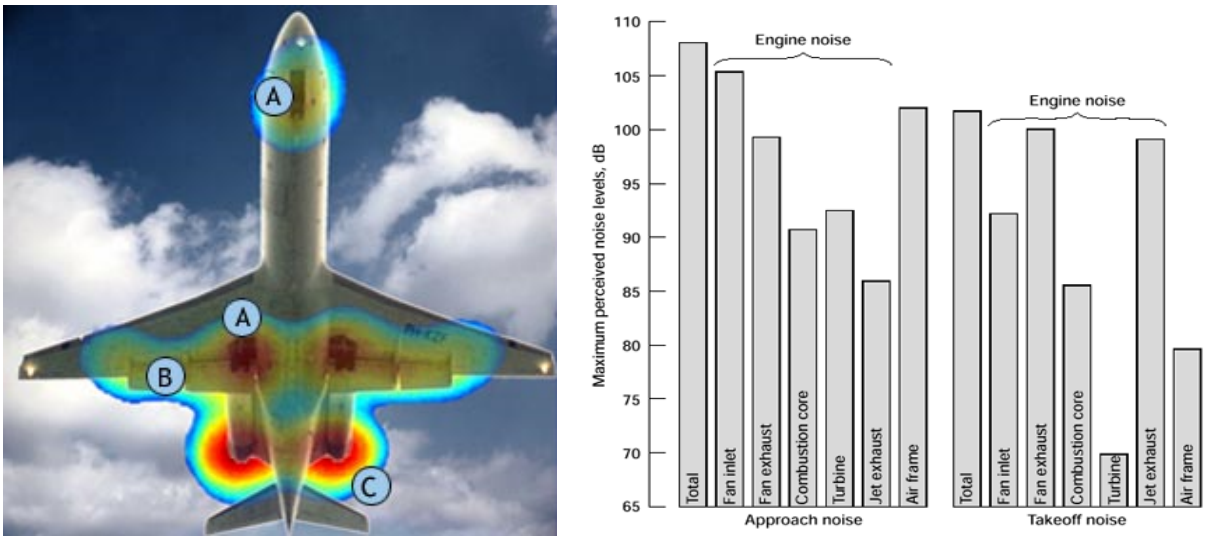

Figure 2: Noise distribution on an aircraft during the takeoff (Left) and influence of the noise sources during approach and takeoff (Right): the Jet exhaust is one of the main sources during the takeoff phase.

The near-field noise, that influences passengers' comfort, on the contrary, seems to be different and not so well described by acoustics models for the presence of other pressure fluctuations that are not sound because they don't have all the features of the sound. The near pressure field investigation of an unbounded jet has been the subject of a considerable number of experimental and theoretical investigations over the past 60 years to understand flow-dynamics and sound production and propagation mechanisms.

1.1 Objectives

The main aim of this study is the investigation of the near-field noise that is considered nowadays interesting for the possibility to locate the noise source.

To perform this investigation some objectives have been pursued:

- A jet noise facility has been designed and realized.
- The jet facility has been qualified and compared with literature studies.
- The near-field pressure fluctuations have been analyzed and filtered to separate the sound contribution; to perform this, a novel filtering procedure has been developed.
- Synchronized measurements of velocity and acoustic fields have been carried out to locate the noise generation zones of the jet.

This thesis is organized as follows:

The Chapter 2 gives an overview of the jet properties starting from the turbulent characteristics related to the jet noise production mechanisms, describing models and theories from the Lighthill's analogy to the recent developments.

The Chapter 3 describes the analysis and filtering methods with particular attention to the wavelet-based algorithms. This represents a novel approach in aeroacoustics studies.

The Chapter 4 presents the experimental setup and the measurement techniques used to study the jet; the used hardware is analyzed to define its application limits and to quantify its accuracy.

The Chapter 5 presents both flow-dynamic and acoustic qualification of the jet and the results are compared with literature data.

The Chapter 6 shows the near-field pressure fluctuations comparing the filtered and non-filtered data with the far-field and with literature data.

In the Chapter 7 the identification of noise production zones is performed correlating the velocity and the acoustic data; a comparison also with some previous studies is done.

At the end the Chapter 8 presents some conclusions and suggestions for future works.

2 Turbulent and Acoustic Jet Properties

The noise produced by a jet is governed by the turbulence flow from it; the basic mechanisms involved in the jet noise production are still not understood. The complex nature of the turbulence is dependent mainly by the three dimensional character of the velocity field, its non-linearity and its random and intermittent variation. The statistical models for the turbulence introduce simplifications that don't allow an accurate understanding of some noise production mechanisms. In turbulence models it is impossible to predict the exact value of fluctuation at a given moment but it was accepted in the research that the average values for particular locations in the flow should remain constant; in this manner not all scales of the turbulence can be viewed. For this reason, for example, the identification of intermittent large scale structures is difficult for any time averaging analysis technique. However the statistical properties of turbulence have provided great information on the nature of a turbulent flow and are useful for the prediction of its noise generation.

A jet airflow produces pressure fluctuations either in the form of regular eddies or an irregular turbulent flow. These pressure fluctuations can be detected and measured by a microphone or the human ear; only a relatively small part of the energy of these fluctuations can be called sound. Most of the pressure fluctuations, for example eddies, are convected in the flow at the flow speed and don't propagate at the typical sound speed. These hydrodynamic pressure fluctuations transfer a certain amount of their kinetic energy into radiated sound. An examination of the radiated sound field reveals that is comprised of a broadband spectrum so all turbulent scales must contribute to the propagating noise. However the large and small scales of turbulence may behave differently and the exact mechanisms of sound generation from these fluctuations are not yet completely understood.

A key point of the aeroacoustics research is the identification of noise production mechanisms from each turbulent structure during its evolution in the flow field. The full understanding improves the active noise control and reduction modifying the flow turbulent characteristics. The purpose of this work is to correlate the pressure fluctuations to some generation mechanisms in the flow; for this reason an introductive description of jet properties is necessary.

2.1 The Turbulent Jet

A jet is a flow that enters in a stationary fluid. This interaction brings to intense mixing and creates a shear layer. Going downstream the shear layer widens through the axis of the jet; the conic zone between the exit section and the point where the shear layer meet the jet axis is the potential core; in this zone the velocity maintains constant and it is extended to a distance of 3 – 5 diameters (Rajaratnam 1976). In the potential core the axial velocity profiles starts with a top-hat shape and evolves maintaining the maximum velocity value equal to the jet velocity, the velocity gradients between the jet core and the external fluid becoming smooth moving downstream (see Figure 3). Beyond this distance, the turbulence produced by the shear layers from the border of the jet reaches the jet centreline and dissipates the velocity; after this point a transition zone begin and changes quickly to a fully developed flow zone. The structure of a jet is shown in the Figure 4.

In the fully developed region the velocity and turbulence profiles are comparable and are known as self-similarity profiles. In fact the velocity and turbulence radial profiles, opportunely scaled, can be perfectly overlapped as observed by Trupel (1926).

As previously mentioned the axial velocity is constant inside the potential core, so, along the jet axis, the non-dimensional axial velocity has a constant profile until the end of the core, after that it decreases with a 1/X law (Eq. 1); according to literature the decreasing factor is usually between 5 and 7.5 (see Tab 1).

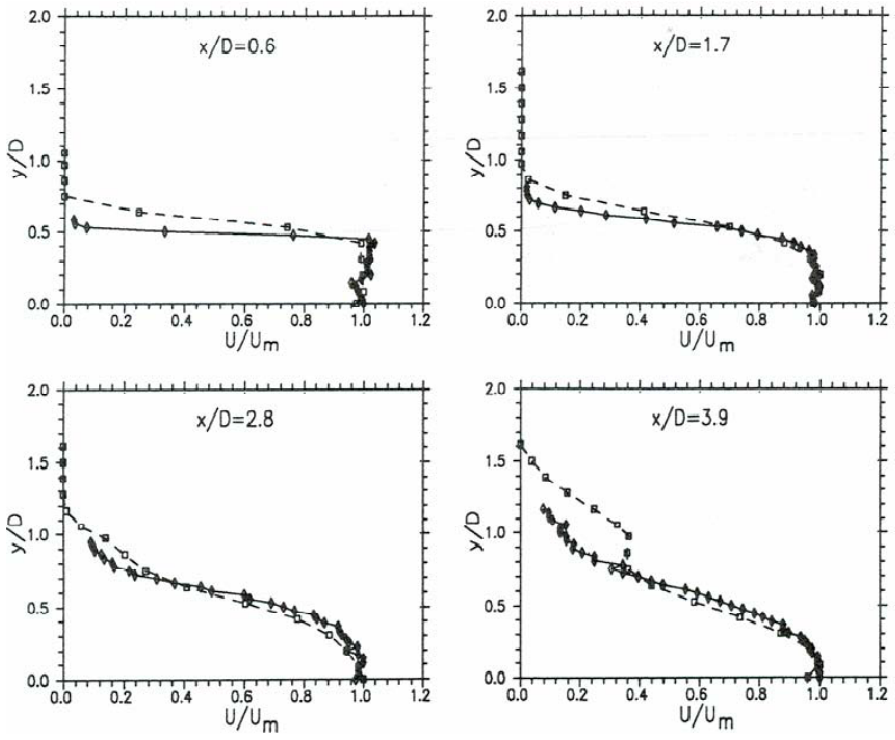

Figure 3: Potential Core velocity profiles. (Cenedese et Al. 1994)

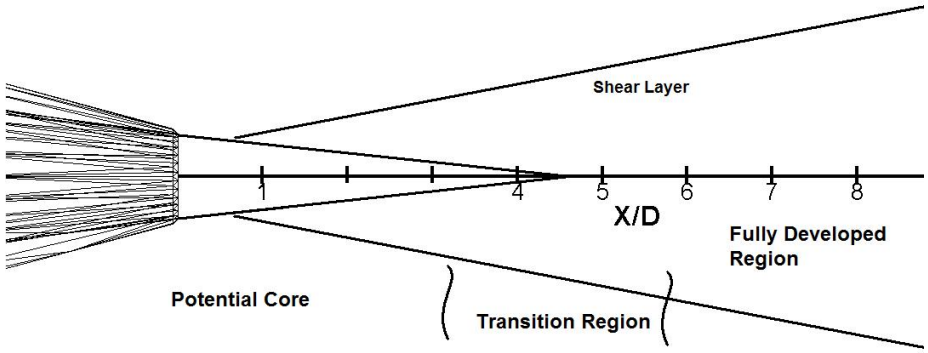

Figure 4: Structure of a Jet.

The potential core end is located where the axial Kurtosis has a maximum, downstream this point the jet becomes fully turbulent and the velocity profiles became self-similar. Many experimental data and empirical solutions are available to compare the jet profiles as Tolmien, Goertler type (Rajaratnam 1976) or Integral Solution (Agrawal e Prasad 2003).

These characteristics are useful to verify that the jet studied in the presented work has been designed correctly.

$$\frac{U}{U_j} = C * \frac{D}{X} \qquad \text{Eq. 1}$$

Reference	C coefficient
Trupel (1926)	7.32
Hinze Zijne (1949)	6.3
Albertson et Al. (1950)	6.39
Grizzi et Al. (2006)	7.47
Panchapakesan e Lumley (1993)	6.06
Hussein et Al. (1994) HW	5.9
Hussein et al. (1994) LDA	5.8
Grandmaison (1982)	5.43
Becker (1967)	5.59
Ebrahimi (1977)	5.78
So (1990)	5.51
Dowling (1990)	5.11

Tab 1: Axial velocity decreasing coefficients.

In the self-similarity zone the velocity and turbulence profiles have to be scaled using as parameters the maximum local axial velocity (U_m) and the half jet aperture radius (b), which is defined as the distance from the axis where the local velocity is half of the local maximum velocity. (see Figure 5) Moreover, also the turbulence profiles are self-similar as the axial Reynolds stress u'^2 is scaled with respect to U_m^2 (see Figure 6).

Another important feature is the state of the boundary layer in the nozzle that, just at the exit section, can be laminar or turbulent. In this work it has been checked that the boundary layer is turbulent.

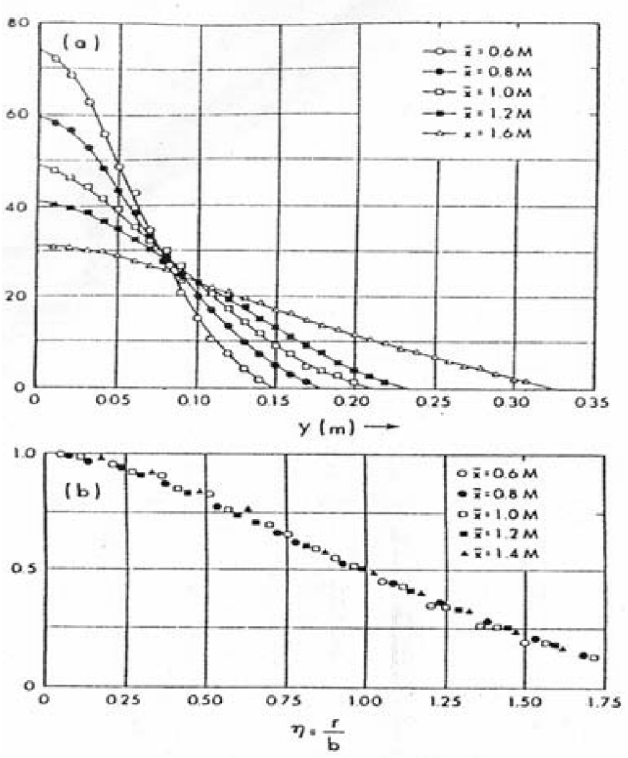

Figure 5: Dimensional (top) and non-dimensional or self-similar (bottom) velocity profiles (Abramovich 1963)

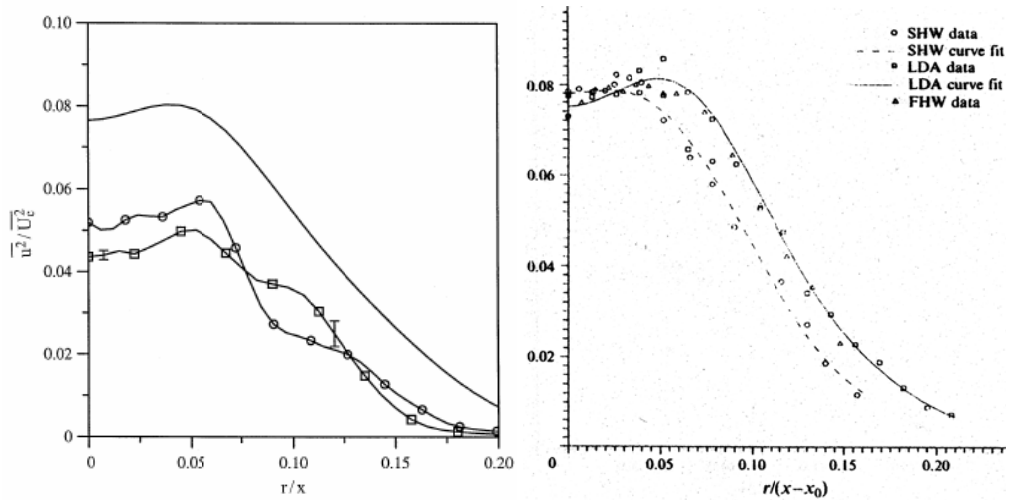

Figure 6: u'/Um^2 self- similar profiles: on the left Weisgraber e Liepmann (1998); on the right Hussein et al. (1994).

2.2 Overview on the Jet Noise

Several regions in the jet structure are interesting for the noise production but there is a lot of uncertain in the physical mechanisms of noise production. In the Lighthill's works (1952 and 1954) the sources were modelled as freely-convected quadrupoles; during the 1970s large scale structures were discovered in the shear layer and this structures' noise production were studied. Juvé (Juvé et Al. 1980) shows that these structures have a significant intermittency; he demonstrates also that the 50% of the noise is produced in the 10 – 20% of the total time. Juvé suggests also that the noise emissions can be placed also upstream of these structures where the external fluid was entrained. It has been shown that the breakdown of the structures at the end of potential core is a significant mechanism of noise emission (Guj et Al. 2003, Hileman et Al. 2005)

There are other phenomena that affect the noise radiation from the sources in the jet; the noise sources are convected in a high speed flow affecting the directivity of the radiated noise. In addition the noise must pass through the shear layer and suffers of refraction effects by the velocity gradients generating the well-known "cone of relative silence" (Tanna 1977). Other characteristic of the noise is the different spectral content as a function of the direction. Tam et Al. (1996 and 1999) proposed that the fine-scale turbulence is responsible for the noise at 90° and the large scale structures generates the noise at 150°, defining 180° direction as the jet axis downstream; other researchers explained on the contrary the different spectral contents in the far-field as a different directivity that affects different scale sources.

2.3 The Acoustic Analogy

The Lighthill's Acoustic Analogy was developed in the early 1950s (Lighthill 1952 – 1954); this works represents the beginning of aeroacoustics science and allows to made acoustic predictions of turbulent flow for the first time. In the Lighthill's work a small part of the fluid is occupied by the main flow that generates fluctuations, the rest of the fluid is only interested by the acoustic propagation. Lighthill recasts the exact equations of fluid motion in the form of an inhomogeneous wave equation, whose inhomogeneity comprises all the non-linearities of the Navier-Stokes equations. This equation describes freely propagating linear disturbances which are driven by the dynamics described by a non-linear term on the right-hand side (Eq. 3).

$$\frac{\partial^2 \rho'}{\partial t^2} - \ c_0^2 \nabla^2 \rho' = \frac{\partial^2 T_{ij}}{\partial x_i \partial x_j} \qquad \text{Eq. 3}$$

Lighthill recognised that this form is particularly well suited to the problem of the jet noise where the system is divided in a freely propagating sound field, which is driven by a confined region of intense rotational and non-linear motion.

The right-hand side term is the Lighthill tensor (Eq. 4) that incorporates sound generation, convection with the flow, propagation with variable speed and dissipation by conduction and viscosity (Lighthill 1952).

$$T_{ij} = \rho u_i u_j + \ [(p - p_0) - c_0^2(\rho - \rho_0)] * \delta_{ij} + \sigma_{ij} \qquad \text{Eq. 4}$$

From the previous equation, considering that the viscous dissipation is a very slow process and that the static pressure field variation is negligible in problems where the temperature is fairly uniform, the principal terms of sound generation are the Reynolds stresses $u_i u_j$. The modelling of this term in the Eq. 3 is one of the targets of the research. A model proposed by Ribner (1964) assumes homogeneous isotropic turbulence and the sources as a distribution of freely-convected quadrupoles with strength related to the two point correlation function of the Reynolds Stress; this requires detailed turbulence statistics to perform an accurate acoustic prediction. Unfortunately this source modelling is inadequate because does not

take into account the changes in radiation efficiency due to the interaction of the flow environment and the sources. Several new models and modifications to the Lighthill analogy were proposed during the years.

2.4 Recent Acoustic Theories

One of the most popular of this model is the one proposed by Tam and Aurialt (1999) and relates the local turbulent kinetic energy to the local pressure fluctuations of the small scale turbulence. This model is semi-empirical and relates the noise to the fine scale turbulence and not with the large scale structures. For this reason the two sources theory was subsequently introduced and attributes different spectral directivities to different sources.

All the presented models from the Lighthill or the Lilley approaches regard the small-scale component but only recent studies identify also large-scale mechanisms that generate pressure fluctuations. Coiffet et Al. (2006) shown experimentally the existence of vortex-pairing and wavy-wall type instabilities in the region upstream the end of the potential core and demonstrate that the production mechanism is linear. Kopiev and Chernyshev (1997) have provided an analytical demonstration of how the eigen-oscillations of a single vortex structure can constitute an octupole sound production mechanism, which presents directivity similar to the jet (Kopiev et A. 1999, 2006). There are also many studies that indicate as dominant sound production mechanisms the intermittent and violent collapses of the annular mixing layer at the end of the potential core. Juvé et Al.(1980) shown that the events in this region have high level of intermittency: the possible mechanisms are identified as the sudden decelerations near the end of the potential core, related to fluid entrainment on the upstream side of ring-like coherent structures. Other works as Guj et Al. (2003) or Hileman et Al. (2006) provided other experimental evidences for this sound production mechanism.

To summarize the different models, the jet noise was described as dependant by two distinct mechanisms: one related to small-scales, random eddies, which are compact, convected and

have a quadrupole behaviour; the other is related to the coherent flow dynamics, which can produces sound via-vortex pairing, vortex eigen-oscillations, quasi-irrotational instability or wavy-wall-like mechanisms and intermittent events in the transition region of the flow. Is unclear how the two mechanisms contribute differently to the sound directivity. Probably an angle-dependent frequency selection occurs depending by the interaction between the sound field and the flow dynamics.

2.5 Sound and Pseudo-Sound

The main objective of aeroacoustics is the comprehension of the physics of noise generation; the uncertain in the real noise sources contribution needs more experimental studies, for this reason many tests were conducted to locate the sources and the noise generation mechanisms; to accomplish the velocity information and sound measurement are correlated both in far-field and in near-field. As previously mentioned the near-field measurements, which are more useful for the sources localization, are affected by some-pressure fluctuations that are not sound. Howes (1960), Ffowcs-Williams (1992) and Ribner (1964) describe the presence of pressure fluctuations, called pseudo-sound, in the near-field that are not sound but are undistinguishable, using a microphone, from the sound. In fact, when sound is generated by an unsteady flow, only a small part of the energy associated with pressure fluctuations radiates as sound and the main pressure fluctuations masks sound field near the jet. A filtering method to separate sound from pseudo-sound is necessary to compare the far-field with the near-field noise and it is also useful for noise-control applications.

Ffowcs-Williams (1992) wrote:

"It is only when the pressure satisfies this equation (Equation of the waves) *that it is properly regarded as sound. Other pressure fluctuations, indistinguishable by a single microphone from proper sound, have been termed Pseudo Sound, only pseudo because they lack some essential characteristics of sound. They do not propagate through the fluid but are convected*

with the eddy structures in the flow, often in chaotic path and usually with a speed very much smaller than the sonic velocity."

The pseudo-sound is convected with eddies, it is the rotational part of the flow and do not propagate. Instead, the sound propagates but it is negligible when the pressure field is dominated by the pseudo-sound. The pseudo sound field decays very rapidly, usually with the inverse of the third power of the distance, and, at large distances, the pressure field reduces to the acoustics field (Howes 1960).

In the flow region, the pseudo-sound is the quasi-incompressible pressure fluctuations part and it is dominated by inertial effects rather than compressibility. Pseudo-sound is a solution of the Poisson's equation (Ribner 1964).

The sound is also present in the near field region, is described by wave equation and it is the irrotational part of the pressure field. When a measure is performed in the near-field the acoustical contribution is affected by the hydrodynamic one since a microphone is subjected to fluctuations both of the sound and of the pseudo-sound (Howes 1960).

Considering the different nature of the two parts an important task for a near-field measurement is the filtering of the two contributions from a near field signal. The pseudo-sound is associated to the convection of structures through the flow and for this reason carries information about the coherent structures. The remaining part is the sound and it is associated to the incoherent part of the pressure fluctuations. Ribner (1964) divides the pressure fluctuations **p'** into sound (**p'_0**) and pseudo-sound (**p'_1**) fluctuations:

$$P' = P'_0 + P'_1 \qquad \text{Eq. 2}$$

Also in Guitton et Al. (2007) the near pressure fluctuations of a jet are considered as a superposition of sound and pseudo-sound fields. When possible a filtering operation can divide the pressure fluctuations in the two contributions that, for the different nature of them, have different behaviours as the different propagation characteristics. Usually Fourier's based filters are used to distinguish the two parts but this is not efficient because, for its nature, this filtering is equivalent to a high-pass and low-pass filtering, in fact the Fourier transform is located only in the frequency domain. In the work of Tinney and Jordan

(2008) the acoustic-hydrodynamic filtering is performed starting from microphone array measurements and calculating the phase velocity of the signal on the array because *"no sound field can produce a subsonic phase velocity"* (Tinney and Jordan (2008).

Considering that sound and pseudo-sound may have energy to the same frequencies and filtering only in the frequency domain is not sufficient for a complete signal splitting. For this reasons a Wavelet filtering tool is more indicated, the Wavelet transform is located both in the frequencies both in the time domain (Graps 1995) and the signal splitting is possible considering the intermittency of events; in fact, using the wavelet, is possible to separate the intermittent events from the rest of the signal; the coherent structures pass through the microphone at intermittent intervals and the remaining signal is related only to the acoustic field. It must be remembered that the intermittent nature of the large scale structures in the velocity field is a noise generation mechanism (Juvé et Al. 1980; Tinney and Jordan 2008) but the intermittent nature of pressure fluctuations in the near-field is related on the contrary to the convection of the large scale structures and its nature is different by the sound, as will be demonstrated in the next chapter.

3 Wavelet Filtering

Classical statistical tools assume to have a homogeneous flow without discontinuities or intermittent events; a wavelet-based tool does not require such hypotheses. Wavelets are mathematical functions that cut up data into different frequency components, and then study each component with a resolution matched to its scale. They have advantages over traditional Fourier methods in analyzing physical situations where the signal contains discontinuities and sharp spikes. Wavelets are functions that satisfy certain mathematical requirements and are used in representing data or other functions, expanding or contracting the selected wavelet, also called *mother wavelet*, using an opportune scaling function, the algorithm can analyze the data both in time both in frequency domain and obtain the wavelet coefficients. The analyzed signal can be represented as a linear combination of the mother wavelet with these coefficients. Selecting an opportune threshold the original signal can be also divided in two parts obtaining two signals: one with the coefficients greater than the threshold and the other with coefficients lower than the chosen value (Graps 1995). Moreover the wavelet analysis locate the intermittency of events (Ruppert-Felsot et Al. 2009) and makes possible to separate the time history of these events from the rest of the signal. In turbulence the wavelet are successfully used for the identification of intermittent structures analyzing the velocities or the pressure fields, as in the works of Lee and Sung (2002) or Camussi et Al. (2008 and 2010).

3.1 Fourier Transform versus Wavelet Transform

The Fourier and the Wavelet transform have similar aspect, for example both decompose the signal in basis functions, that are sinus and cosines for the Fourier transform and the mother wavelet for the wavelet transform. Both describe the transformed signal with the

coefficients of the basis functions but the Fourier transform give only a description in the frequency domain (the windowed Fourier transform gives also a description in time domain but maintaining a uniform resolution as shown in Figure 7) on the contrary the wavelet transform, using very short-in-time functions and scaling them, decomposes the signal both in frequency both in scale domain. The wavelet transform in fact, with respect to the Fourier transform or the windowed Fourier transform, uses functions localized in space and this feature gives the possibility to describe the signal with a resolution that depends by the scale length of each event (see Figure 7). So the wavelet can isolate the discontinuities using very short basis functions and at the same time can offer a detailed frequency analysis using very long basis functions. These characteristics made of the wavelet transform the perfect tool to analyze signals that present intermittent or random events with discontinuities indicating also when a single event occurs and which frequencies or length scales it involves.

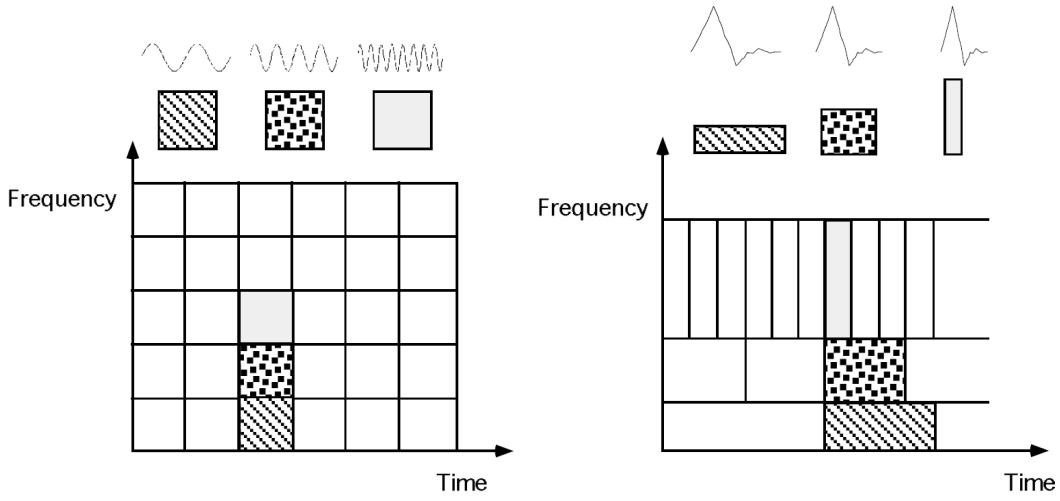

Figure 7: Time-frequency differences of the Windowed Fourier Transform (left) respect to the Wavelet Transform (right) (from Graps 1999)

Another difference is that the Fourier transform uses just sinus and cosines functions instead the wavelet has an infinite set of basis functions (see Figure 8).

In details the wavelet transform decomposes the signal in a set of coefficients resulting from the projection of a signal onto a basis of compact support functions (Eq. 3); the basis is composed by stretched (r) and shifted (t) versions of the mother wavelet Ψ.

$$w(r,t) = C_{\Psi}^{-1/2} r^{-1/2} \int_{-\infty}^{\infty} \Psi^* \left(\frac{t-\tau}{r}\right) p(\tau) d\tau \qquad \text{Eq. 3}$$

This decomposition leads to a description of the signal both in time and in frequency domain.

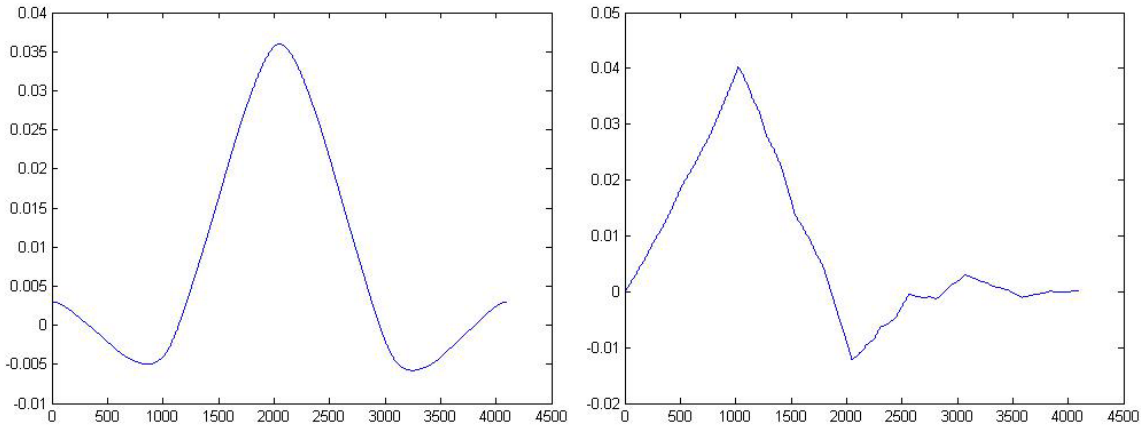

Figure 8: Example of wavelet mother functions: Coiflet 3 function (left) and Daubechies 6 function (right).

3.2 Wavelet Decomposition of Sound: A novel approach

The nature of the near-field pressure measurements, for the presence of the sound and pseudo-sound components, requires the development of a filtering algorithm that recognizes intermittent and random events separating them from the rest of the signal. As previously described the intermittent events are related to pressure fluctuations caused by coherent convected structures so there is the possibility that this part of the signal has a pseudo-sound nature; on the contrary the remaining part of the signal, that represents the incoherent part, could be only composed by sound. The verification of these hypotheses is a topic of the present work. Usually the separation of the sound from the other pressure

fluctuations is performed calculating the cross spectra and the phase velocities (Tinney and Jordan 2008) but a Fourier based method can't capture all the frequencies of intermittent and random events because this filtering method is similar to a pass-band filter; on the contrary the sound and pseudo-sound can exist at the same frequencies with different energies and the wavelets are the best tool to perform this filtering.

An orthogonal discrete wavelet transform is used to separate the coherent intermittent events from the rest of the signal and a verification of the correct threshold value is performed considering the different properties of which can be considered as sound and which is only pseudo-sound; in fact, an intermittent event is properly chosen when its LIM exceeds a threshold value because it is proportional to the energy of the event (Graps 1999).

The main algorithm is presented by Ruppert-Felsot et Al. (2009), the algorithm used to separate the coherent structures from the rest of the signal in a sort of de-noise filtering. In this algorithm the threshold, as demonstrated in Donoho & Johnstone (1994), to remove an additive Gaussian white noise is proportional to the variance of the noise [Eq. 4].

The variance of the noise in not known a priori, the first step threshold is set proportionally to the variance of the full signal [Eq. 4]. The signal is divided in a coherent and incoherent part using this threshold; the coherent part is described by the wavelet coefficients that exceed the given threshold. The next step threshold is evaluated using the variance of the incoherence part at the current step; the algorithm iterates until the wavelet coefficients became constant.

$$Thr_{n+1} = \sqrt{2\,\sigma_n^2\,ln\,N} \qquad \text{Eq. 4}$$

σ_n^2 is the variance on the incoherent signal at the n-pass, and *N* is the resolution of the signal acquisition. The time history signal of the coherent structures is obtained from the inverse wavelet transform of the coefficients that exceed the selected value; the rest of the total wavelet coefficients compose the noise part of the signal. To distinguish the coherent structure pressure fluctuations from the others in the near field is necessary to verify if the coherent and the incoherent signals has sound characteristics. A useful way to distinguish if a particular signal can be considered as sound or not is to verify its propagation velocity

(Tinney and Jordan 2008); to calculate the propagation velocity is necessary to have at least two contemporary signals from different measurements points with a known distance. The cross-correlation of this signal gives the elapsed time of a fluctuation between the two points and consequently the propagation velocity. A couple of microphones is put in the near-field, aligned with a known distance and with an angle respect to the jet axis to maintain parallel to the jet shear layer. Some measurements of the near-field pressure fluctuations can demonstrate such hypotheses on the sound and pseudo-sound; the filtering algorithm (Ruppert-Felsot et Al. 2009) is applied to this signals and each signal gives back two time histories for the coherent and the incoherent part. The cross-correlation of the parts of the signals from the two microphones verifies that the propagation velocity of the coherent part is lower respect the sound speed; instead the propagation velocity of the incoherent part is sonic or supersonic when the sound wave propagation direction isn't parallel to the microphones alignment (see Figure 9). From the cross-correlation is easy to calculate the propagation velocity of the incoherent signal (e.g. Figure 9):

$$V_i = \frac{D_m}{\tau_i} = \frac{0.014\ m}{3 * 10^{-5}\ s} = 466\ m/s$$

τ is the time lag between the time origin and the first correlation peak. The propagation velocity is greater than the sound speed as an effect of the misalignment of the wave propagation respect to the microphones axis and this is a first clue that the incoherent signals are sound. Making the same calculation for the coherent correlation time, it is obtained:

$$V_c = \frac{D_m}{\tau_c} = \frac{0.014\ m}{9.4 * 10^{-5}\ s} = 149\ m/s$$

This propagation velocity is lower than the sound speed (Tinney and Jordan 2008) and indicates that the coherent part of the signal is convected in the flow; we can consider it as Pseudo-Sound. The Figure 9 shows also the shape of the correlation functions, the coherent part has a correlation similar to the full signal part, and it means that in these measurement positions the pseudo-sound has a lot of energy; the shape of the blue line is large and has the characteristic shape of the correlation related to the coherent structures. Considering

the incoherent part (the red line) the peak is very thin with a similar Dirac shape with strong oscillations around the main peak, this is a typical characteristic of this part of the signal.

A further verification is possible comparing the probability density function of the <sound; incoherent> signal and of the <pseudo-sound; coherent>; as shown in the Figure 10 the pseudo-sound is asymmetric and has tails, is the PDF of coherent structures (Ruppert-Felsot et Al. 2009); on the contrary the PDF of the sound is very close to a perfect Gaussian distribution (Frisch and She 1991). The differences of the coherent and the incoherent signal are evident and indicate two different natures. The coherent pressure fluctuations have a typical convective velocity and the incoherent propagate with sound speed. This briefly described algorithm is efficient when the coherent part of the signal (or pseudo-sound) has more energy than the incoherent one (see Figure 9); these conditions are present in the zone nearest to the jet shear layer.

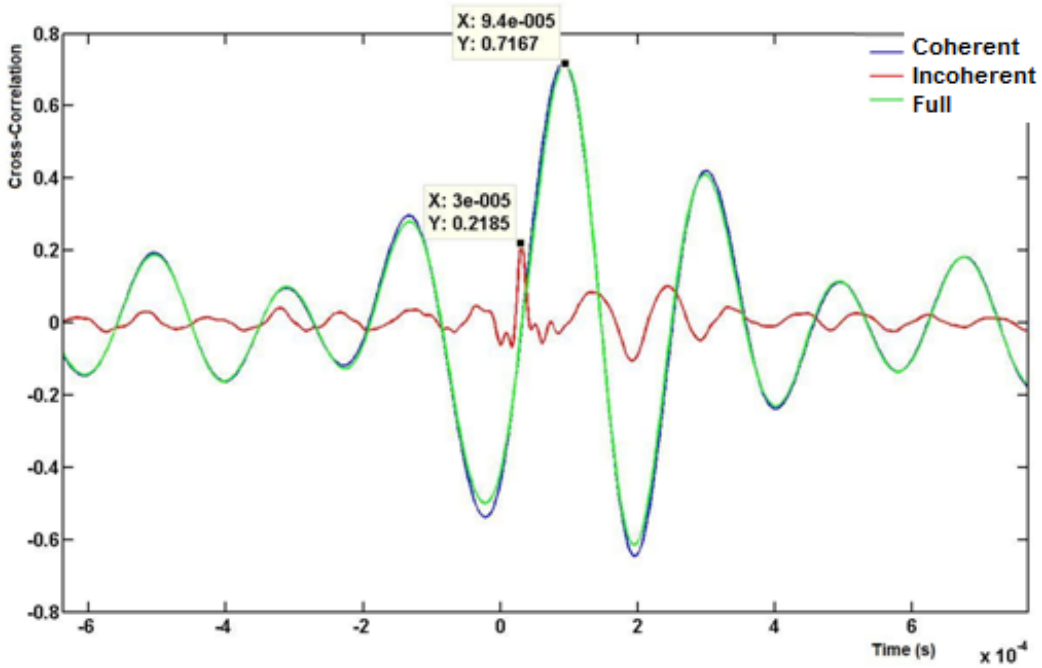

Figure 9: Cross correlation of the two microphones: Full signal (green line), Coherent part (blue line) and Incoherent part (red line)

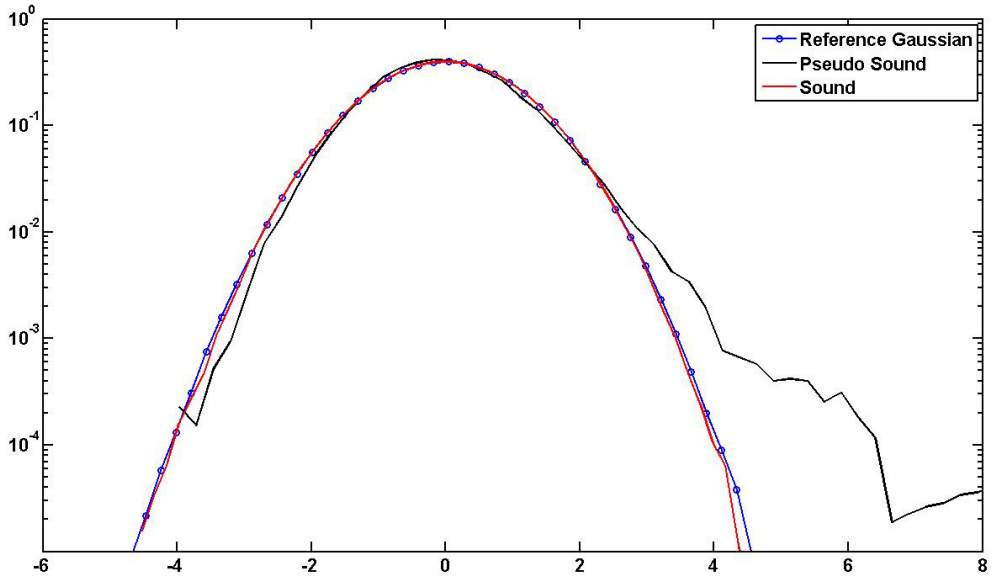

Figure 10: PDF of Sound and Pseudo-Sound part of a wavelet filtered signal.

However the energy of the pseudo-sound decreases rapidly (Howes 1960) and the algorithm loses efficiency when Sound and Pseudo-Sound start to have comparable energies (see Figure 11). The Figure 11 shows the use of the base algorithm in this particular condition. The algorithm is unable to separate all the incoherent part from the coherent indeed, the coherent signal still contain an incoherent part as evident from the shape of the correlation function that is a combination of a Dirac and a large Gaussian function.

Also the PDF of these signals indicates an inefficient filtering. As shown in Figure 12, both the coherent and the incoherent part are very close to the reference Gaussian. In this critical case the proposed algorithm underestimates the correct threshold, thus a modified version of the algorithm has been applied. In the new algorithm the threshold value is iterated. At each iteration the cross-correlation is computed and the iterations end when the correlation shapes, the PDF of the signals and the convective and the acoustic velocities confirm that is obtained an optimal filtering of Sound and Pseudo-Sound. The previous described algorithm is used for a first threshold calculation in a prediction phase.

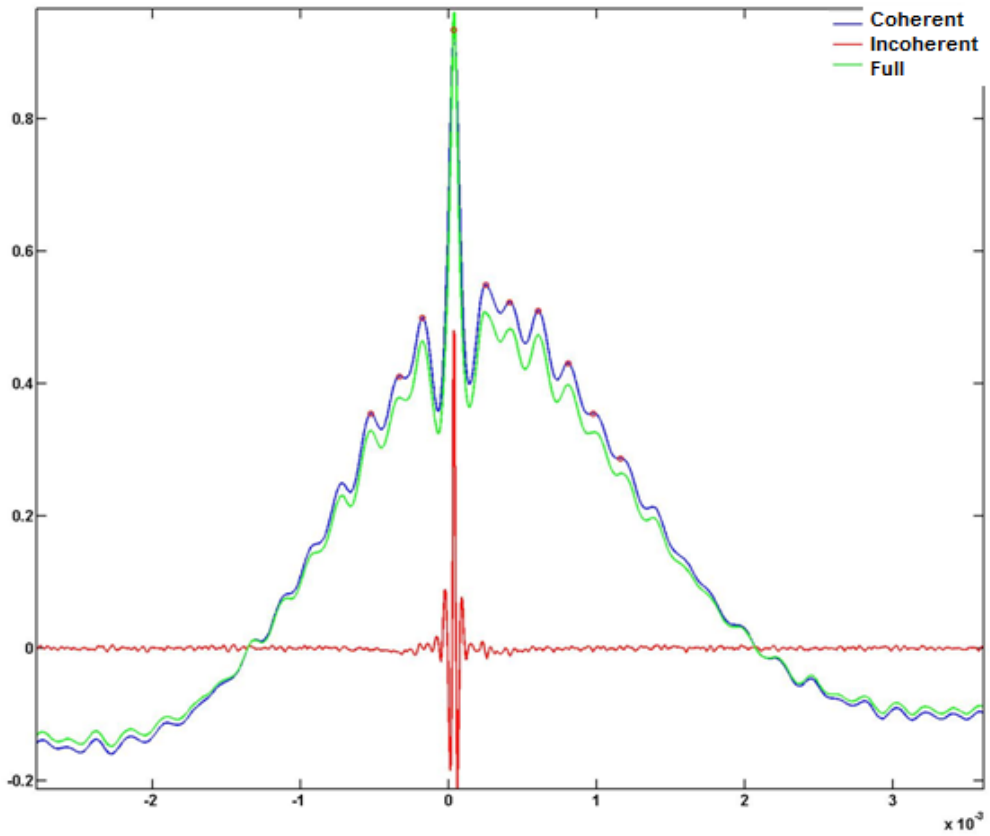

Figure 11: Cross correlation of the two microphones in a critical zone: Full signal (green line), Coherent part (blue line) and Incoherent part (red line)

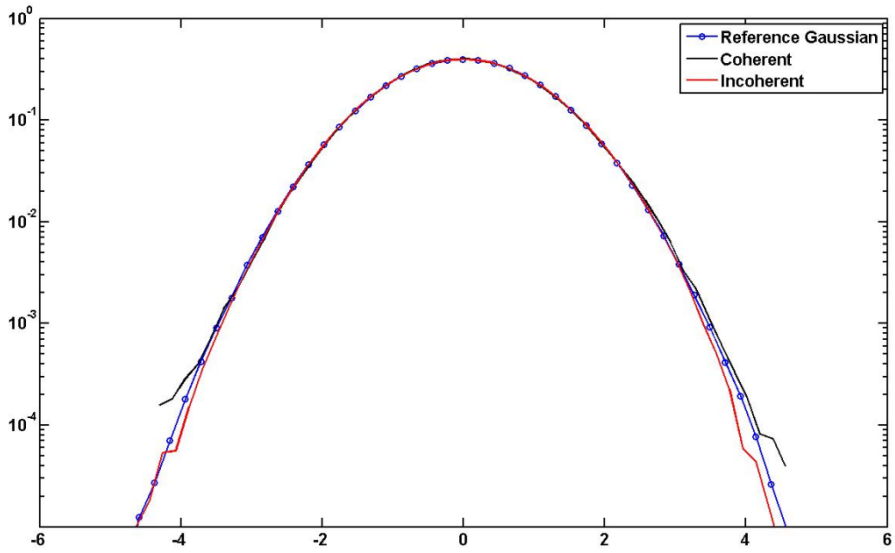

Figure 12: PDF of wrong filtered signals.

Calling the signal from the i-microphone as S_i, Sc_i is the coherent part of this signal and Si_i is the incoherent part. The modified algorithm controls the correlation functions of coherent and incoherent parts of the signals. The applied wavelets are orthogonal, so:

$$S_i = Sc_i + Si_i \qquad \text{Eq. 5}$$

The correlation for coherent structures (Sc_1-Sc_2) is large, similar to a Gaussian function around the peak and its peak position is proportional to the convective velocity.

The correlation for incoherent signals (Si_1-Si_2) is quite similar to a Dirac function and the peak position is proportional to the sound velocity propagation. This substantial difference between the two peaks makes possible to select a correct modified threshold until the two correlation functions (Sc_1-Sc_2 and Si_1-Si_2) assume the right shapes (e.g. Figure 13). At each iteration the algorithm calculates both the convective and the sound velocities and the signal to noise ratio (SNR) of the correlation functions. The SNR is overestimated as the ratio of the first and the second peak of the correlation functions. The algorithm ends when the convective velocity is subsonic, the SNR is greater than an appropriate value and the coherent PDF divergences from a reference Gaussian function but only if the incoherent PDF remain close to the Gaussian. The Figure 13 shows an example of correct cross-correlations.

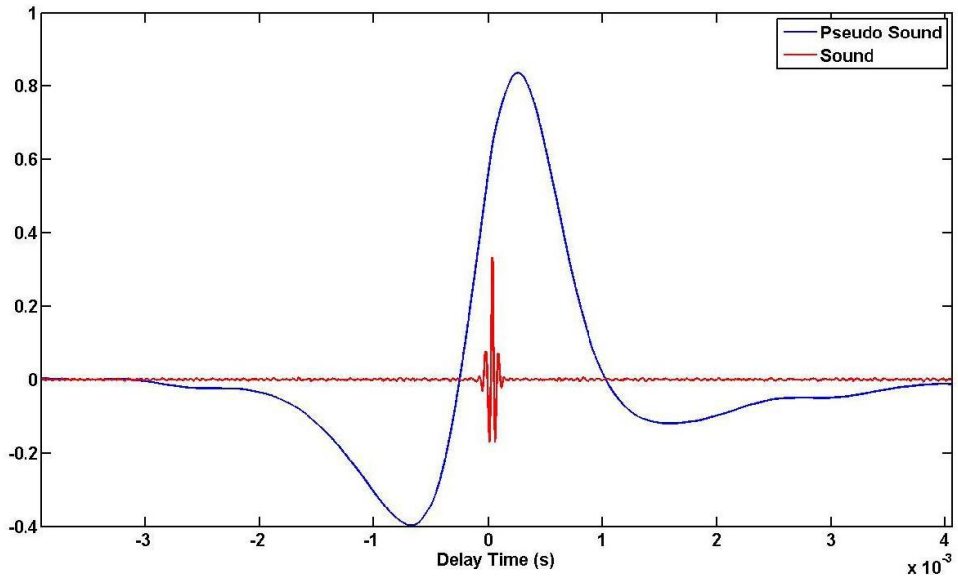

Figure 13: Correlation peaks with the modified wavelet algorithm.

With the use of the modified algorithm the PDF of the coherent signal becomes asymmetric with tails and the incoherent PDF maintains the Gaussian shape as shown in Figure 14; in this case the calculated propagation velocities from the Figure 13 are V_c = 55 m/s for the coherent signal and V_i = 410 m/s for the incoherent.

Another control is performed "a posteriori" with the cross-correlations Sc_1-Si_2 and Si_1-Sc_2, to verify the independence of the sound from the pseudo sound signals. If the filter is efficient, this cross-correlation is minimized (see Figure 15).

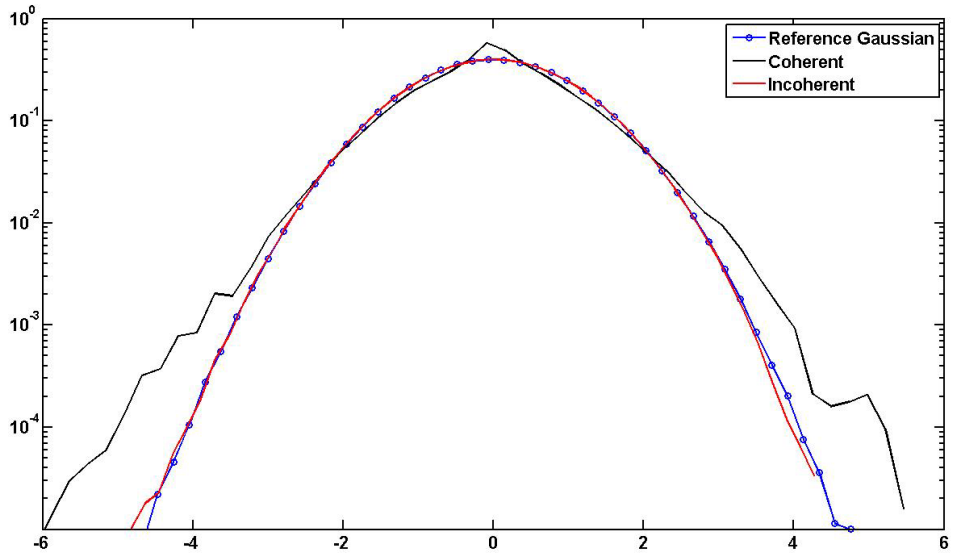

Figure 14: PDF of the filtered signals with a well selected threshold.

In this chapter a wavelet approach was proposed, a filtering algorithm and its evolution are applied for some near-field measurements and their limits were tested. Starting from two signals of pressure fluctuations acquired in the near-field, the algorithm divided them in two parts, the coherent part, that is the intermittent part of the signal, shown convective propagation velocity and characteristics that are related to the pseudo-sound pressure fluctuations. On the contrary the incoherent part propagates with sound speed and shows characteristics of the sound field.

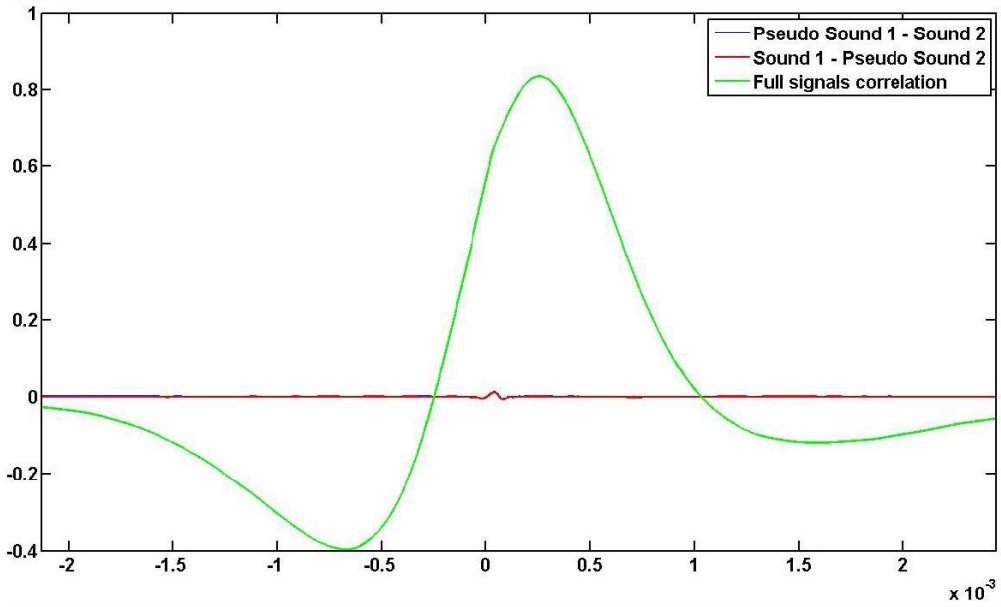

Figure 15: Verification of the independence of the sound signals from the pseudo-sound signals: the blue line is hidden by the red one.

The case where the original algorithm is efficient is shown in the Figure 16 top; is evident as the Sound spectra has very low energy respect to the pseudo-sound. On the bottom of the Figure 16 is shown the second case after the application of the modified algorithm, the energy of the sound part is higher than the previous case. In the Figure 16 is evident as the pseudo-sound and the sound exist in the full frequency domain and this filtering capability is only dependant by the wavelet use. A wavelet useful characteristic is that maintains the original synchronization in the inverse transformed signals, because it analyzes the signals also in time domain; it is just this feature that allows obtaining the propagation velocities of the filtered signals.

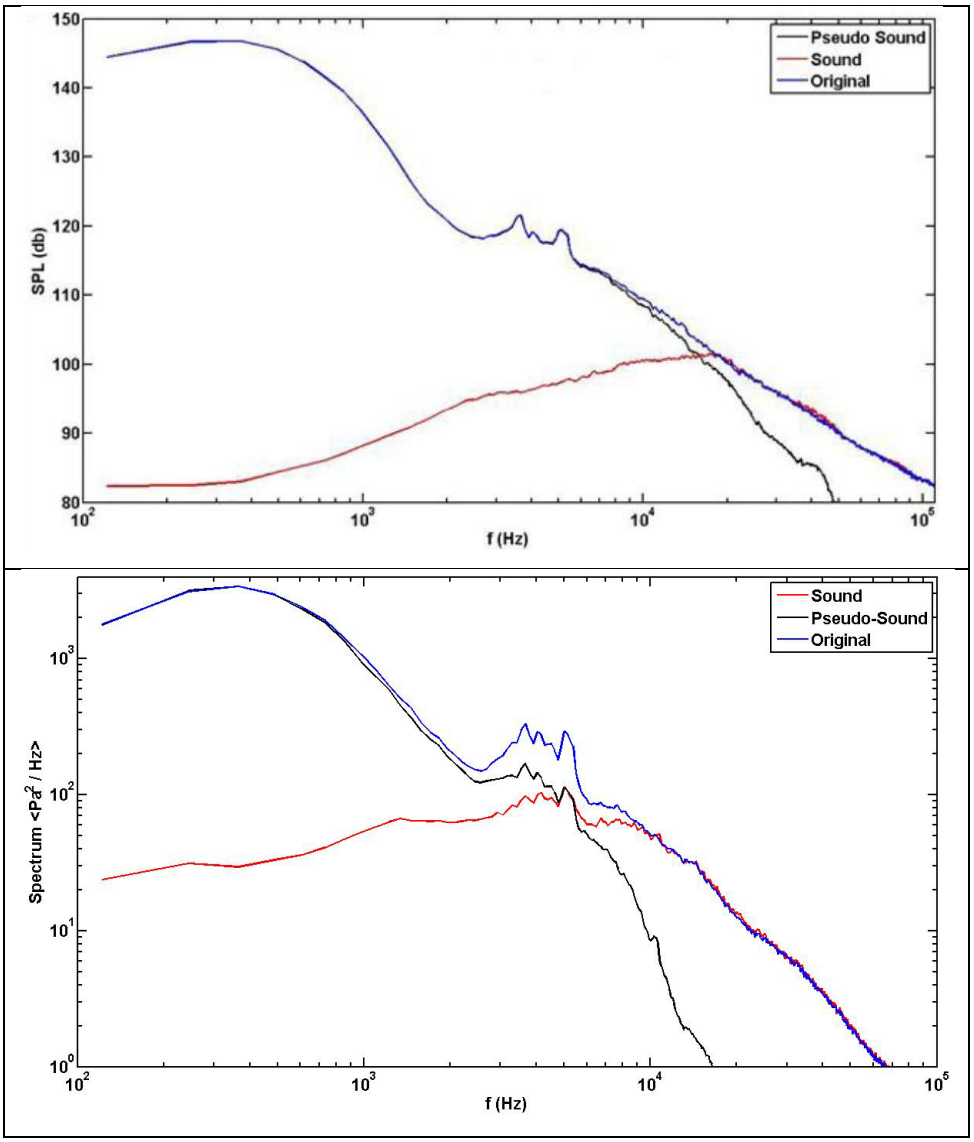

Figure 16: Filtered near-field spectra of the pressure fluctuations: on the top a measurement point at 1 diameter from the jet shear layer; on the bottom a point at 3 diameters from the shear layer.

4 Experimental Setup

To perform correct measurements a semi-anechoic chamber was prepared; the jet, installed in the chamber, is connected to a compressed air circuit powered by a rotary compressor. The complete setup is described in this Chapter as follows:

- semi-anechoic chamber characteristics;
- jet duct and nozzle design;
- sensors and jet calibration;
- instrumentation;

4.1 The Semi-Anechoic Chamber

The setup was prepared in a semi-anechoic chamber; the walls and the top of the room are covered with sound-absorbent panels mounted on wood struts; during the tests also the main part of the floor, the jet and the struts are covered with the same panels and a draining space is provided in the wall in front of the nozzle to eject the air excess (see Figure 17 for a scheme of the chamber and the jet installation). A jet usually has high entrainment and engulfment mechanisms that increase the ejected air-mass flow from the room, for this reason a recovery of the air comes from holes in the walls and from the air-circuit on the ceiling, these air intakes are behind coating panels. Upstream of the jet duct some security valves are applied on the air-circuit and a pressure regulator provides the correct air flow. The used nozzle has a diameter of 12 mm and for this reason generates sound at high frequencies. The used sound-absorbent panels are composed of 100mm polyurethane pyramids having a cut-off frequency of about 500 Hz (see Figure 18) that is sufficient for

these measurements. Moreover the absorbent coefficient at 250 Hz is 0.6 and this offers a good sound softening also at low frequencies.

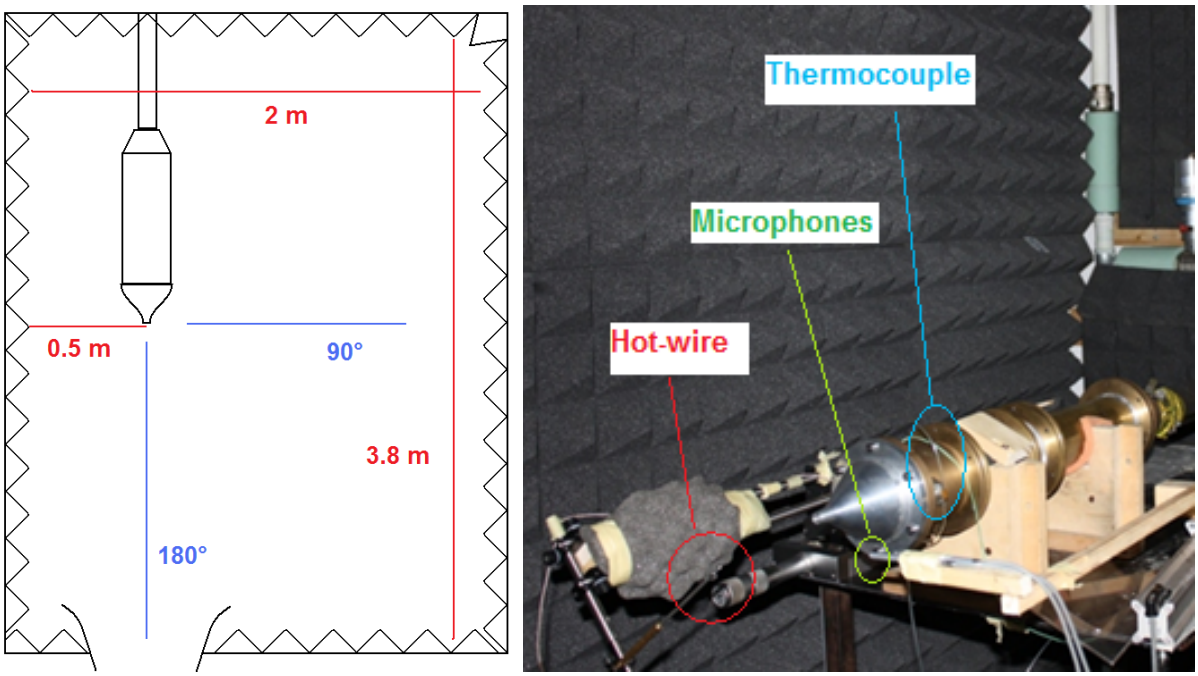

Figure 17: Plant of the semi-anechoic chamber with some dimensions (left). Jet installation in the semi-anechoic chamber (right) with sensors, hot-wire and near-field microphones.

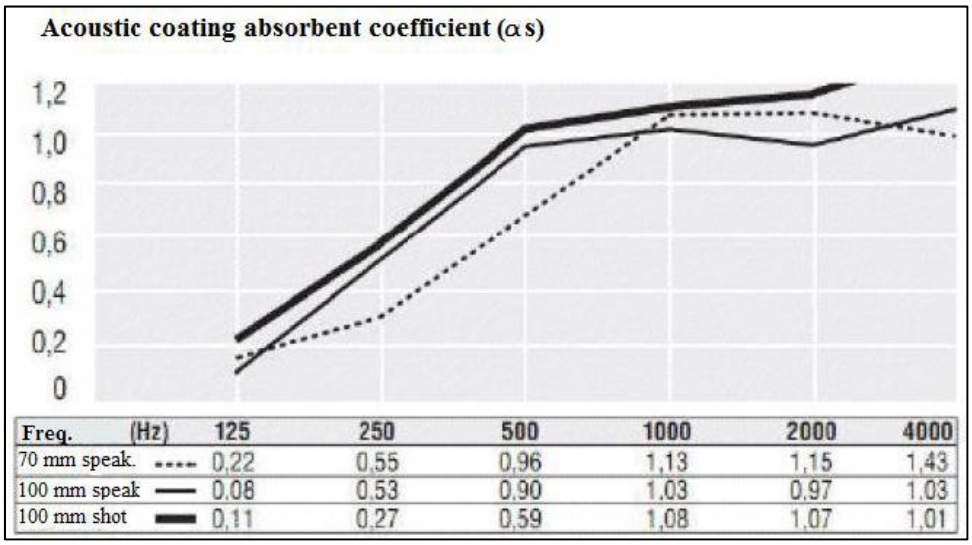

Freq. (Hz)	125	250	500	1000	2000	4000
70 mm speak. ----	0,22	0,55	0,96	1,13	1,15	1,43
100 mm speak ——	0,08	0,53	0,90	1,03	0,97	1,03
100 mm shot ▬	0,11	0,27	0,59	1,08	1,07	1,01

Figure 18: Characteristics of the sound-absorbent panels.

4.2 The Jet geometry

To connect the nozzle to the compressed air circuit a duct was designed; the duct has to reduce turbulences and asymmetries coming from the air supply, and it has to prevent undesired noise propagation inside it.

Upstream of the duct is installed a muffler (see Figure 19) that has been designed to dissipate the undesired noise produced by the valves and the compressed-air circuit. This muffler is a reactive-dissipative model called *"lined plenum chamber"* (Bell 1994). The frequency fading curve is reported in Figure 20, the coating in the installed muffler having a thickness of 100 mm.

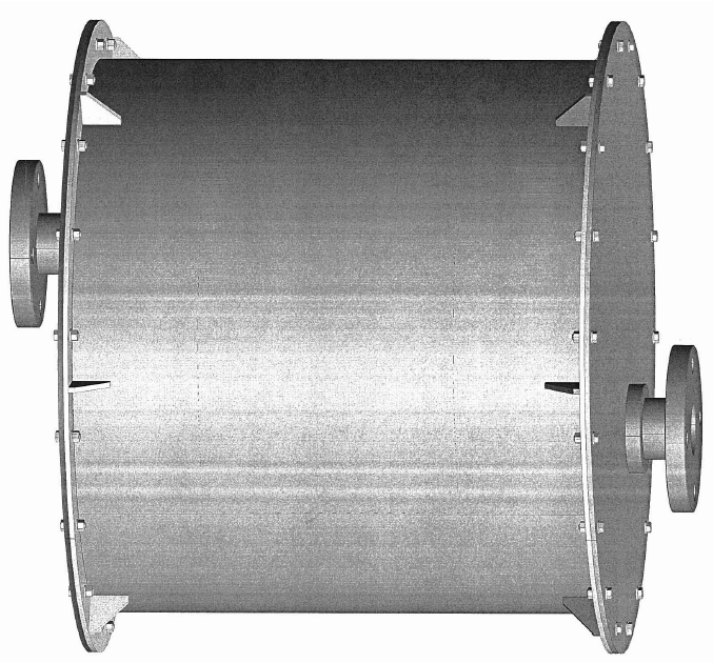

Figure 19: Reactive-dissipative muffler: *"lined plenum chamber"* type.

The main duct is connected with the muffler. Inside the duct is reasonable to consider the air speed lower than 10 m/s also at transonic jet velocity so is possible to dissipate the

turbulence, generating very low scale structures, without significant pressure losses or unwanted noise generation.

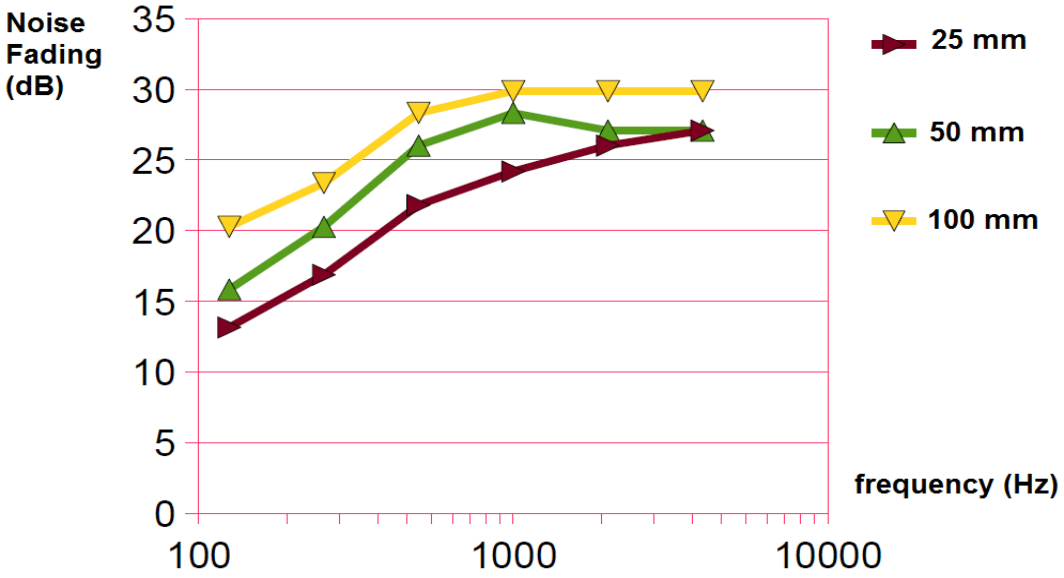

Figure 20: Noise fading curve for different thickness of the absorbent coating.

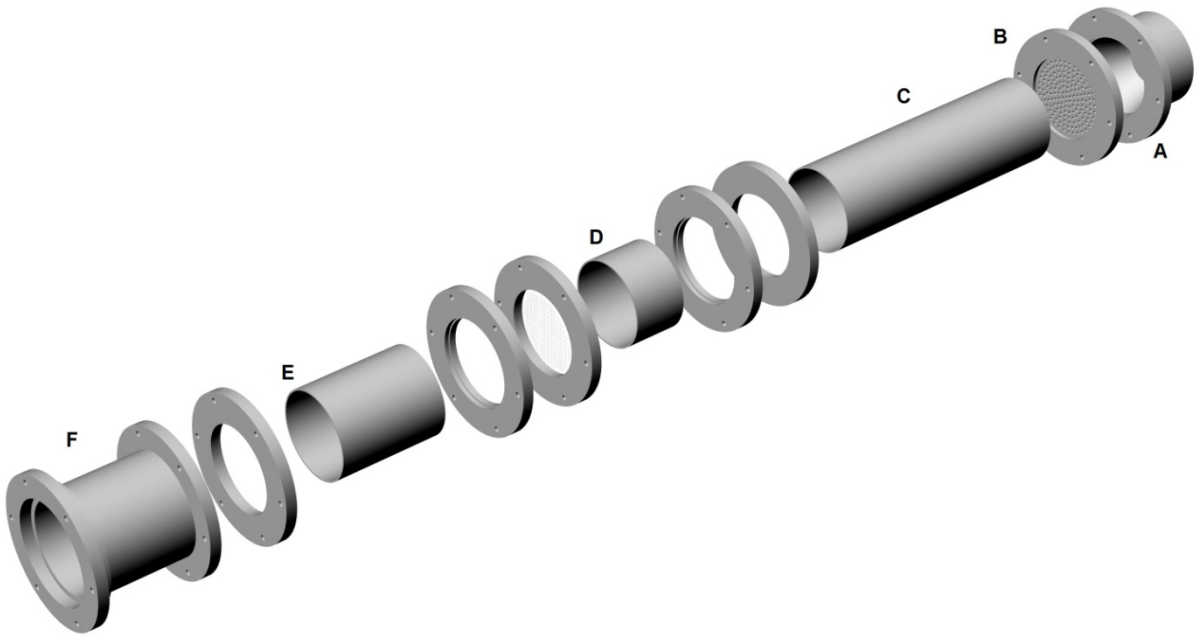

Figure 21: Duct exploded rendering.

The duct design is shown in the exploded rendering of Figure 21: it starts with a strong divergent part (part [A]) that connects the compressed air circuit (2 inches of diameter) with the rest of the duct (80 mm of diameter); in the divergent [A] there are the inlet of the main air supply and a small inlet of seeding for further velocimetry measurements; a glass wool is also inserted to eliminate noise propagation from the upstream ducts.

The [B] part is a holed plate with 158 holes of 3 mm diameter each. The total area is about 10 times greater that the nozzle outlet section; this part generates small scale structures that decay in a length of 100 diameters. This system uniforms the flow and reduces the turbulence coming from the air supply and from the divergent [A]. To ensure the complete decaying the [C] duct is 30 cm of length; the [D] section contains honey-comb of hexagonal 1 cm mesh size and 6 cm length. The honeycomb prevents swirl motions inside the flow canalizing the air in small straight ducts. At the end of the [D] section a net with a mesh squared size of 2 mm x 2 mm is placed: the net has the same function as the holed plate and generates small scale structures that decay in 20 cm of length. The main requirement for the net is the porosity ratio to be higher than 60% of the main duct. Using the Eq. 6, the porosity for the used net is P_n = 64%.

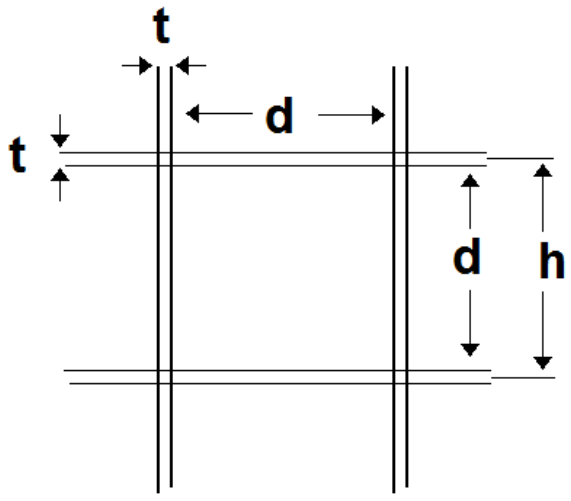

Figure 22: Net geometric characteristics.

Referring to the Figure 22 the net can be divided in elementary meshes so the complete area is h^2 and the empty section is d^2. From geometric considerations $h = d + 2 * t/2$, where t is the wire thickness. In the present case d = 2 mm and t = 0.5 mm.

$$P_n = \frac{d^2}{h^2} * 100 = \frac{d^2}{(d+t)^2} * 100 \qquad \text{Eq. 6}$$

Downstream of the net there are [E] and [F] ducts with a total length of 20 cm; the end section of the [F] part is built to match accurately with the nozzle avoiding steps or misalignments. In this section 4 holes of 1 mm are used to place pressure transducers and thermocouples. These sensors are used to calculate the exit velocity from the flow property in the upstream part. The small diameter of these holes doesn't interfere with the flow.

At the end of the duct is inserted the nozzle (see Figure 23), having an inlet section diameter of 80 mm (d_0) and an outlet section diameter of 12 mm (d); the contraction ratio is $A_r = (d_0/2)^2/(d/2)^2 = 44.44$.

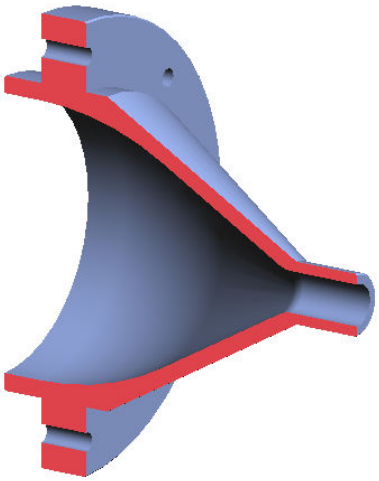

Figure 23: Axial section of the nozzle.

The nozzle is designed following the specifications of Glushko (1935) (see Figure 24), where $\mathbf{r_0}$ is the inlet section radius, $\mathbf{R_1}$ is the first tangential radius, $\mathbf{R_2}$ is the second tangential

radius, Θ is the nozzle angle, $\mathbf{l_0}$ is the length of the subsonic region and **r** is the outlet section radius. These parameters have to follow the constrains of Eq. 7 to avoid flow detachments:

$$R_1 \geq r_0$$
$$\Theta \leq 40° \qquad \text{Eq. 7}$$
$$R_2 > r$$

Following these relationships and minimizing the $\mathbf{l_0}$ to avoid an excessive boundary layer at the outlet section, the nozzle is designed with values shown in Tab 2.

r_0	40 mm
r	6 mm
R_1	80 mm
R_2	7.2 mm
Θ	30°
l_0	82.75 mm

Tab 2: Nozzle design parameters.

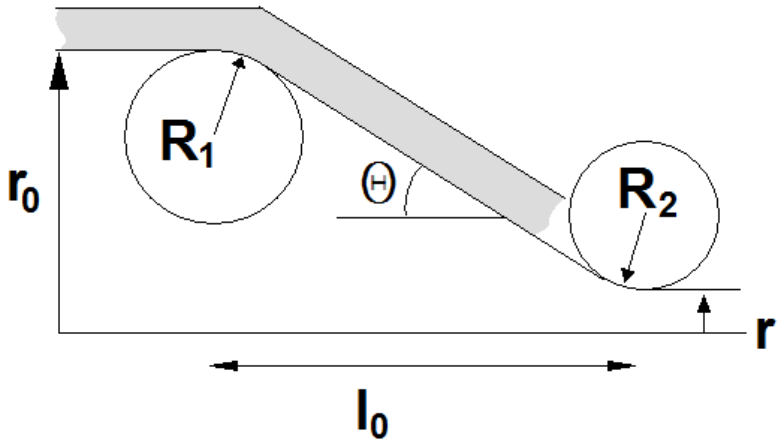

Figure 24: Nozzle design profile (Glushko 1935).

The complete Nozzle design is reported in Appendix A.

4.3 The Calibration of the Jet

As previously mentioned the jet was calibrated using the information thermocouples and pressure transducers placed just before the inlet section of the nozzle.

4.3.1 The Thermocouple

A J-type thermocouple is used for measuring the air temperature inside the duct. A thermocouple is composed by two wires of different metals in the hot junction that represents the measuring part. A J-type thermocouple is used. Usually the circuit of a thermocouple needs a cold junction and a voltmeter (see Figure 25), in the used sensor both the cold junction and the voltmeter are inner the Yokogawa DL708 oscilloscope that contains also the calibration function. The J-type (iron–constantan) has a restricted range of temperatures (−40 to +750 °C), but high sensitivity of about 55 µV/°C. The Curie point of the iron (770 °C) causes an abrupt change in its characteristics, which determines the upper temperature limit.

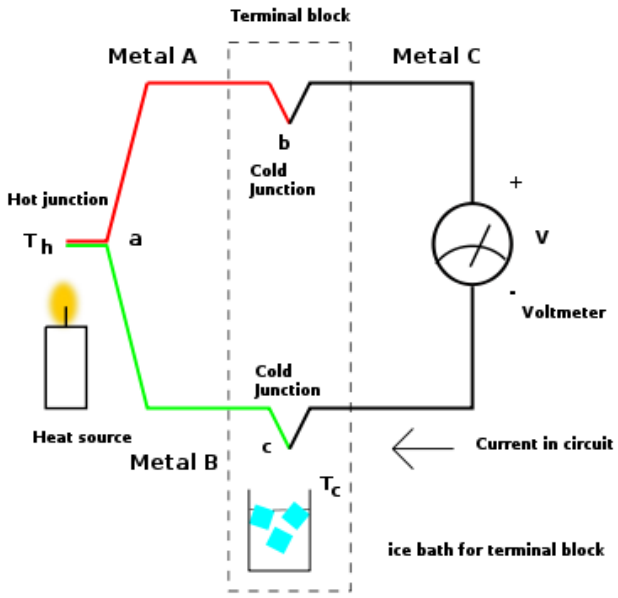

Figure 25: Example of thermocouple measuring circuit.

The hot junction has a spherical head with a radius of 0.5 mm that is inserted in the flow for 1 mm of height therefore its interference can be neglected. This head measures the total temperature of the air but for the low velocity in the duct it can be considered as the static temperature value as well.

4.3.2 The Pressure transducer

At the same section of the thermocouple is applied a circuit of tubes that captures the static pressure of the section from small holes that don't interfere with the flow; these tubes are connected with an ICSensors pressure transducer. The used transducer has a maximum pressure limit of 50 psi; it gives the difference between the measuring point pressure and the atmosphere; this transducer is powered with constant voltage DC current and needs to be calibrated to correlate the output voltage to the measured pressure (see Figure 26).

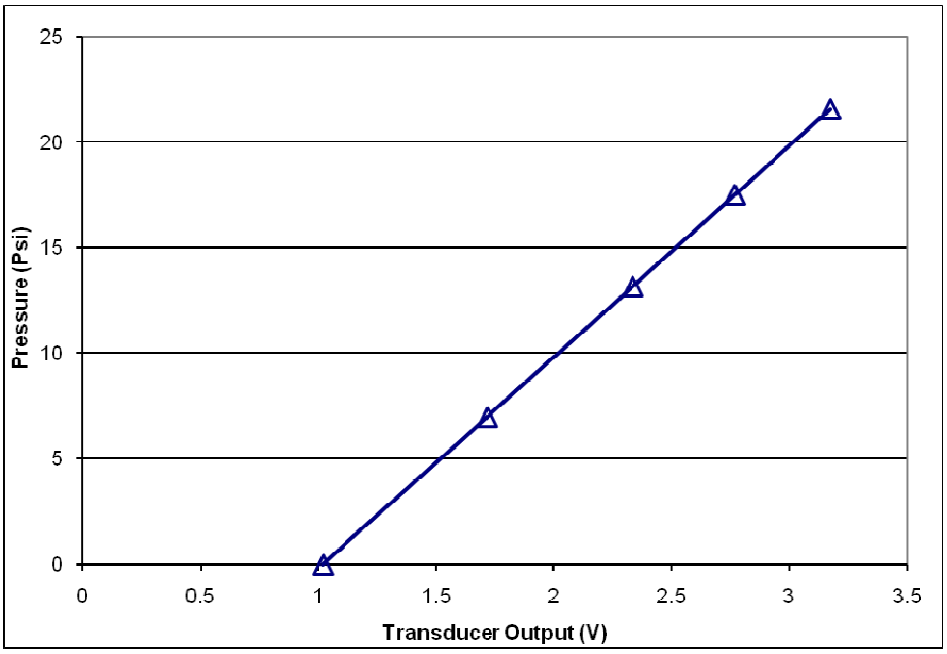

Figure 26: Pressure transducer calibration.

As shown in Figure 26 there is a linear correspondence between the measured pressure and the voltage output: $Dp = a * V + b$; in Tab 3 are presented the calibration parameters for the used transducer.

a	10.0069 Psi/mV
b	-10.1937 Psi
Sensitivity	99.9 mV/Psi
Uncertain	<0.05%

Tab 3: Pressure transducer calibration parameters.

4.3.3 Jet Velocity Calibration

The jet calibration starts from the measurement of the temperature and the pressure upstream of the nozzle. Defining **A** as a section, **T** the temperature, **P** the pressure and **M** the Mach number, the subscript ***i*** indicates the inlet section and ***j*** the outlet. The isentropic equations in an almost one-dimensional model are:

$$\frac{A_i}{A_j} = (H)^{\frac{\gamma+1}{2(\gamma-1)}} \cdot \frac{M_j}{M_i} \qquad \text{Eq. 8}$$

$$\frac{T_j}{T_i} = H = \frac{1+\frac{\gamma-1}{2}\cdot M_i^2}{1+\frac{\gamma-1}{2}\cdot M_j^2} \qquad \text{Eq. 9}$$

$$\frac{P_j}{P_i} = (H)^{\frac{\gamma}{\gamma-1}} \qquad \text{Eq. 10}$$

Dp is obtained from the pressure transducer and $\mathbf{P_i}$ is assumed to be the atmospheric pressure under the fully expanded jet hypothesis. Therefore:

$$P_j = P_i + Dp \qquad \text{Eq. 11}$$

From Eq. 10 and 9, ***H*** and $\mathbf{T_j}$ are obtained; knowing the contraction ratio A_i/A_j from Eq. 8 and the second part of Eq.9 the outlet Mach number $\mathbf{M_j}$ is calculated. From $\mathbf{T_j}$ and $\mathbf{M_j}$ the velocity of the jet is calculated using the following equation:

$$U_j = M_j * \sqrt{\gamma R T_j} \qquad \text{Eq.12}$$

Figure 27 shows the jet calibration results, the pressure transducer output related to the evaluated jet Mach number and the jet exit velocity. The divergence of the two curves depends by the exit temperature decreasing with the increasing of the expansion ratio in the nozzle. From the previous mentioned equations is also possible to evaluate the air velocity in the duct: as shown in Figure 28 the velocity is less than 5 m/s, as expected; this velocity guarantees that the noise generated inside the duct is negligible and the pressure losses caused by the net and the honeycomb are very low.

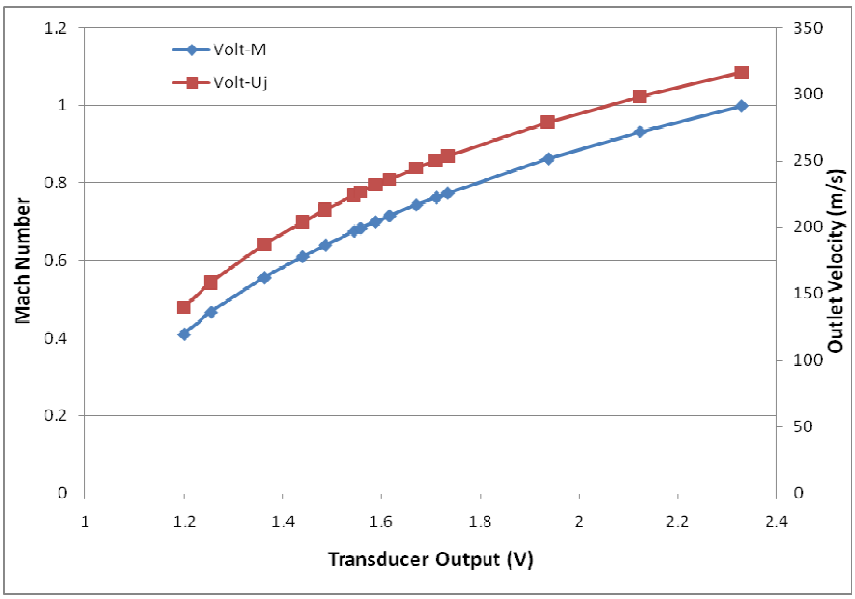

Figure 27: Jet Calibration: Jet Mach number (blue line) and Jet velocity (red line) respect the transducer voltage output.

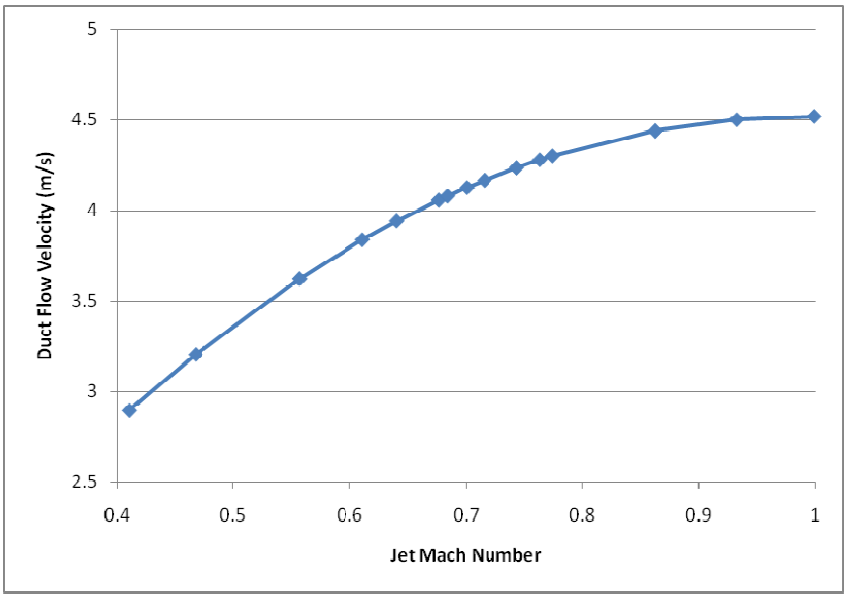

Figure 28: Evaluation of the air velocity in the duct with respect to the Jet Mach number.

4.4 Velocimetry and Acoustics sensors

During the experimental campaign conducted to qualify the flow-dynamic of the jet, a Pitot tube and a hot-wire probe were used. The Pitot tube is used for a qualification of the velocity profiles both in the potential core and in the fully developed region and to verify the self-similarity of the velocity profiles. The hot-wire probe is used for deeper study of the velocity and turbulence distribution along a symmetry plane of the jet. Synchronized velocity and pressure measurements were carried out to investigate the noise-generation phenomena. Two microphones Brüel & Kjær 4939 are used for the pressure measurements.

4.4.1 The Pitot Tube

The Pitot tube consists of a small probe of about 2 mm of maximum diameter and 6 holes for the static pressure measurement (see Figure 29). The Pitot tube total pressure duct is connected with a pressure transducer of the same model as the one previously described; its calibration parameters are slightly different and are reported in Tab 4.

a	10.04976 Psi/mV
b	-8.310 Psi
Sensitivity	99.5 mV/Psi
Uncertain	<0.06%

Tab 4: Second pressure transducer parameters.

$$u_p = \sqrt{\frac{2\gamma RT}{\gamma - 1}\left[\left(\frac{p_t}{p_s}\right)^{\frac{\gamma-1}{\gamma}} - 1\right]} \qquad \text{Eq. 13}$$

To evaluate the maximum interference of the Pitot tube with the flow, an additional jet calibration has been performed to evaluate the jet velocity both with the Pitot tube in correspondence of the outlet section and the sensors upstream of the nozzle.

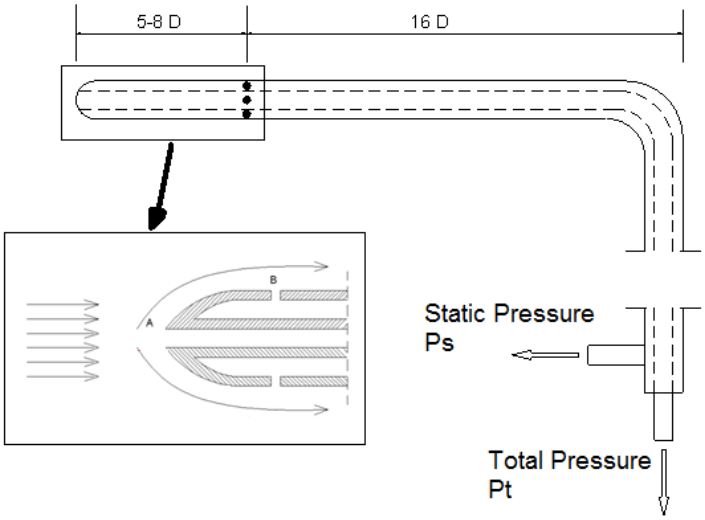

Figure 29: Pitot tube drawings.

The interference of the Pitot tube with the flow is shown in Tab 5. The maximum interference is of about 4.7 % obtained in correspondence of the centre of the nozzle outlet section. The evaluated intrusiveness is reasonably low and the simplicity of use and robustness of the Pitot tube justify its use for a velocity qualification in terms of mean values.

Jet evaluated velocity	Pitot tube measured velocity	% error
185.8 m/s	190.8 m/s	2.7
166.2 m/s	174.1 m/s	4.7
140.3 m/s	146.2 m/s	4.3

Tab 5: Evaluation of the interference of the Pitot tube.

4.4.2 The Hot-Wire Probe

For advanced and accurate velocity measurements a Dantec 55P11 hot wire probe (see Figure 30) is used. This probe is a single wire sensor whose characteristics are shown in Tab 6. Due to the small diameter of the wire and of the prongs, the sensor interference with the flow is negligible. The interference with the acoustic measurements will be evaluated afterwards.

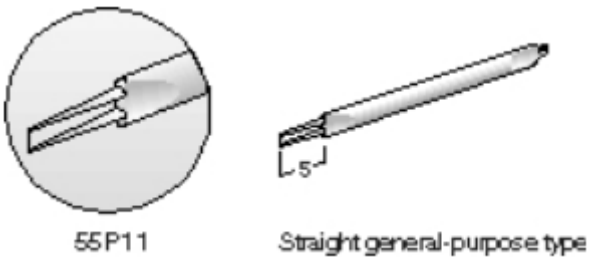

Figure 30: 55P11 Hot-wire sensor (www.dantecdynamics.com)

The hot-wire calibration is performed using the same jet, and the information from the sensors upstream of the nozzle are used to determine the exit velocity. The probe to be calibrated is positioned at the center of the jet section and in the potential. The hot-wire probe is used in constant temperature mode and it is calibrated starting by the lowest stable velocity generated with the jet and is extended to the necessary Mach number; a 4^{th} order polynomial curve (see Figure 31) is generated with a least square algorithm as the best approximation for the hot-wire voltage-velocity equation (Eq. 14).

Technical data for miniature wire sensor Dantec 55P11	
Medium	Air
Sensor material	Platinum-plated tungsten
Sensor dimensions	5 µm dia. 1.25 mm long
Sensor resistance R20 (approx)	3.5 Ω
Temp. Coeff. of resistance (TCR) α 20 (approx.)	0.36%/°C
Max. sensor temperature	300°C
Max. ambient temperature	150°C
Min. velocity	0.05 m/s
Max. velocity	500 m/s
Frequency limit fcpo (CCA mode, 0 m/s)	90 Hz
Frequency limit fmax (CTA mode)	400 kHz

Tab 6: Hot-wire sensor characteristics.

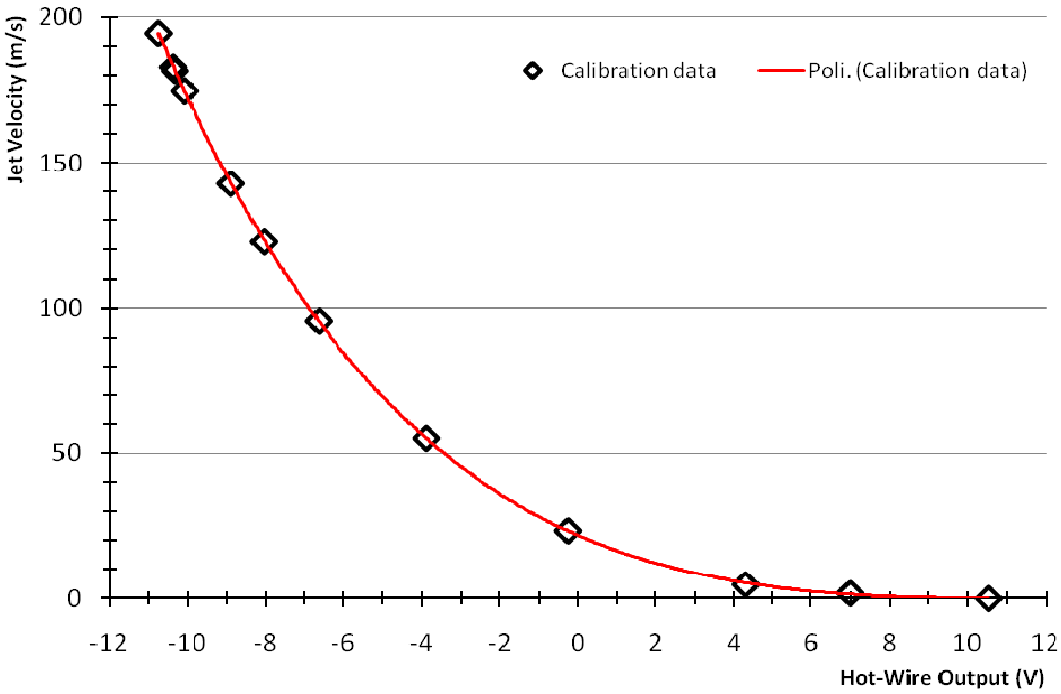

Figure 31: Hot-wire calibration data and the 4th order polynomial curve.

$$U_{hw} = 0.00062\,V^4 - 0.02754\,V^3 + 0.58104\,V^2 - 5.85316\,V + 21.84032 \qquad \text{Eq. 14}$$

Usually the hot-wire probe can be influenced by the compressibility and the pressure and density fluctuations of a transonic flow (Horstman and Rose 1975). The velocity measurements of this work are performed at a maximum mach number of 0.6. However, a second test is performed to evaluate where the compressibility effects appear. In this test the hot-wire probe, in the same position as in the previous calibration, is tested at velocities from mach 0.1 to Mach 1. The compressibility effects are evaluated when the measured values diverge from the 4th order equation.

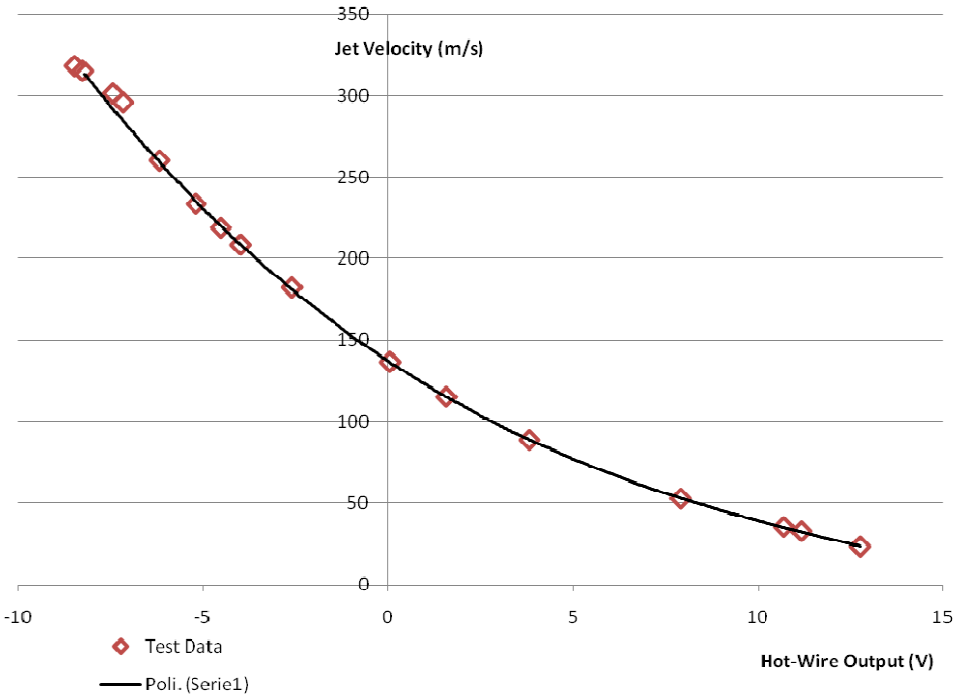

Figure 32: Evaluation of the compressibility effects on hot-wire.

Figure 32 shows the hot-wire voltage output in a wide range of velocities. The effects of compressibility can be estimated to be important where the acquired data have a deviation from the fitting curve. This happens at a velocity of 280 m/s that corresponds to a Mach number of 0.85.

4.4.3 The Microphones

The microphones used for the pressure field measurements are two Brüel & Kjær 4939 (see Figure 34). These ¼" diameter microphones are pre-amplified to guarantee a more stable sensitivity with the temperature. They are connected to the B&K Nexus 2690 that is a signal conditioner and amplifier. The microphones have a wide frequency response up to 100 kHz (see Figure 33). The Nexus filters the signals with a band-pass of 20 Hz - 100 kHz. Tab 7 shows the characteristics of these microphones taken from the B&K product information. As shown in Figure 34 these microphones have a protective grid that has to be removed for accurate acoustics measurements according to the literature (Viswanathan 2009).

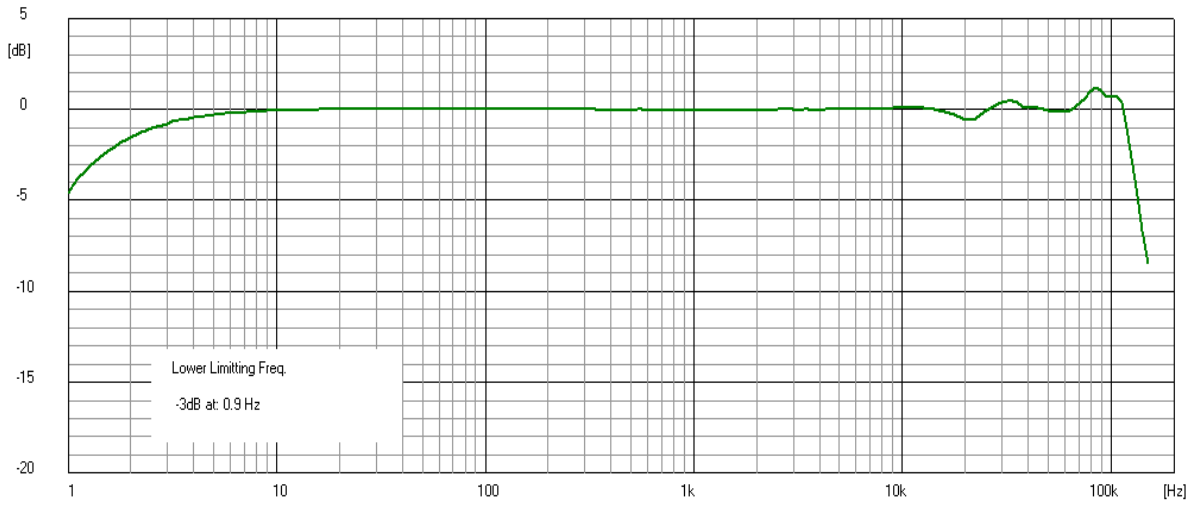

Figure 33: Frequency response of the B&K microphones without the protective grid.

Sensitivity	4 mV/Pa
Frequency range	4 Hz – 100 kHz
Dynamic range	28 – 164 dB
Temperature Range	-40°C – 150°C

Tab 7: Brüel & Kjær 4939 microphone characteristics.

The simultaneous use of two microphones makes necessary to compare their frequency response. For this reason a measure is performed with this two sensors in the same position and comparing the spectral response in 1/3 octave-bands. The Figure 35 shows as the response differs with a maximum percentage difference of 1.5%.

The thermocouple, pressure transducers, microphones and the hot-wire signals are acquired with a Yokogawa DL708E with a sampling frequency of 500 kHz to obtain $5*10^6$ samples.

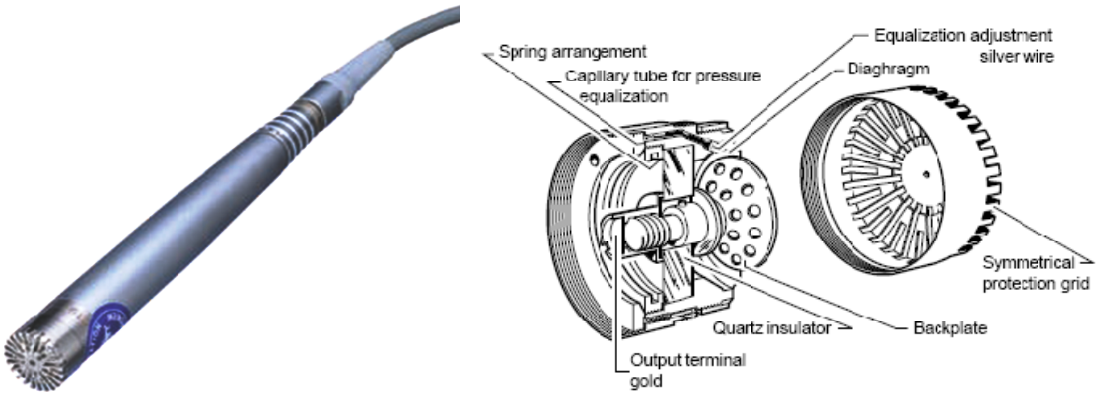

Figure 34: A Brüel & Kjær 4939 microphone: on the left the microphone connected with its pre-amplifier; on the right the inner structure of the microphone.

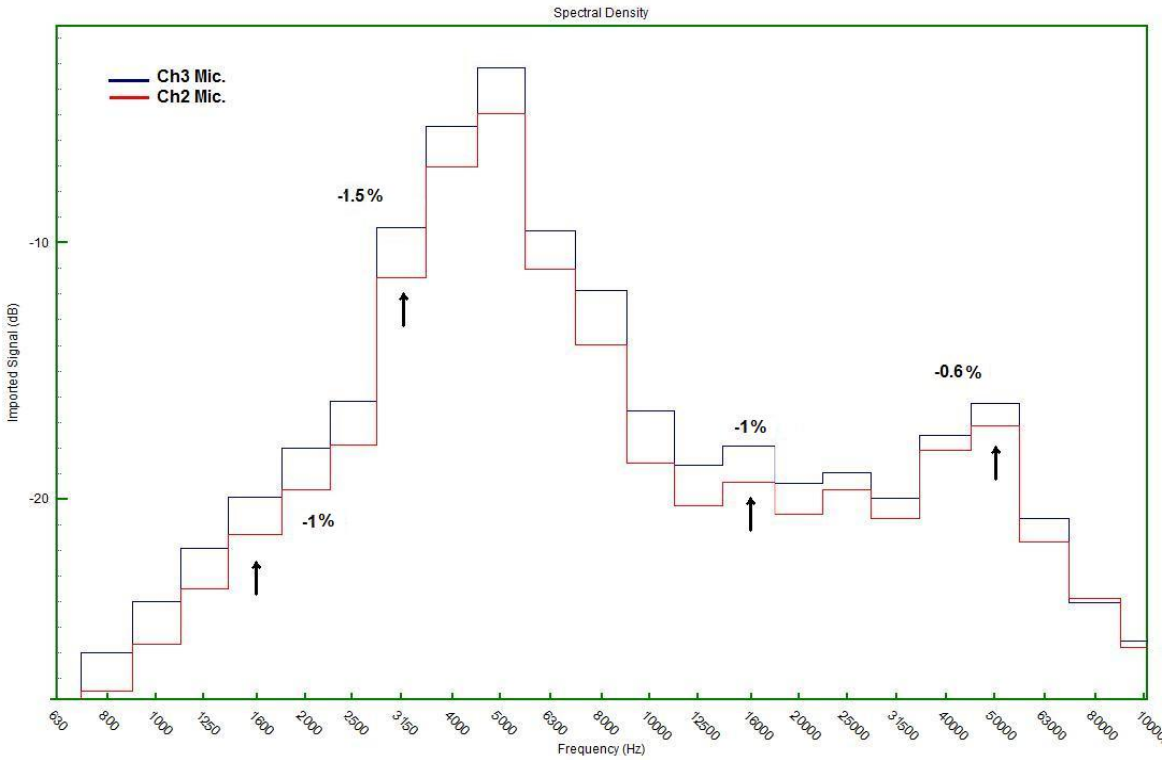

Figure 35: Microphones comparison in 1/3 octave-bands.

5 Jet Characterization

Hot-wire and Pitot tube measurements are performed to verify the jet flow characteristics. The Pitot tube measurements are aimed at verifying the jet symmetry and the characteristics of self-similarity of the velocity profiles, as well as the axial velocity decrease. The Hot-wire measurements are performed to obtain high order statistics as axial velocity variance, the skewness and the Kurtosis. The sound measurements in the far-field complete the jet characterization and allow us to compare the sound spectra with literature data. Figure 36 defines the used reference system for the measurements with the X correspondent with the jet axis.

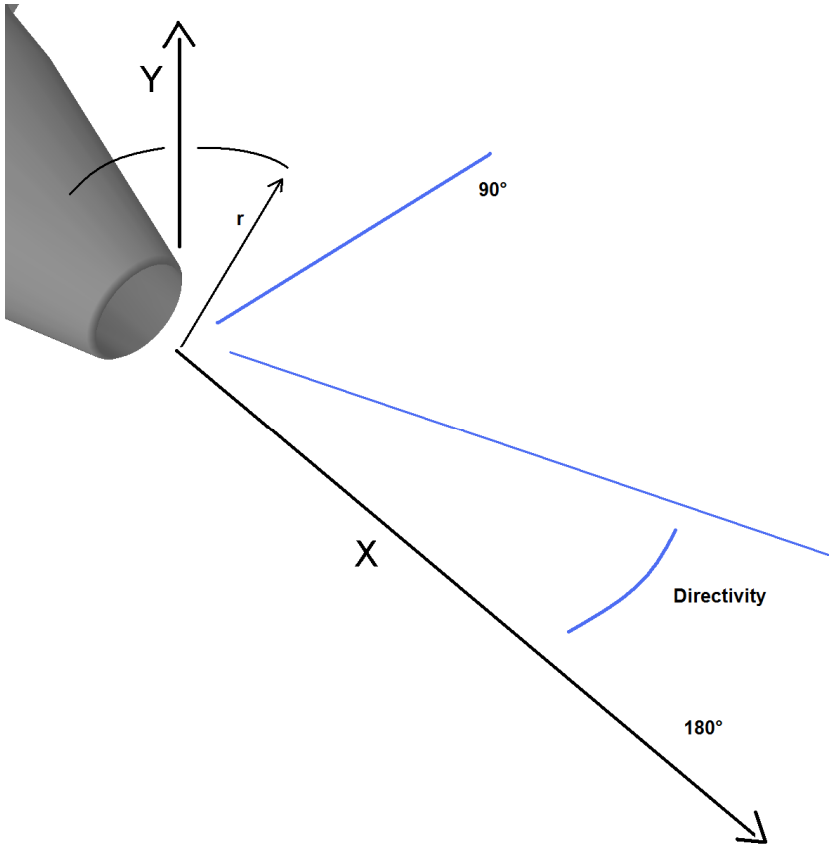

Figure 36: Reference system: X corresponds to the jet axis

5.1 The Jet Flow-Dynamics

With the jet set at M= 0.7, the axial velocity profiles, in the radial direction, are measured with the Pitot tube from 0 to 10 D on the jet axis. The Pitot tube was aligned with the jet geometrical axis to verify misalignments and asymmetries. The measurements from 0 to 4 diameters are performed with radial steps of 1 mm to verify the symmetry of the jet potential core. In particular the velocity profiles at a distance of 2 D are performed along horizontal, vertical and ±45° diagonal diameters. The other velocity profiles are measured to compare the incipient self-similarity with well-known data as the Goertler type solution. Velocity measurements on the jet axis from 0 to 33 diameters with a step of 1D are performed to verify the axial velocity decreasing and to calculate the C coefficient (see Paragraph 2.1, Eq. 1). In Tab 1 the Pitot tube measurements are summarized. Figure 37 shows the inverse of the axial velocity. In the turbulent region, the jet exit velocity Uj divided with the velocity measured on the jet axis follows a linear decay equation. The decreasing coefficient C can be calculated from the linear fit in Figure 37:

$$\frac{U}{U_j} = C\,\frac{D}{X} = \frac{1}{0.179}\,\frac{D}{X} \;\rightarrow C = 5.58$$

Axial Distance - X	Radial step - r	Measured diameter
0 D	1 mm	Horizontal
2 D	1 mm	Horizontal, Vertical and ±45°
4 D	1 mm	Horizontal
5 D	1 mm	Vertical
6 D	1 mm	Horizontal
8 D	2 mm	Vertical
10 D	2 mm	Horizontal

Tab 8: Pitot tube measurements of the axial velocity profiles.

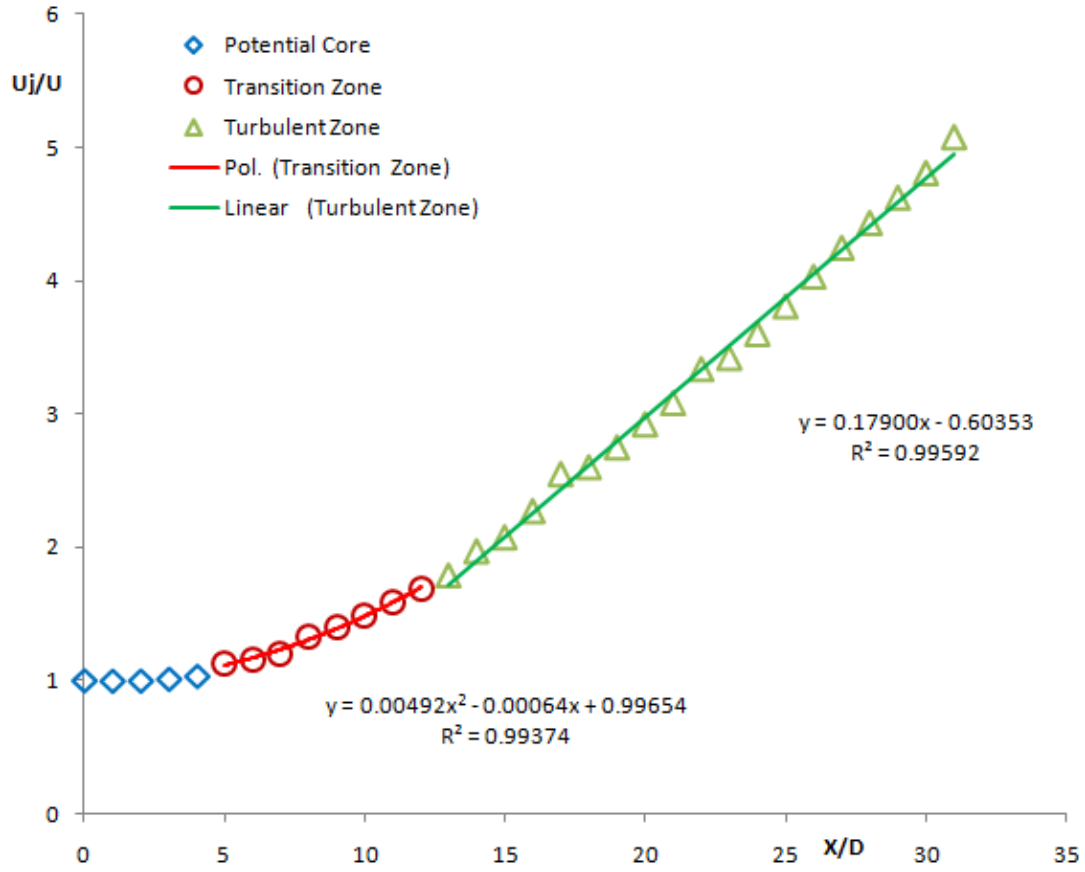

Figure 37: Inverse of the axial velocity decreasing.

It is found C=5.58 that compared with the results reported in Tab 1 shows a good agreement in particular with the coefficients calculated by Becker (1967) and So (1990). The Figure 37 shows that the potential core extension is of about 4 diameters. The potential core is defined as the part of the flow where the axial velocity is undisturbed, and $U_j/U \approx 1$ (Rajaratnam 1976). Also the transition zone is evident where the velocity doesn't follow a linear profile (see red line in Figure 37).

The axial velocity profiles in the potential core (see Figure 38) show a good symmetry with some oscillations in the peripheral zones depending by the uncertain in the use of the Pitot tube. The error bars indicate the error of about 5% previously evaluated as the maximum interference of the Pitot tube with the flow. At section 0 diameters there is the typical top hat profile.

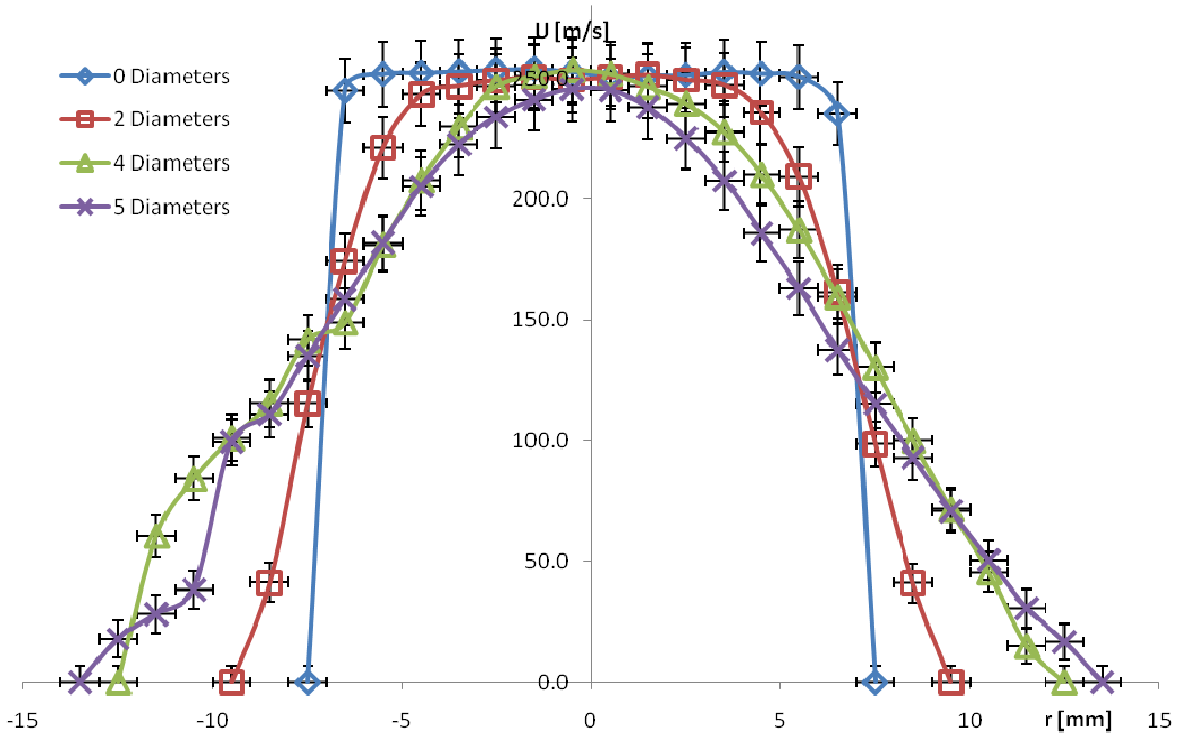

Figure 38: Axial Velocity profiles in the potential core.

Further measurements of the velocity profiles are necessary to evaluate the complete axial-symmetry of the jet. These measurements are performed on the section at 2 diameters from the jet exit along the horizontal, vertical and diagonal directions reported in Tab 8. Figure 39 demonstrates the axisymmetry of the jet, excluding misalignments and undesired motions in the nozzle. Downstream of the potential core velocity profiles are shown in non-dimensional form. The measured velocity (***U***) is divided by the local mean velocity value on the jet axis ($\boldsymbol{U_m}$). The position is divided by the local half jet aperture (***b***), as defined in Chapter 2. In this form the self similarity becomes, as shown in Figure 40.

The estimation of half aperture ***b*** makes possible also to evaluate the jet aperture angle that results of about 9 – 10°.

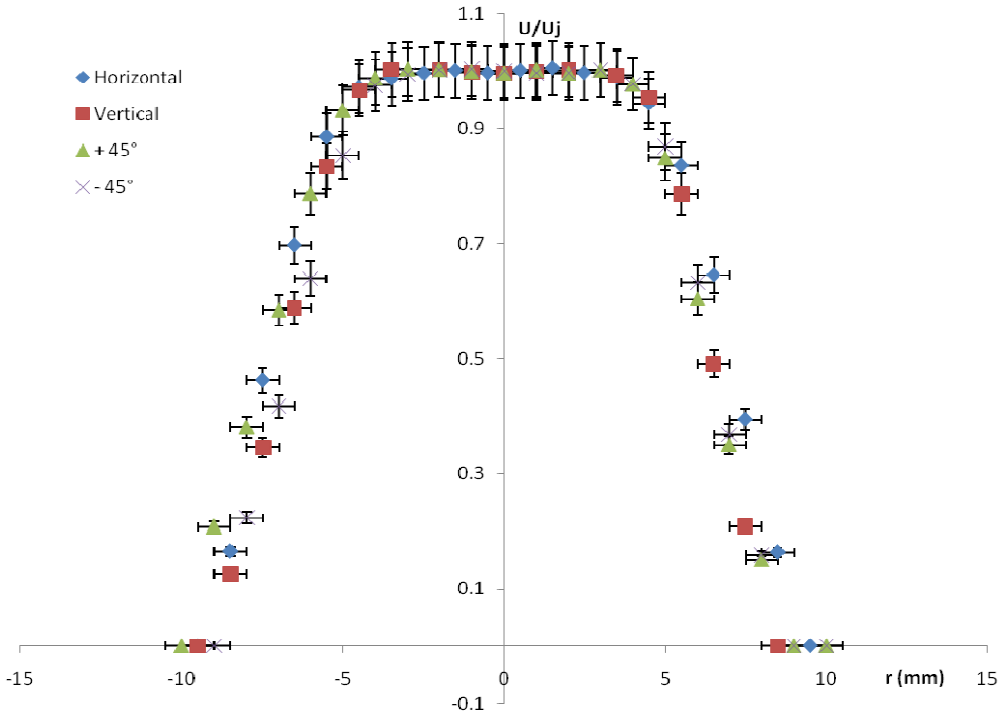

Figure 39: Axial velocity profiles at 2 diameters section along the 4 directions.

Usually in the transition zone, the velocity profiles begin to show self similarity. These profiles are reported in Figure 40 with a Goertler type profile as comparison. The discrepancy between the analytic curve and the tails of the profiles is explained by the low sensitivity of the Pitot tube at the low velocities. Anyway the self-similar profiles confirm the good symmetry of the jet.

Further flow qualification is performed with hot-wire measurements. A single wire probe is used as described in Chapter 4. In a three-dimensional flow single-wire probe measurements are affected by two velocity components (see Figure 41); referring to the Figure 41 the Hot-wire measures the sum of the U_1 and the U_2 velocities and is unaffected by the U_3. This causes measurement errors if the flow has strong transversal components. For its nature a jet flow has an axial symmetry, positioning the measurement points on a symmetry plane the stronger velocity components are the axial velocity (***U***) and the radial velocity (***V***), the third velocity component (***W***) is orthogonal to the symmetry plane and has usually a mean value closest to zero and a very low turbulence (Hussein et Al. 1994). Positioning the wire

parallel to the plane of symmetry the ***V*** component results parallel to the wire and doesn't affect the ***U*** measurements. Referring to the Figure 41 and Figure 42 it becomes $U=U_1$, $W=U_2\approx 0$ and $V=U_3$. A scheme of the hot-wire measurement points and the position of the probe is given in Figure 42, the out of plane velocity ***W*** being closest to zero doesn't affect the measurements.

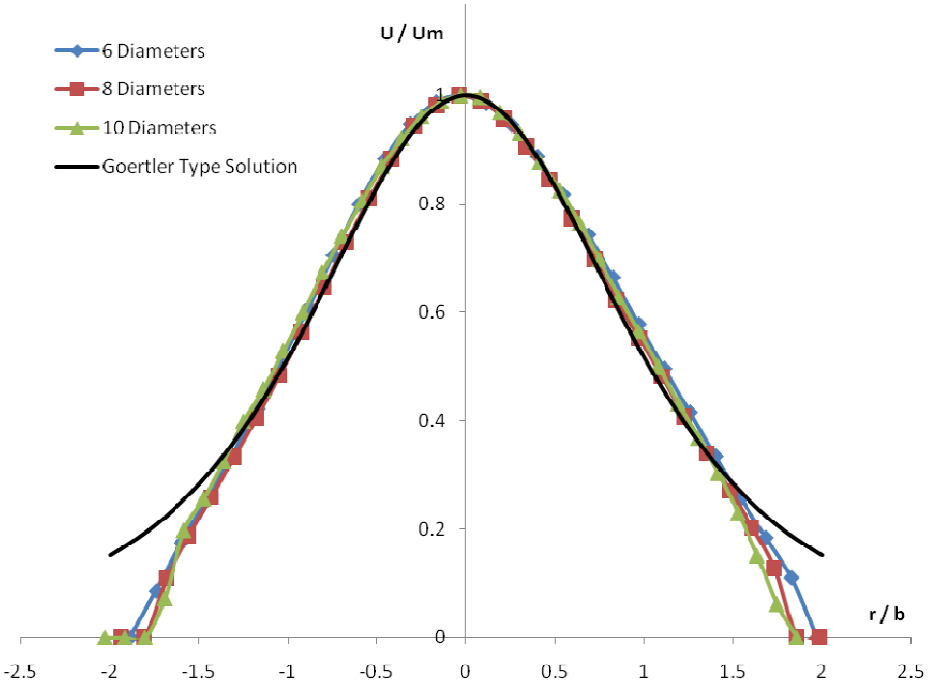

Figure 40: Self-similarity of some axial velocity profiles.

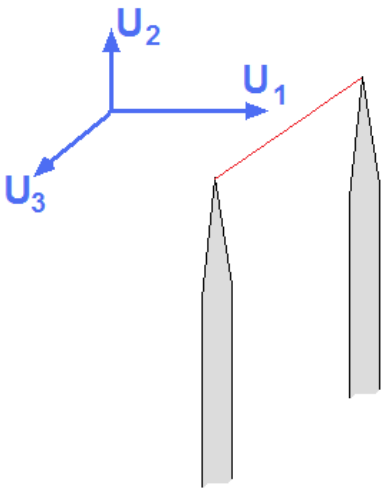

Figure 41: Single wire probe in a three component flow.

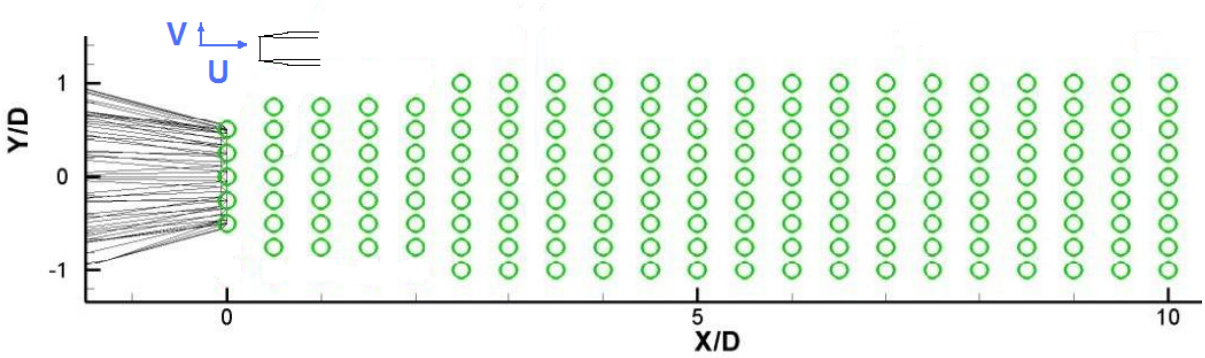

Figure 42: Hot-wire probe position and measurement points.

The hot-wire probe measurements are performed at a Mach number of 0.5. The turbulence of the shear layer just outside the nozzle is evaluated to establish the nature of the boundary layer. Figure 43 shows the velocity spectrum just outside the nozzle, inside the shear layer generated inside the duct. According to the Kolmogorov's hypothesis, the -5/3 slope indicates a fully developed turbulent condition, thus indicating that the boundary layer is turbulent.

From the measurement points of Figure 42 planar distributions of the axial velocity ***U*** and of the other statistics as the Reynolds stress $\langle u' \rangle^2$ are obtained. Figure 44 and Figure 45 show that these distributions are similar to literature results. From the Figure 44 (left) is evident the jet expansion and the velocity decrease. Also, turbulence from the nozzle expands downstream and rejoins the jet axis at the end of the potential core, around 4 -5 diameters. Figure 45 shows the skewness (left) and Kurtosis (right) distributions. The maximum value of the Kurtosis locates the end of the potential core. The peripheral zones of Figure 45 exhibits high skewness and Kurtosis values being affected by the fluctuations of the jet shear layer.

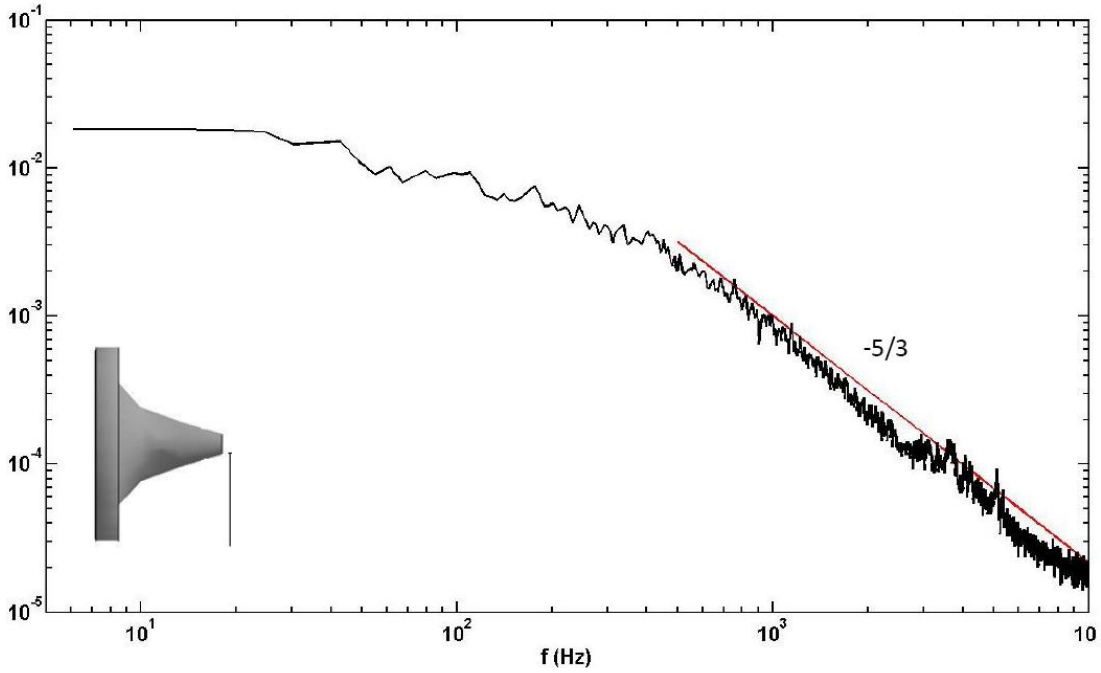

Figure 43: Velocity spectrum of the nozzle boundary layer.

The profiles along the jet axis of the previous distributions evidence the axial velocity decrease that starts at the end of the potential core and the increase of the turbulence level along the axis (Figure 46). The axial velocity measured with the hot-wire can be compared with the same measurements performed with the Pitot tube.

The hot-wire error can be estimated about 1% (Jullen 1978) instead the Pitot tube introduces an interference error previously evaluated near the 5%. The Figure 47 shows the comparison of the non-dimensional velocities on the jet axis measured with hot-wire and Pitot tube. Figure 47 shows a good correspondence of the two measurements though the Mach numbers of the two tests are different.

Figure 48 shows the skewness and the Kurtosis along the jet axis. As described above, the maximum value of the Kurtosis locates the end of the potential core at a distance of about 4 diameters from the exit.

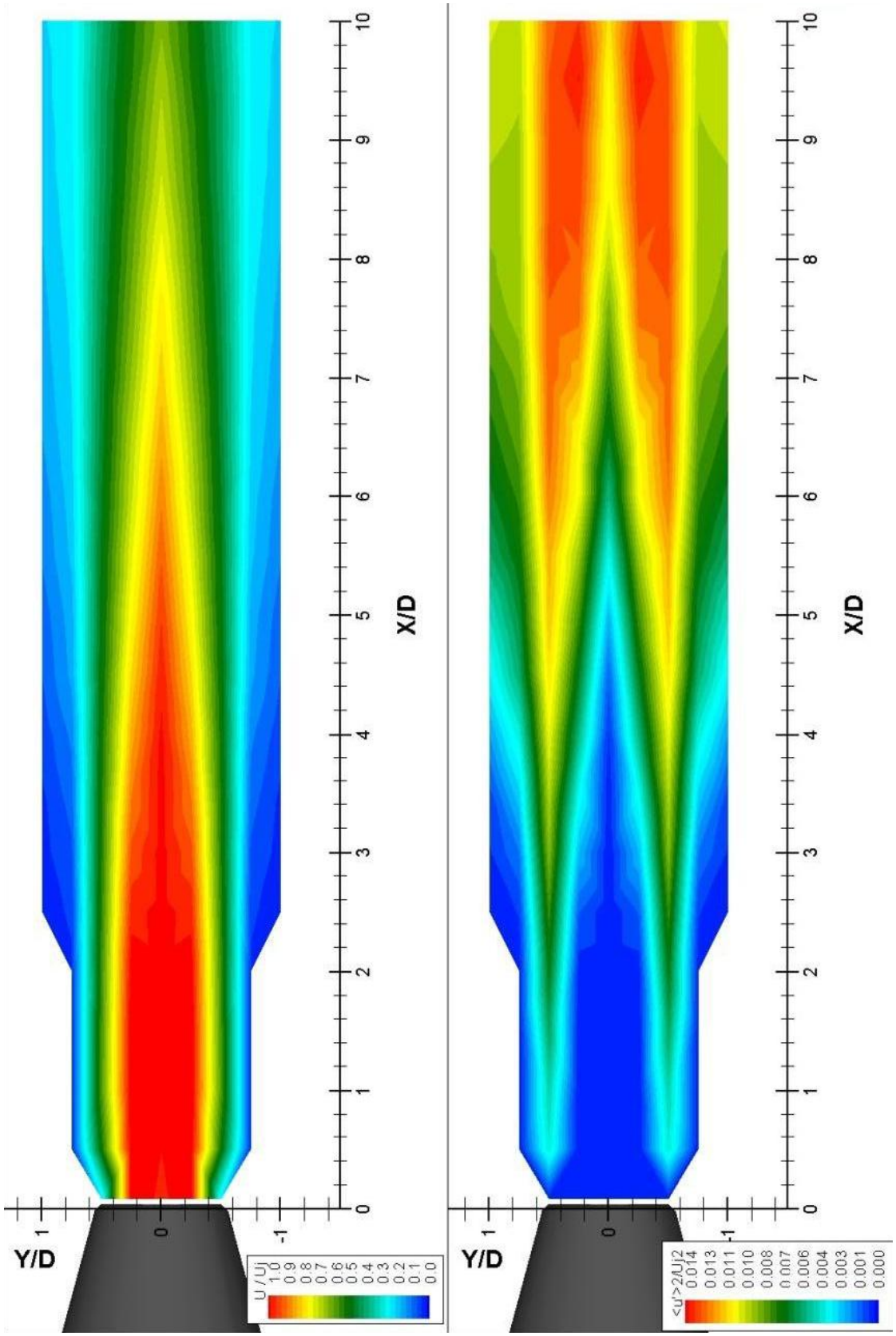

Figure 44: Velocity and Reynolds stress distributions on a symmetry plane.

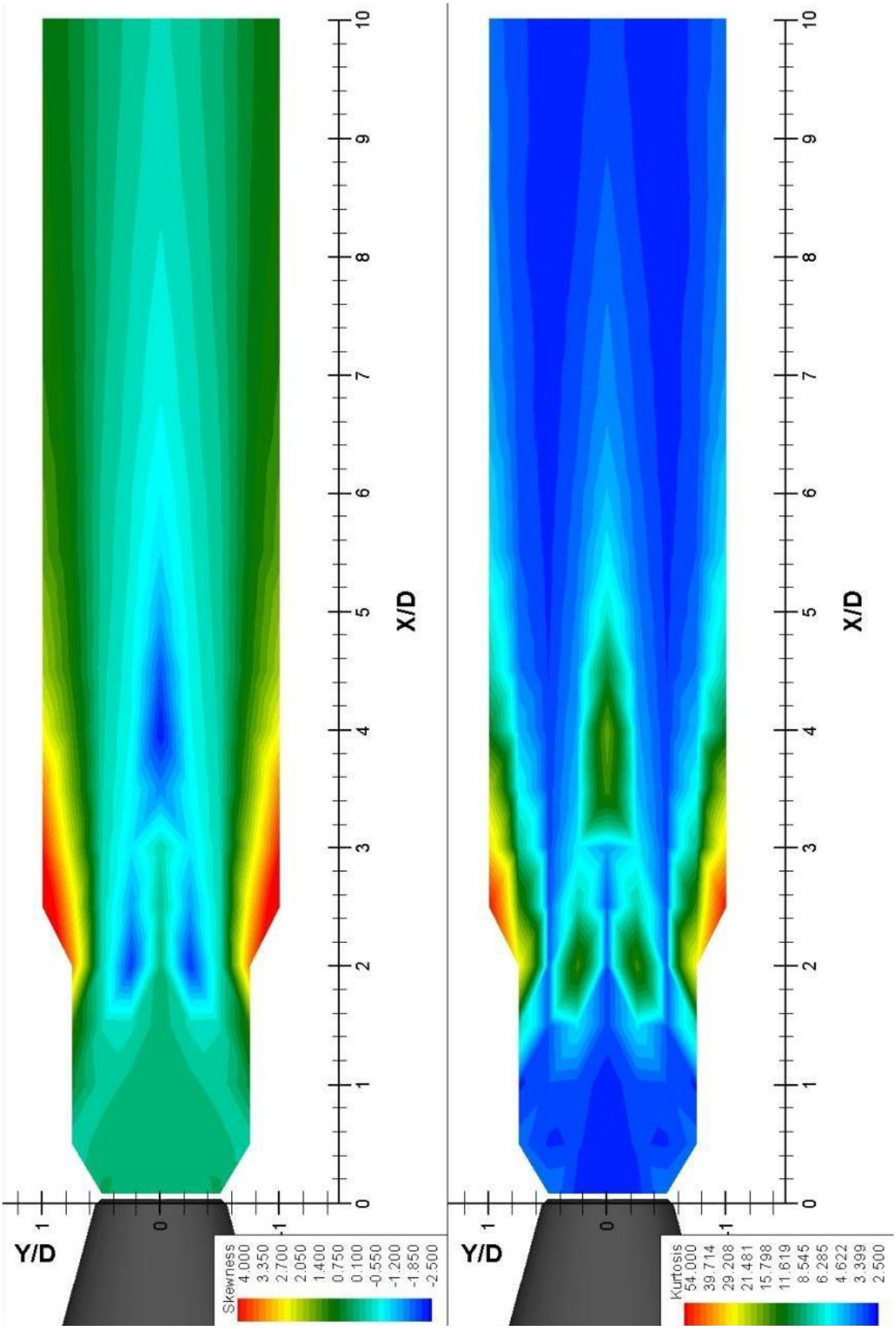

Figure 45: Skewness and Kurtosis distributions on a symmetry plane.

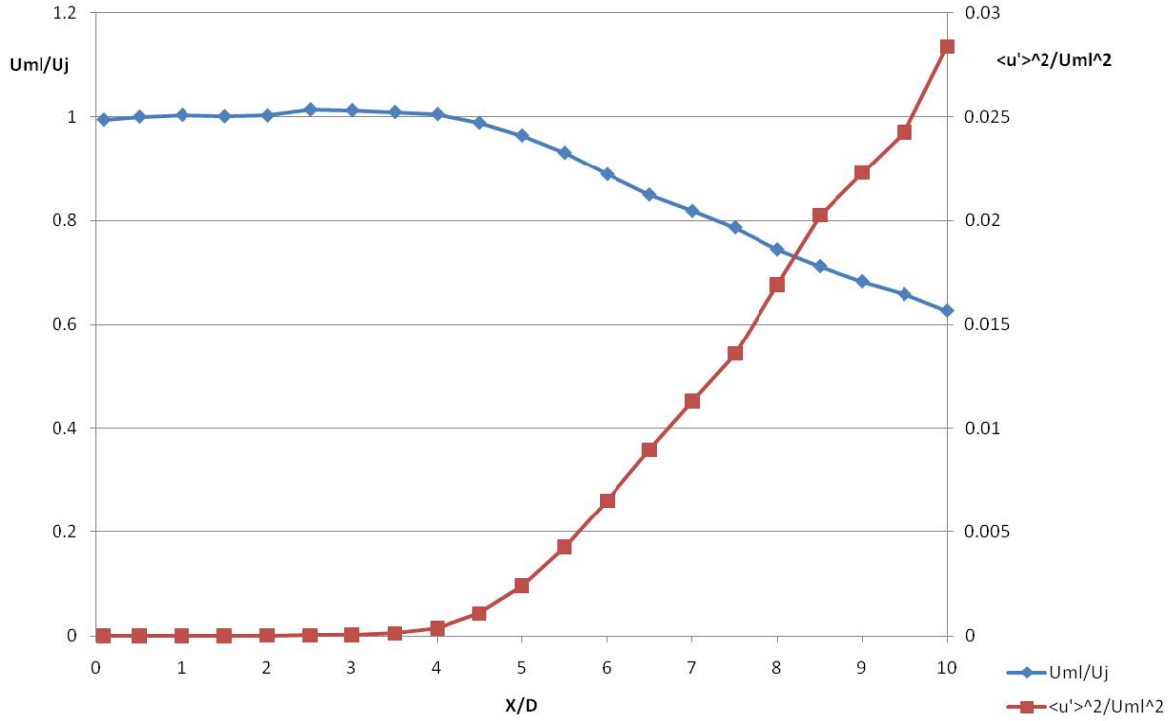

Figure 46: Velocity and turbulence profiles in correspondence of the jet axis.

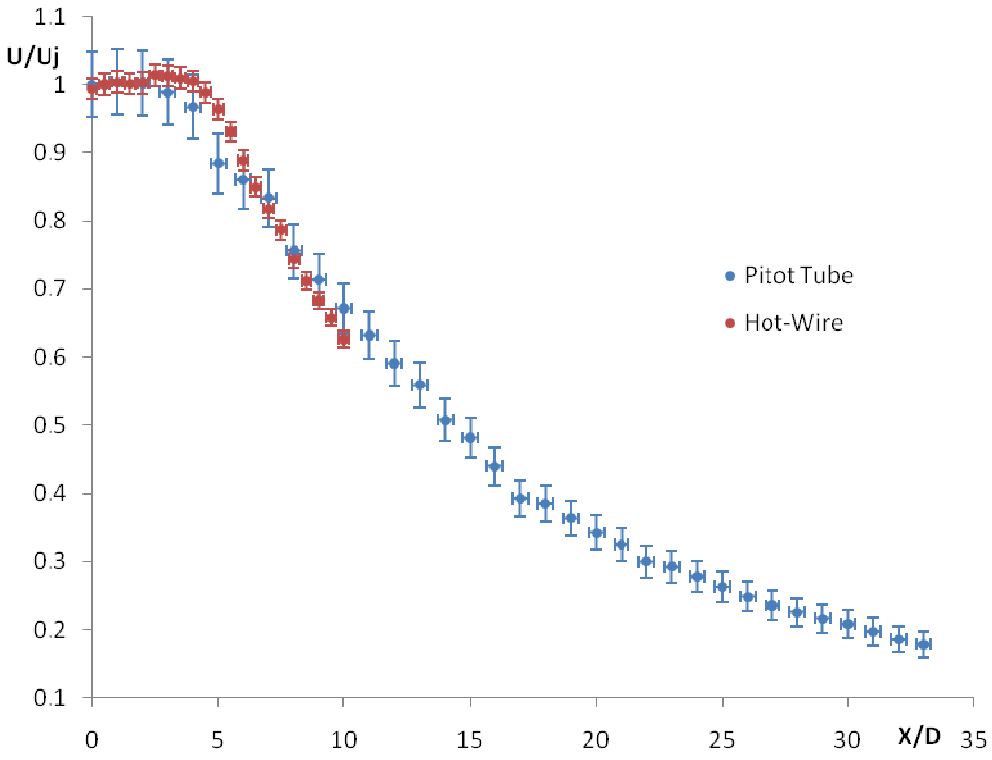

Figure 47: Axial velocity comparison of Pitot tube and Hot-wire.

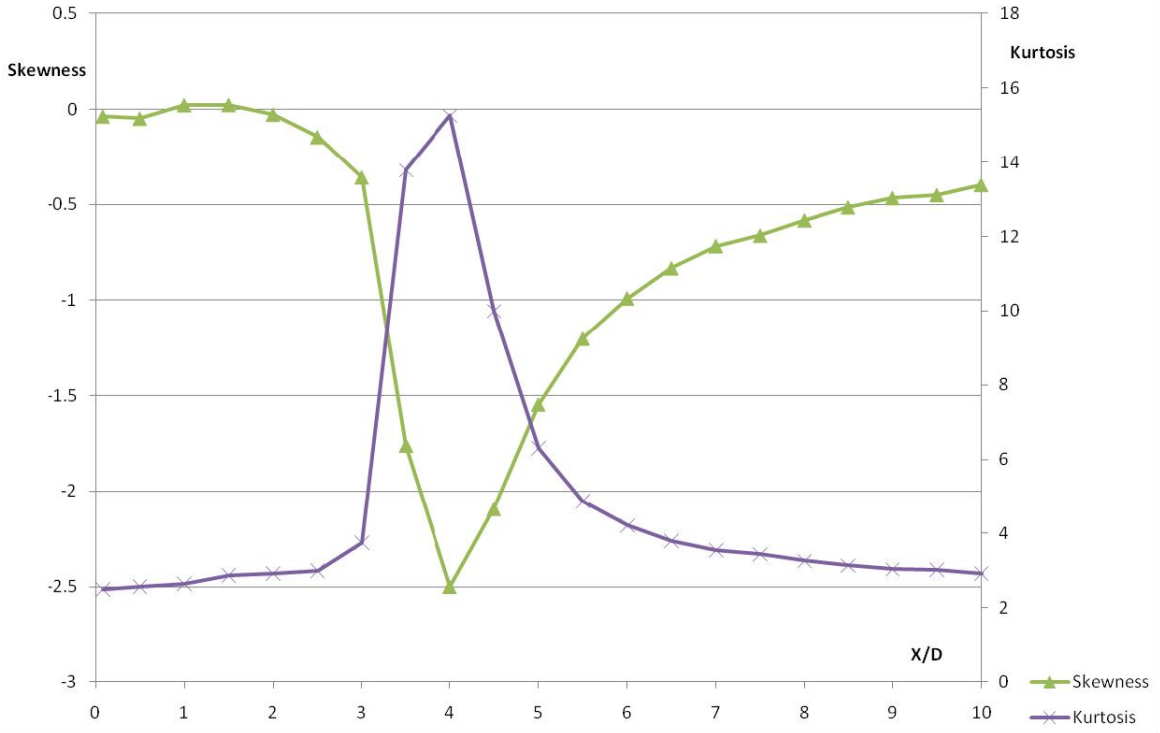

Figure 48: Skewness and Kurtosis on the jet axis.

5.2 The acoustics of the Jet Far-field

The Far-field acoustic qualification is performed using a Brüel & Kjær ¼" 4939 microphone mounted on a wood strut partially covered by acoustic absorbent material to reduce any sound reflection. The used sampling rate is 500 kHz to exceed the Nyquist's theorem for the maximum filter frequency of 100 kHz set to use the full frequency range of this kind of microphones. The far-field is mapped for two conditions at Mach 0.5 and Mach 1 and at two radial distances at 90 and 120 diameters from the nozzle. Figure 49 shows the microphone positions for the far-field measurements.

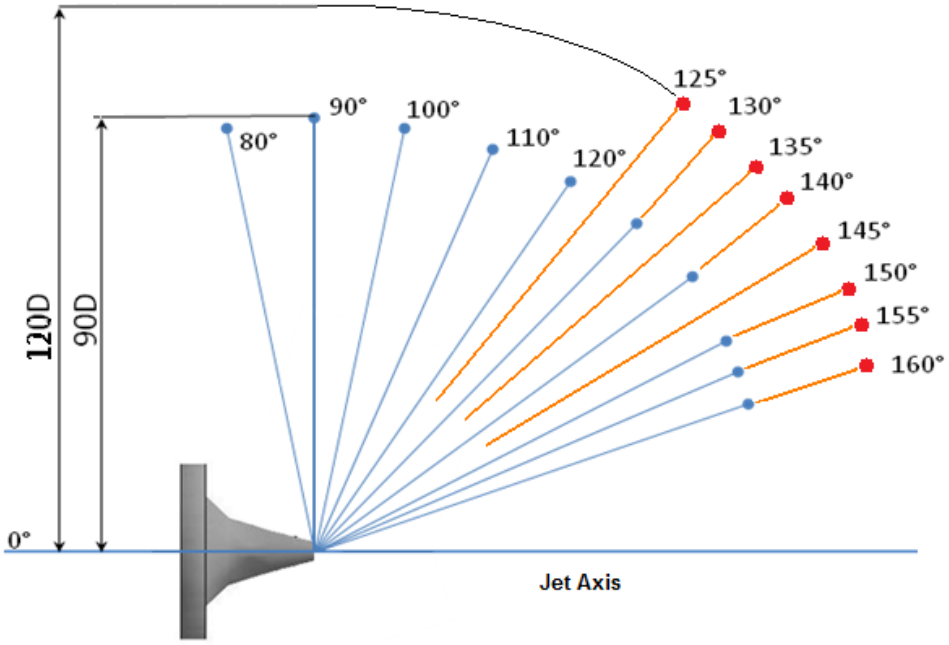

Figure 49: Microphone positions for the Far-field measurements.

The "Overall sound pressure level" (OASPL) is a first element for the jet far-field noise estimation. The OASPL is defined as:

$$OASPL = 10 \log E \qquad \text{Eq. 14}$$

Where ***E*** is the total sound energy that is defined as:

$$E = \int_F \left(\frac{p(f)}{p_0}\right)^2 df \qquad \text{Eq. 15}$$

The term $p(f)$ is the measured pressure in the frequency domain and p_0 is the reference pressure that is the audible threshold at 1 kHz and is $p_0 = 2 * 10^{-5}$ Pa. From Eq. 14 the OASPL is evaluated both for the full signal and for the signal filtered in the frequency range of the microphones (20 Hz – 100 kHz).

Figure 50 shows the OASPL directivity measured at a distance of 90 and 120 diameters and at Mach numbers of 0.5 and 1. The maximum OASPL for the filtered signal is located around 130 – 140° for Mach 0.5 and around 140 – 150° for Mach 1; for the full signal (Raw in the

Figure 50) the maximum directivity is around 155° at Mach 1 and 160° for the Mach 0.5. The slightly different directivity of the filtered and Raw OASPL in Figure 50 is evident; the raw directivity is influenced by frequencies external to the filter that are unreliable for the characteristics of the microphones and of the signal conditioner.

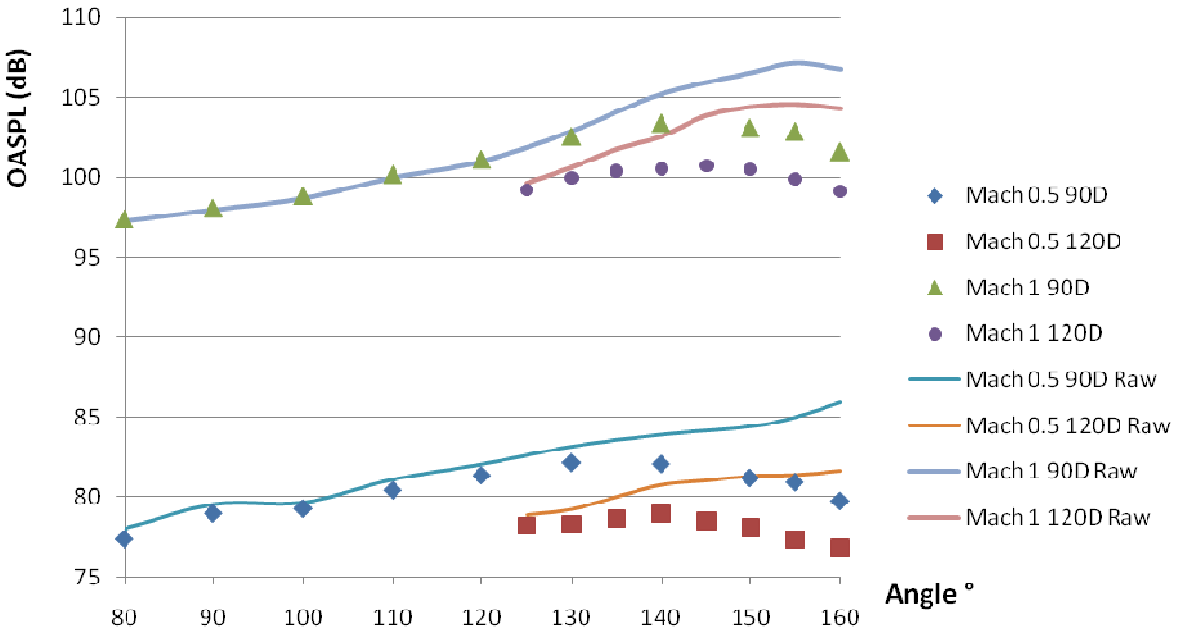

Figure 50: OASPL of the Jet: directivity in the far field.

Figure 51 shows the directivity angle for a jet at Mach 0.5 and 0.9 extracted from the work of Tanna (1977), with angles adapted to the convention adopted therein; the similitude with the Figure 50 is evident. The continuous lines in Figure 51 represent the directivity evaluated with the freely-convected quadrupole model.

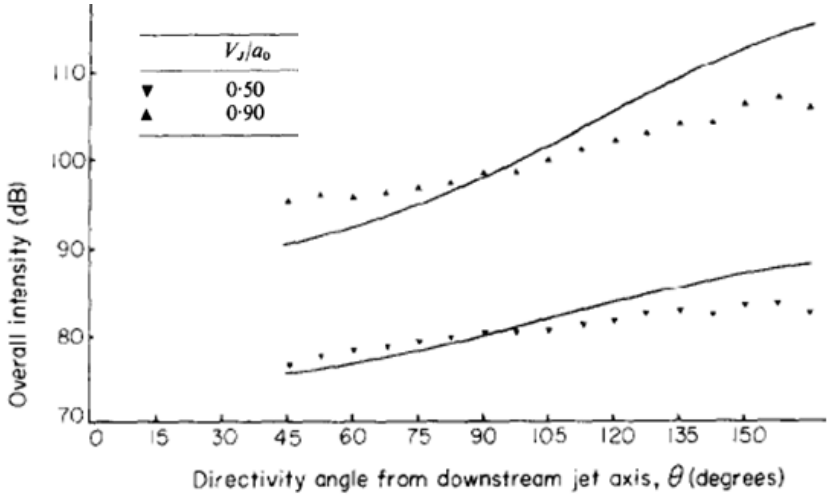

Figure 51: OASPL directivity of the jet (Tanna, 1977)

The selective directivity of the various frequencies can be underlined dividing the OASPL in 1/3 octave band and taking only the sound energy contribution around some interesting Strouhal numbers. Figure 52 shows a comparison of the 1/3 octave band directivity with analogous results from the work of Tanna (1977). The similarities are evident as well as the different directivity for different Strouhal numbers. The low frequencies (St= 0.1 and 0.3) propagates at higher angles while the high frequencies (St= 1 and 3) have a maximum directivity around 130° and 140°.

As said by the two sources theory (Tam et Al. 1996) the noise at low angles depends mainly by fine scale turbulence (higher Strouhal numbers) and at high angles depends by large scale structures (lower Strouhal numbers).

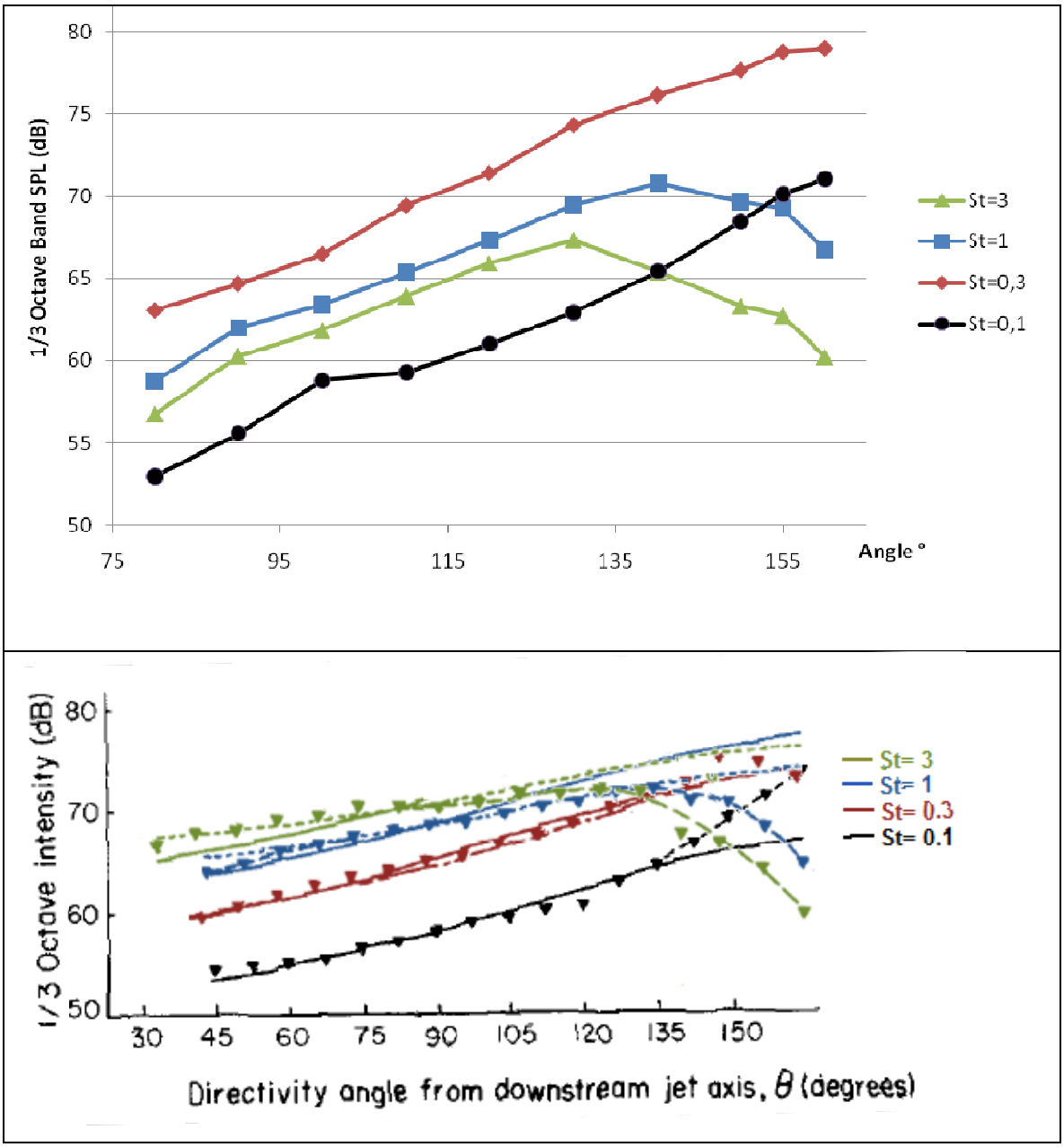

Figure 52: Comparison of the 1/3 Octave band directivity of the present work on the top with the work of Tanna (1977) on the bottom.

Tam et Al. (1996) proposes also analytical solutions for the sound spectra depending on the scales. The so called similarity spectra equations are:

$$SPL = 10\ log\left[\frac{A}{p_0^2}F\left(\frac{f}{f_l}\right) + \frac{B}{p_0^2}G\left(\frac{f}{f_f}\right)\right] - 20\log\left(\frac{r}{D}\right) \qquad \text{Eq. 16}$$

A and ***B*** are the similarity parameters that depend on the jet temperature and the Mach number and f_l and f_f are the main frequencies for large and fine scales. ***F*** and ***G*** are the large scale and fine scale spectral functions respectively (Tam et Al. 1996). The main influence of the ***F*** function is near 150° and the main influence of the ***G*** function is near 90°. From the work of Tam et Al. spectra at different angles are described as a sum of large and fine scale effects (Eq. 16). Figure 53 shows a measured spectrum at Mach=1 in the far-field at 90° angles 90D from the nozzle compared with the **G** function of Eq. 16 that describes the fine scale spectra.

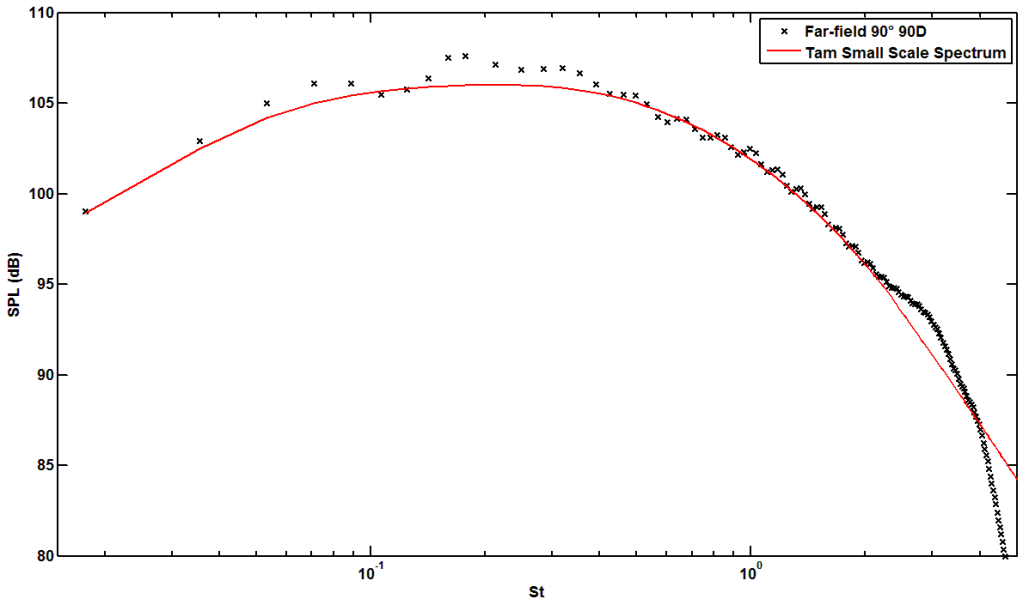

Figure 53: Mach1, 90° far-field spectrum compared with fine scale spectrum.

Figure 54 shows a measured far-field spectrum at Mach=1 at 150° and 90D compared with the ***F*** function of Eq. 16 that represents the effects of large scale structures. Again, a good correspondence is observed. The effect of the directivity on the power spectral density is shown in Figure 55. This figure shows how the spectra are influenced by the directivity at Mach=1. The spectra shape changes from fine scale type situations (80°, 90° and 120°) to large scale type (155° and 160°) with the maximum value that increases with the angle. The spectrum at 140° seems a combination of large and fine scales spectra.

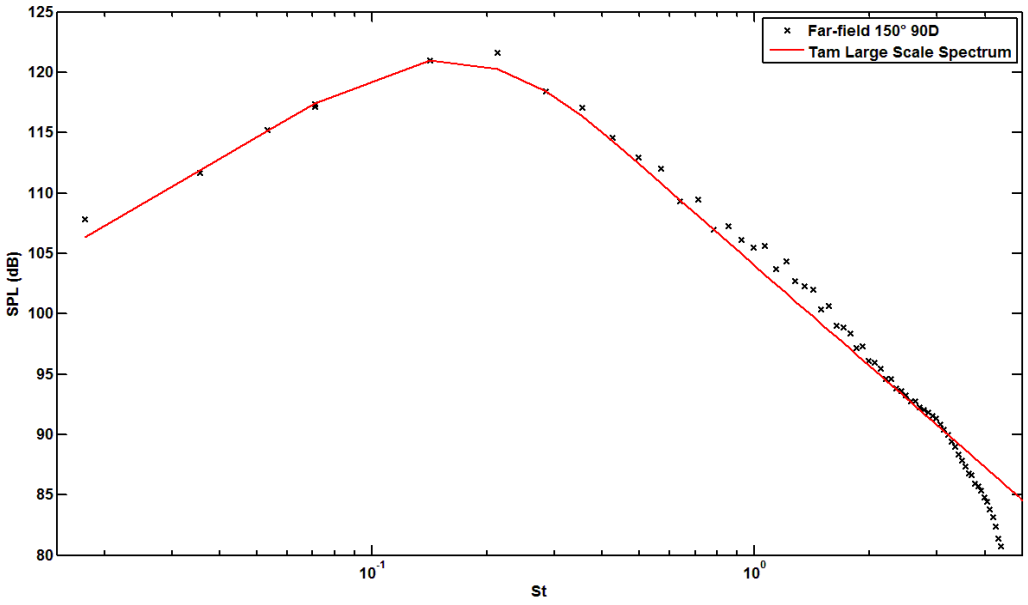

Figure 54: Mach 1, 150° far-field spectrum compared with large scale spectrum.

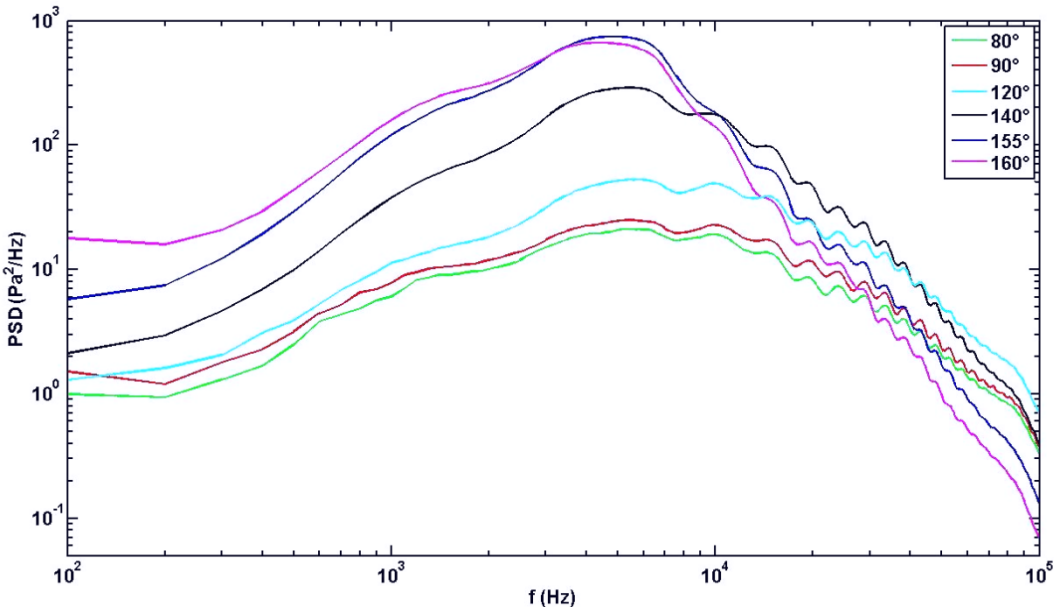

Figure 55: Mach1, Spectral variations with the directivity angle, 90D from the jet exit

Other interesting aspect is the effect of the Mach number to the far-field spectra. Figure 56 - Figure 58 show the far-field spectra variation with Mach respectively at 90°, 130° and 155° at 90 diameters from the jet exit. The shape of the spectra doesn't change with the Mach

number, while the maximum sound pressure level and the corresponding dimensional and non-dimensional frequency changes.

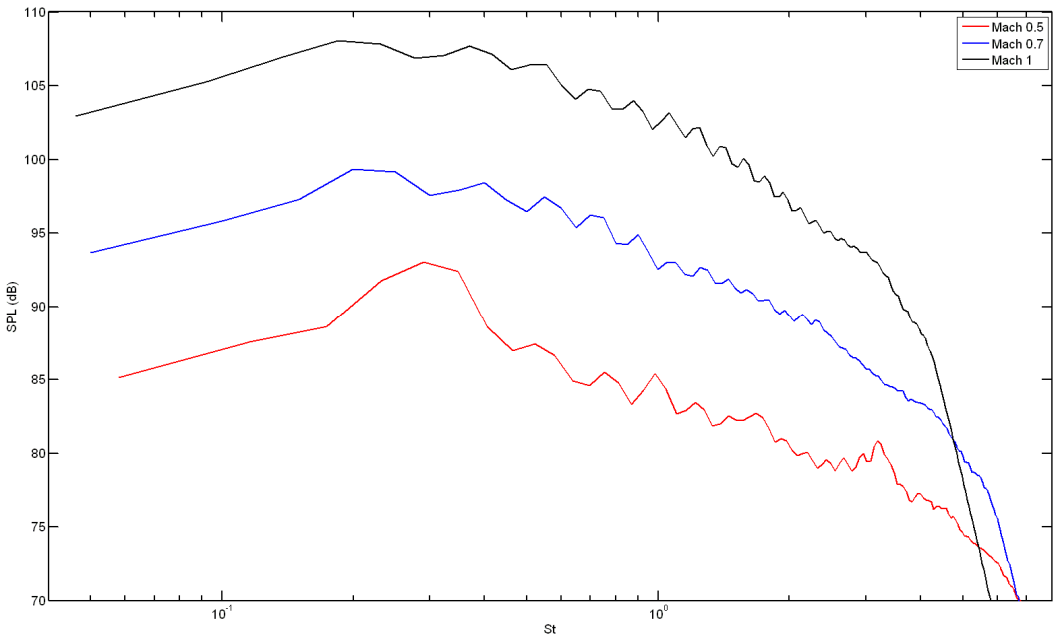

Figure 56: Effect of the Mach number to 90° spectra, 90D from the jet exit

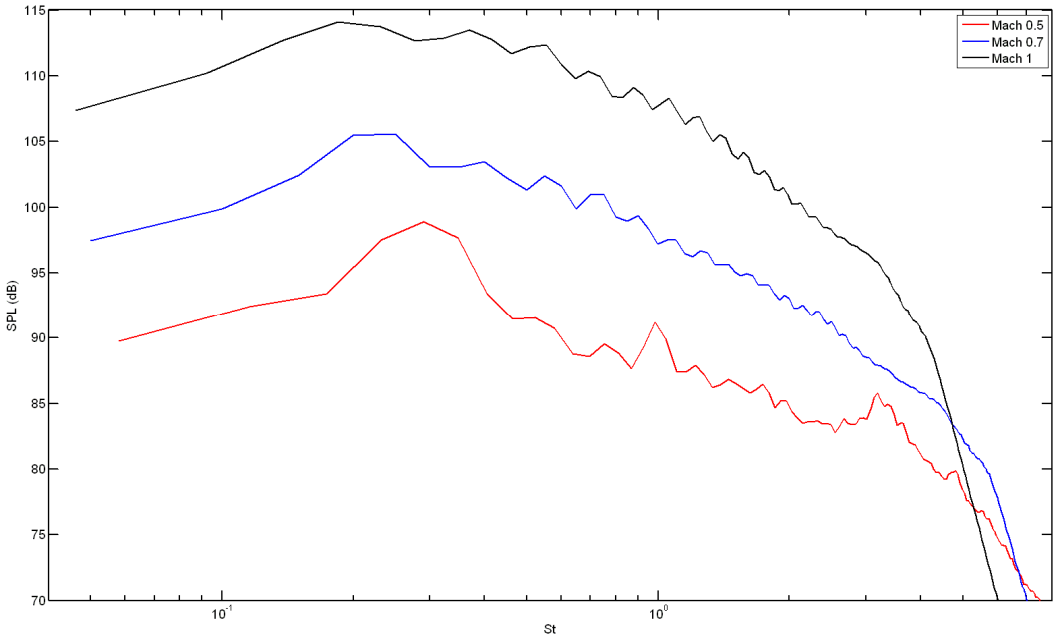

Figure 57: Effect of the Mach number to 130° spectra, 90D from the jet exit

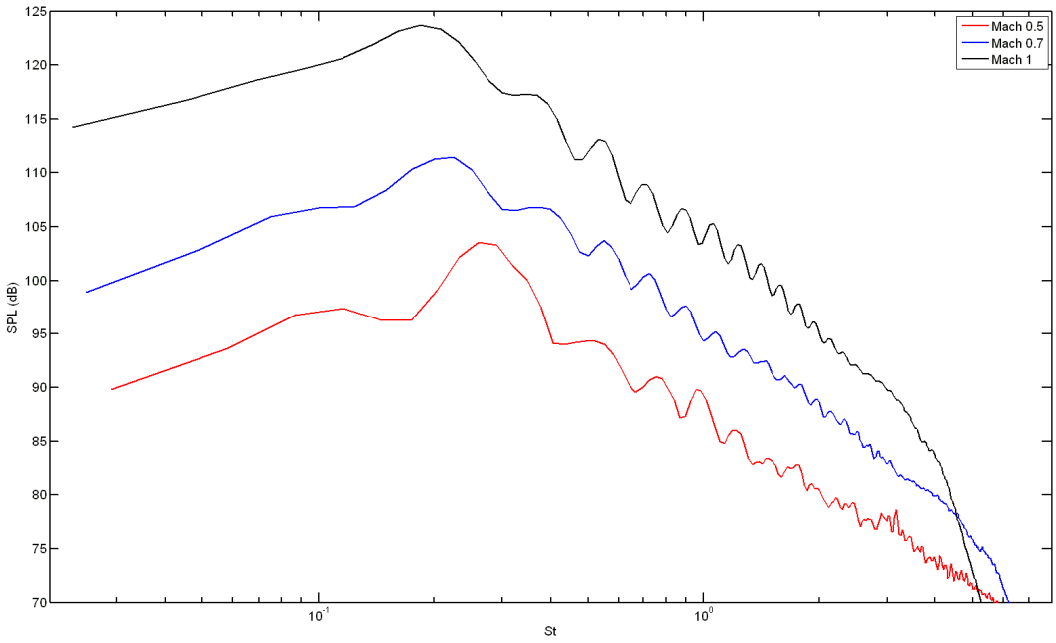

Figure 58: Effect of the Mach number to 155° spectra, 90D from the jet exit

The maximum SPL peak has been extracted and the dependence on the Mach and the angle is given in Figure 59. It is evident that the SPL increases with mach are different with the directivity. (see Figure 59)

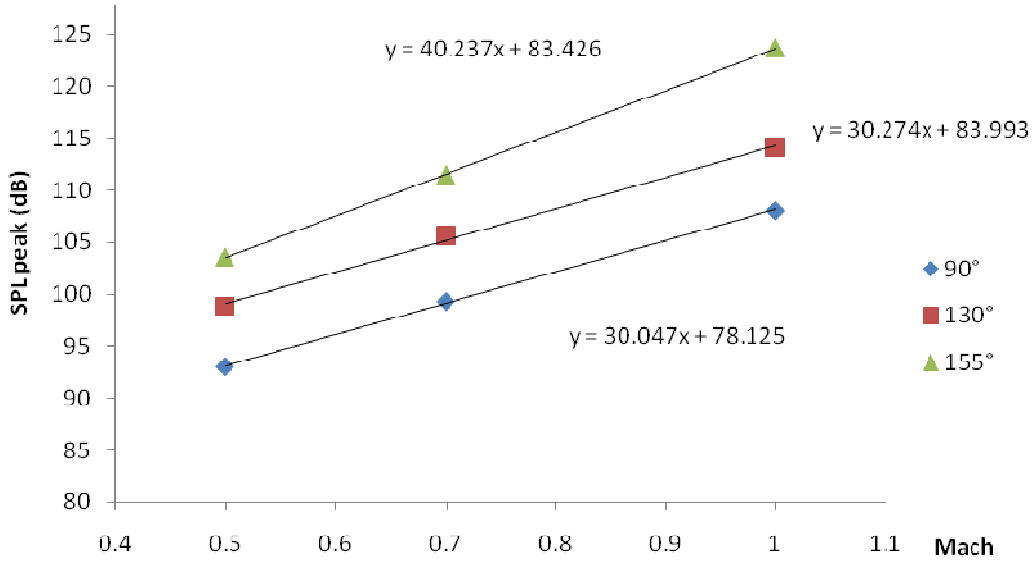

Figure 59: SPL variation with the Mach number and the angle.

Figure 59 shows the increase of the SPL peak with the Mach number for different angles, is evident that the increase depends strongly by the Mach number but also by the directivity. At 155° the SPL increases higher than at 130° or 90°. The spectra at 90° and 130° are similar to fine scale spectra and their SPL increase is lower than the spectra at 155° that seem typical large scale spectra. For this reason is evident that the large scales are influenced by the Mach number more than the fine scales.

The measurements for qualify both jet flow-dynamics and acoustics demonstrate a strong similarity with literature data; the nozzle generates a typical jet-flow with strong directivity and well-known far-field noise characteristics.

The full data of the far-field are shown in Appendix B.

6 Near-Field Pressure Fluctuations

In this chapter the near-field pressure fluctuations are examined applying the wavelet filtering algorithm to distinguish the sound and the pseudo-sound. The near-field measurements are performed at Mach=0.5 using simultaneously a couple of B&K 4939 microphones mapping a planar zone from 1 to 7 diameters in the radial direction and from 0 to 22 diameters in the axial direction with an angle of 10° respect the jet axis. The microphones are mounted on a wood strut that moves to the measurement points maintaining the two microphones at a distance of 14 mm. The signals are acquired with a sampling frequency of 500 kHz.

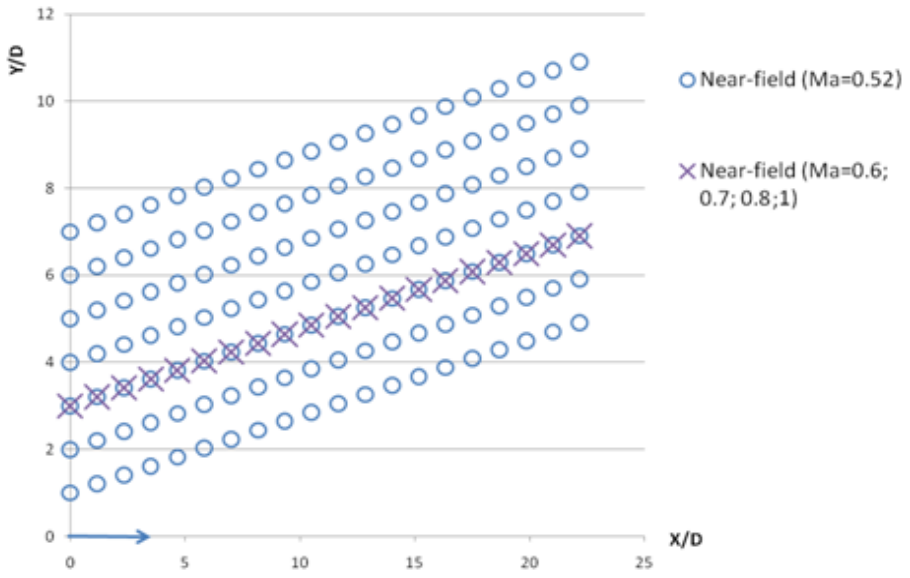

Figure 60: Microphone positions for the near-field measurements.

Other measurements were performed at Mach 0.6, 0.7, 0.8 and 1 on a 10° line respect to the jet axis at a radial distance of 3 diameters and from 0 to 22 diameters from the jet exit section in the axial direction (see Figure 60).

6.1 Near-field characteristics

As previously mentioned, a microphone in the near-field measures both sound and pseudo-sound (Ffowcs-Williams 1992). The acoustic field is combined with the pressure fluctuations that are convected in the flow. The measured OASPL in the near-field seems to lose the typical directivity of the jet; in fact the sound level lines are parallel to the flow shear layer that has an aperture angle of about 10°. Figure 61 shows the near-field OASPL distribution around the jet.

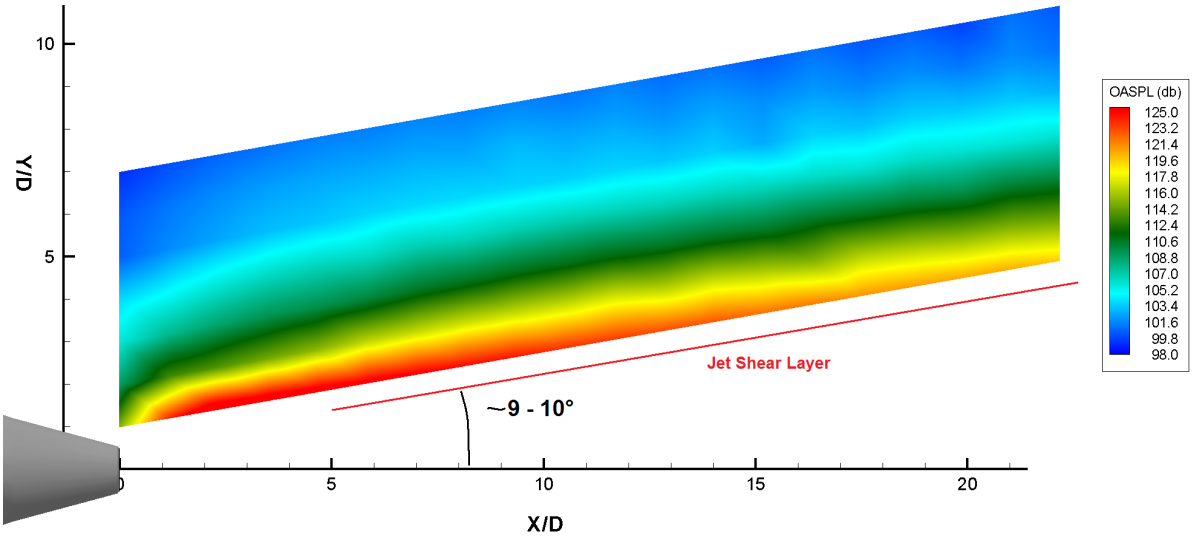

Figure 61: Near-field OASPL distribution.

The directivity of the jet is usually selective with the frequencies and is possible to locate it analyzing the distribution of 1/3 octave SPL for some typical Strouhal numbers as 0.1 and 0.3 for the low frequencies and 1 and 3 for the high frequencies. Figure 62 shows the SPL distributions for low Strouhal numbers, evidencing directivity effects. From Figure 62 (top) is evident how the smallest scales propagate in a direction partially parallel to the shear layer but have a radial distribution with an ideal center at about 7 or 8 diameters; moving away from the ideal origin point is evident how the iso-sound curves are extended in the flow direction. Also at St=0.3 the directivity starts to have a particular radial distribution of the

sound level with an approximate center at 3 – 4 diameters on the jet axis and with the same elongation in the flow direction of the iso-sound curves.

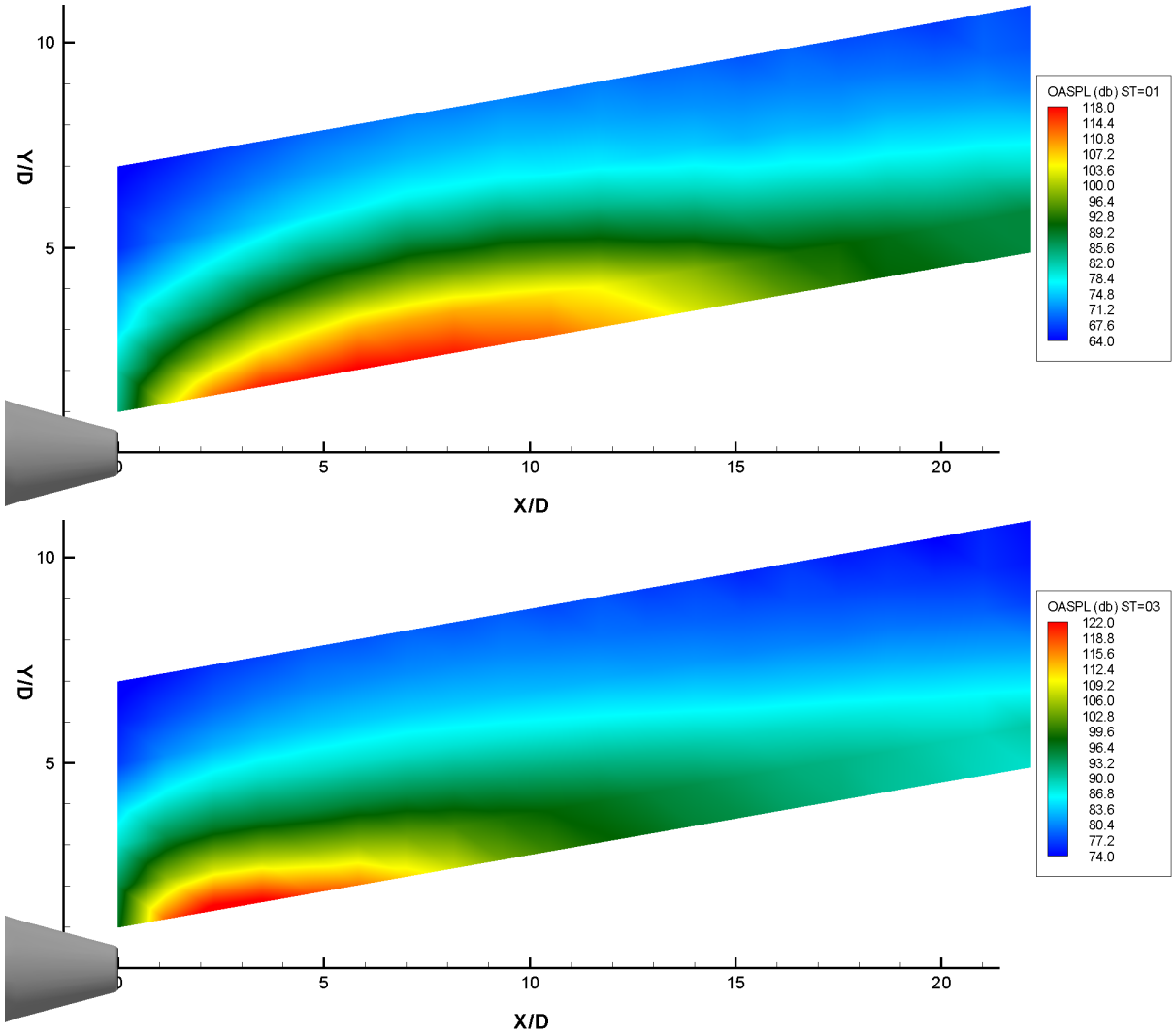

Figure 62: SPL for 1/3 octave at St=0.1 (top) and St=0.3 (bottom)

The same details are shown in Figure 63 (top). The SPL around the 1/3 octave band of St=1 has a shape similar to that at St=0.3. The difference with respect to the case St=0.3 is the evident propagation in the direction highlighted with an arrow in the figure. Figure 63 shows also the distribution of SPL at St=3 (bottom); the higher frequencies have an ideal origin around 1 or 2 diameters on the jet axis. The propagation of these frequencies is preferential

in the low angles direction as evident by the iso-sound levels of Figure 63 (bottom). A deformation in the flow direction is also shown in the same figure but only very close to the shear layer.

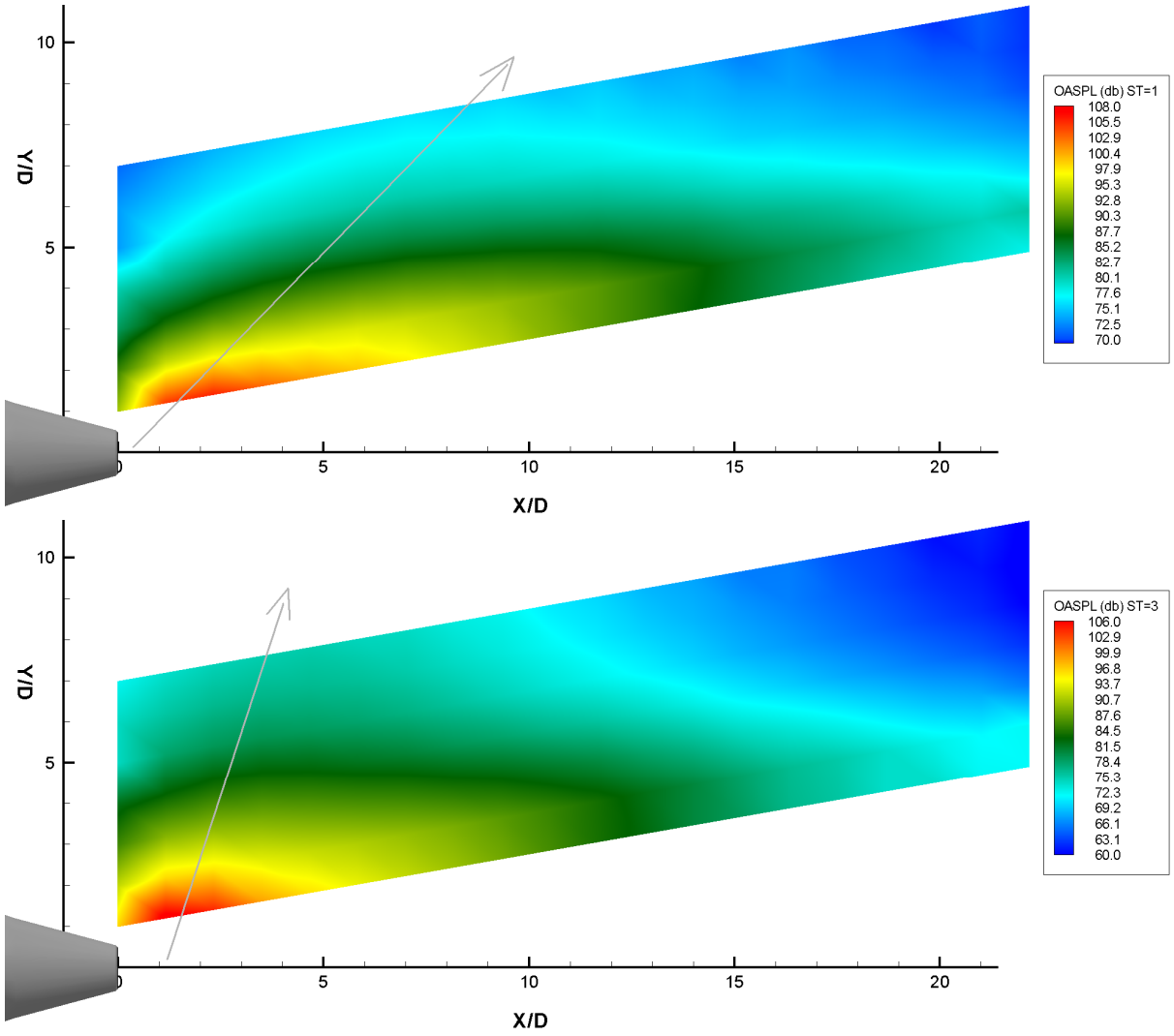

Figure 63: SPL for 1/3 octave at St=1 (top) and St=3 (bottom)

Even if the 1/3 octave division offer indications on the selective directivity at different frequencies, this type of simple filtering avoids the identification of sound and pseudo-sound and the study of their spectral components. The near-field spectra are different from the far-field and this difference is dependent on the presence of strong pseudo-sound components.

Figure 64 shows some near-field spectra from points in the near-field. The spectra around 150°-160° have similar shapes (Figure 64 top), as the spectra at angles lower than 140° (Figure 64 bottom).

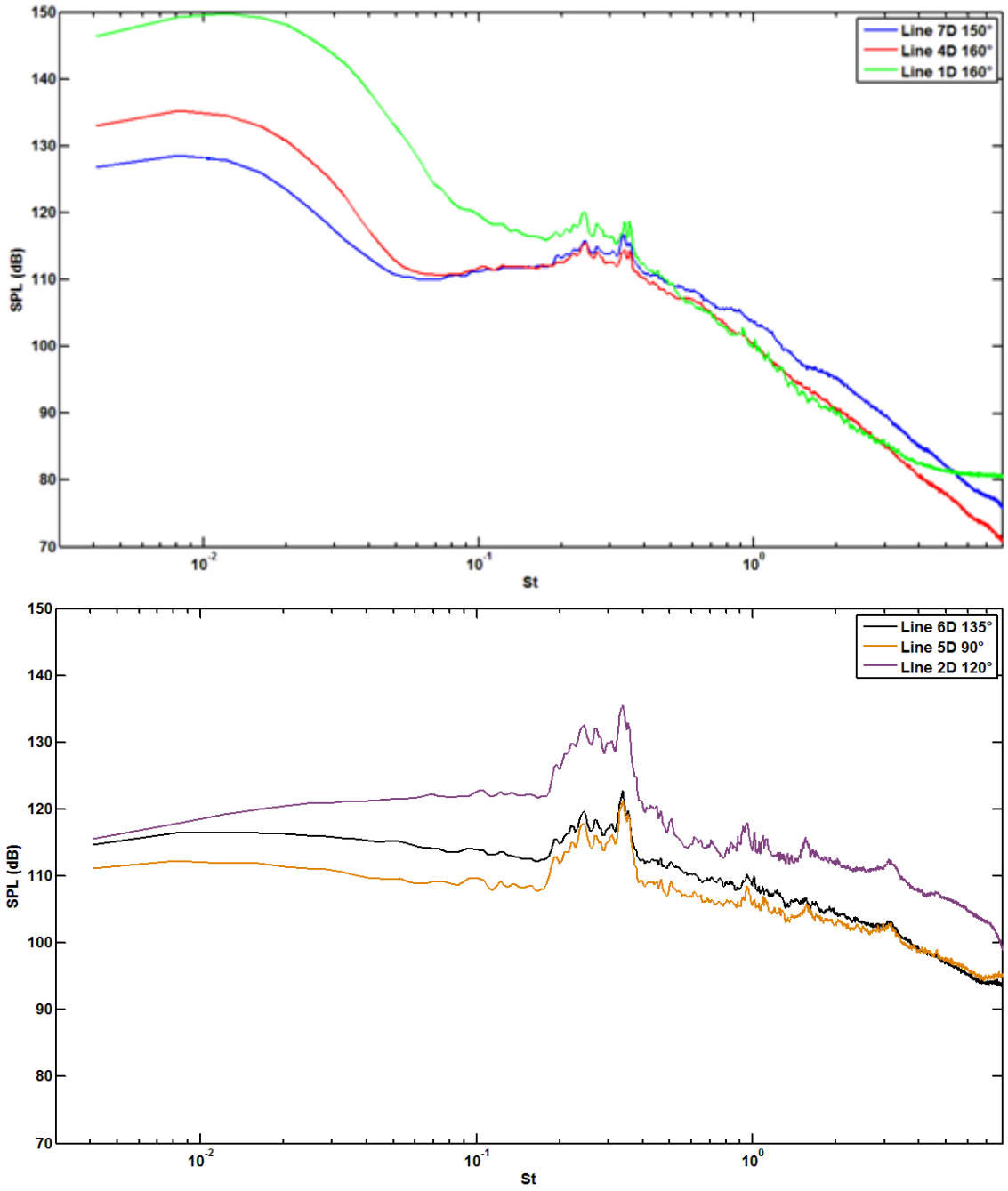

Figure 64: Near-field spectra comparison: maximum directivity angles (top); lower angles (bottom)

Moreover at medium and high frequencies (St>0.2) these spectra seem similar with those measured in the far-field at the same angles; while they are quite different at low frequencies components (St < 0.1).

6.2 Near-field wavelet filtering

The algorithm described in the Chapter 3 is applied to the near-field measurements. The pressure signals, acquired simultaneously with two microphones at a fixed distance, are filtered using the wavelet. Pseudo-Sound Pressure Level is defined at the same manner as the OASPL to compare the effects of sound and pseudo-sound (Eq. 14 and Eq. 15). Figure 65 shows the Pseudo-Sound pressure level distribution on the measurement zone.

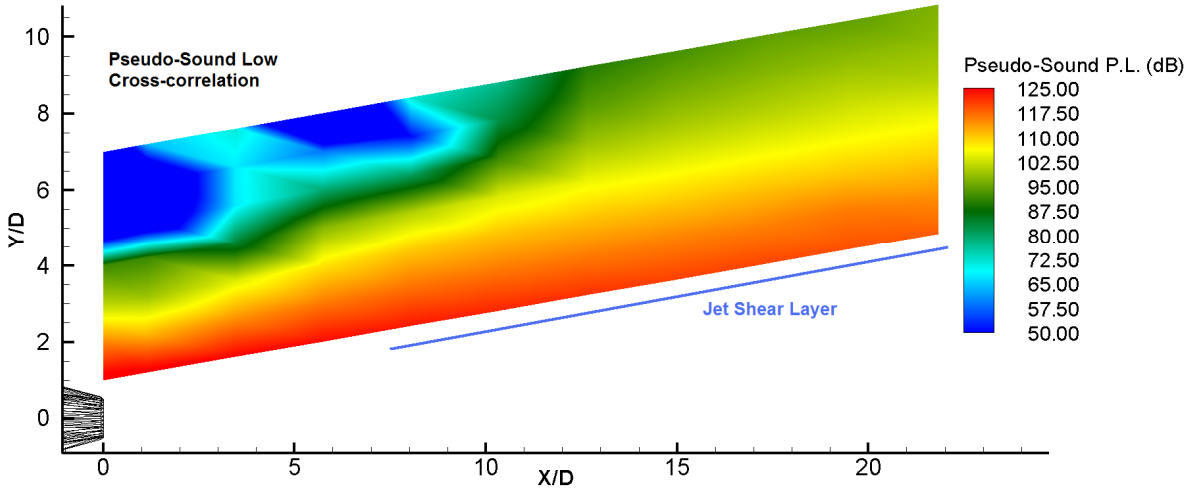

Figure 65: Pseudo-Sound pressure level distribution.

As shows in Figure 65 the pseudo-sound pressure level propagates with an angle slightly smaller than the jet shear layer in the zone of maximum intensity. Moving far from the axis the intensity decreases quickly and the angle with respect to the jet axis increases. In the same figure is also evident a zone where the pseudo-sound pressure level is lower than 50

dB. That zone can be considered as unaffected by the jet pressure fluctuations and undisturbed.

One of main filtering parameters is the convective velocity of the pseudo-sound. The Figure 66 shows the convective velocity distribution with respect to the jet velocity. The line of maximum convective velocity depends on the propagation direction of pseudo-sound pressure fluctuations. In fact in this zone the main velocity component isn't parallel to the microphones line, which is tilted of 10° respect the jet axis, so the flow experiences an apparent distance lower than the microphone separation (14 mm).

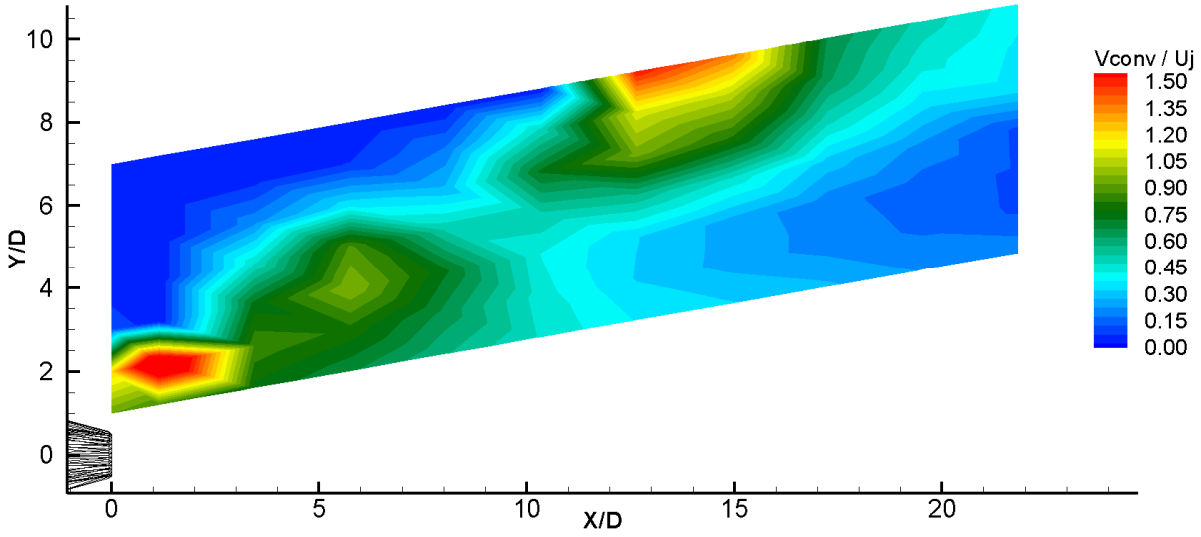

Figure 66: Pseudo-sound convective velocity distribution

Below this maximum velocity line, the propagation direction of the pressure fluctuations is parallel to the microphones line and the convective velocity is "*very much smaller than the sonic velocity*" (Ffowcs-Williams 1992). Above this line there is the weak correlation zone and the flow can be considered undisturbed and the convection velocity is close to zero. A useful evaluation of the convective velocity can be done by extracting axial and radial profiles. Figure 67 shows the axial decrease of the convective velocity along a line at 1 D from the jet axis.

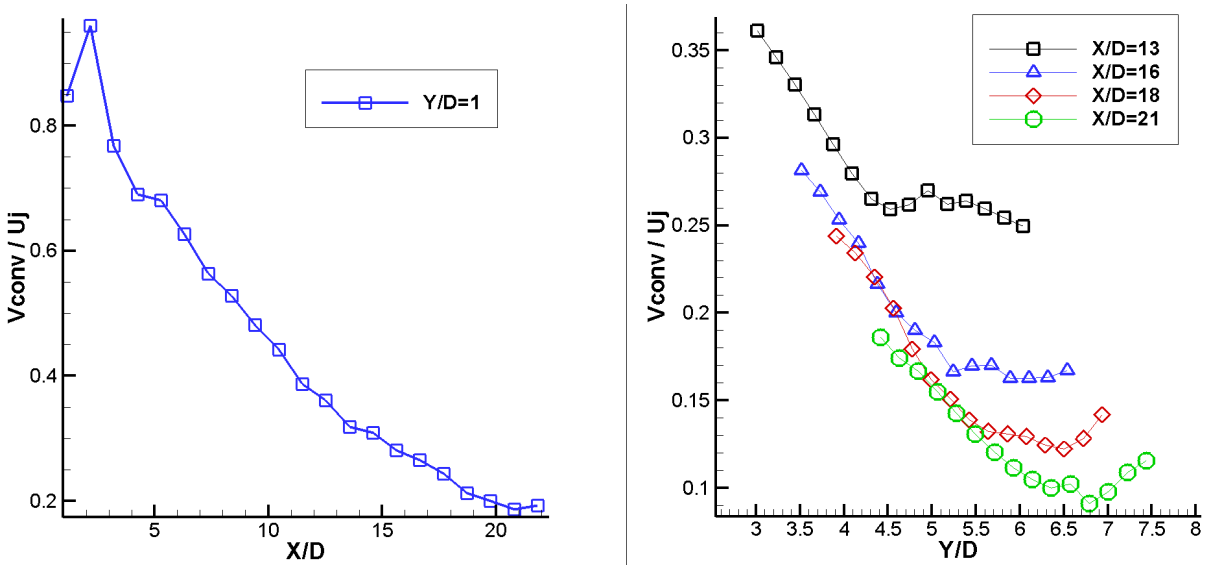

Figure 67: Convective velocity profiles: decreasing on 1D line (left); some radial distributions (Right)

Figure 67 also shows radial profiles of the convective velocity extracted from the zone below the line of the maximum velocity. That looks similar to the tails of the self-similar jet velocity profiles (Rajaratnam 1976 and Figure 5). Figure 67 shows a strong similarity of the pseudo-sound convective velocity with the jet velocity characteristics, and highlights the good efficiency of the wavelet algorithm.

The wavelet algorithm gives the Sound part of the signals that propagates at sound speed and Figure 68 shows the OASPL distribution of the sound pressure fluctuations. The gray arrow highlights the maximum propagation direction that corresponds to an angle between 130- 150° as usually found in the far field directivity. From Figure 68 it is also evident a zone where sound is very low, in the right part of the figure. This can be considered a silent zone where the OASPL is 15 - 20 dB lower than the rest of the field, and corresponds to a peripheral part of the “cone of silence” that depends by the refraction of the sound in the jet flow (Atvars et Al. 1964 and Tanna 1977).

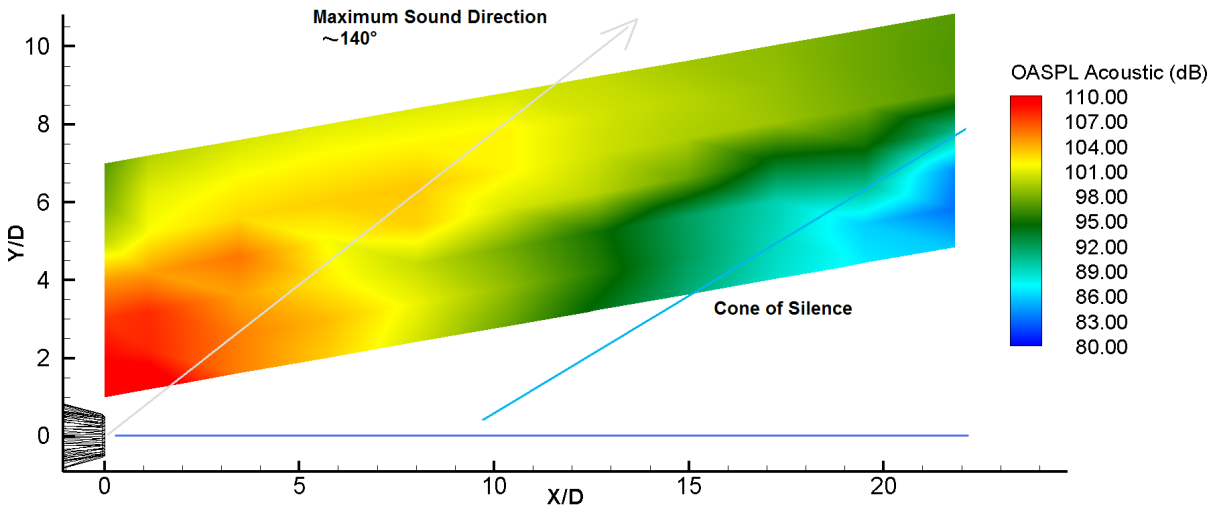

Figure 68: Sound OASPL distribution.

The near-field directivity can be compared with the far-field extracting some profiles of the near-field sound pressure level along concentric arcs with a radius from R=5D to R=16D. Results are presented in Figure 69, where the main sound direction is 125°, very close to the jet and becomes 145° moving away from it. In addition is necessary to study the directivity of spectral components Figure 70 shows the Strouhal number corresponding to the maximum spectral sound energy. Some typical directions and some interesting points are also drawn in the figure. The acoustic peaks around the maximum propagation direction from 140 ° to 150° have Strouhal number in the range 0.1 – 0.3 (see Figure 70).

At angles lower than 130° the peaks are at St ≈ 0.4. Figure 70 shows also that in the cone of silence the sound peak Strouhal number is greater than 1. Comparing this figure with the sound directivity of Figure 68 it is evident that the maximum directivity depends on the large scales that propagate acoustic energy while in the cone of silence the noise is radiated at very higher frequencies and smaller scales.

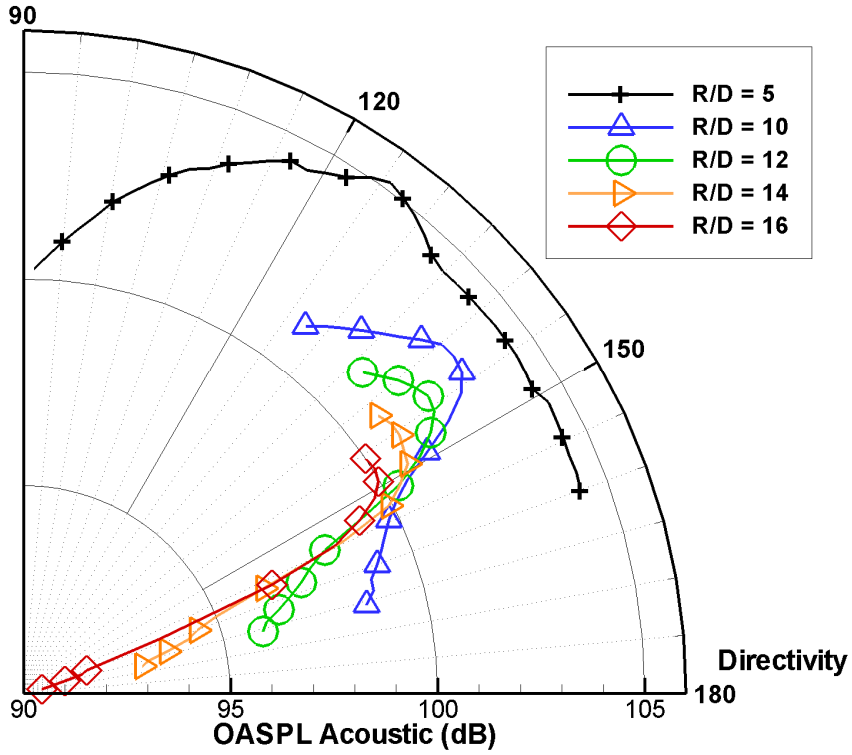

Figure 69: Near-field OASPL: Directivity profiles

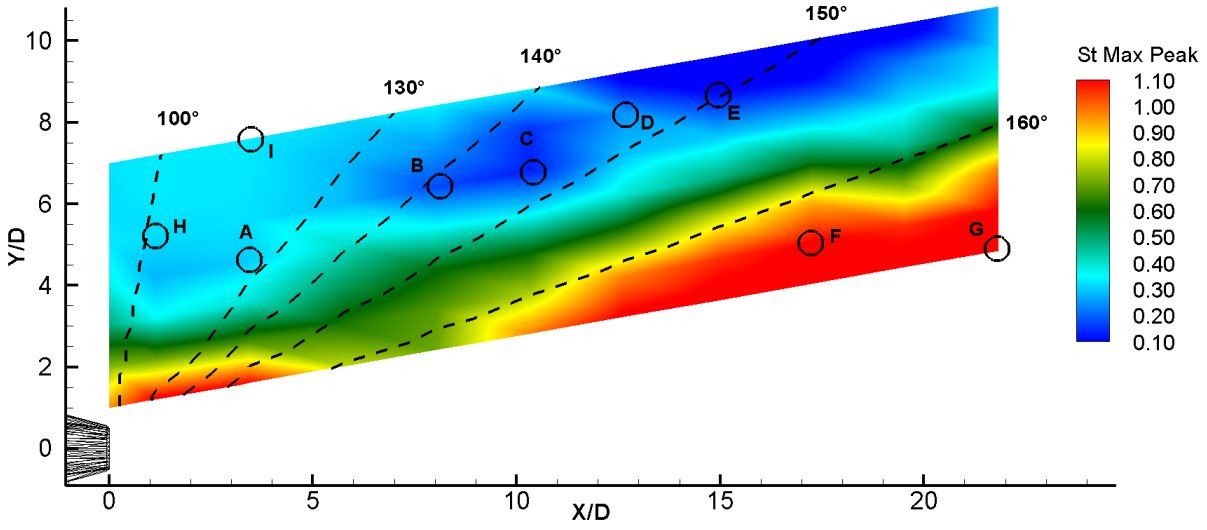

Figure 70: Strouhal number of the maximum spectral Sound energy

Considering the acoustic spectra of the control points drawn in the Figure 70 the noise contribution at different scales in different zones is evident: in the maximum intensity

direction (from 130° to 150°) there is a great contribution of the large scales. In fact the SPL is around 115 - 120 dB at a Strouhal number of 0.01 to 0.1 (see Figure 71) peak at St=0.2 – 0.4 is related to the typical jet instability mode, but the greatest energy is principally at lower Strouhal numbers, the B, C, D, E spectra are similar.

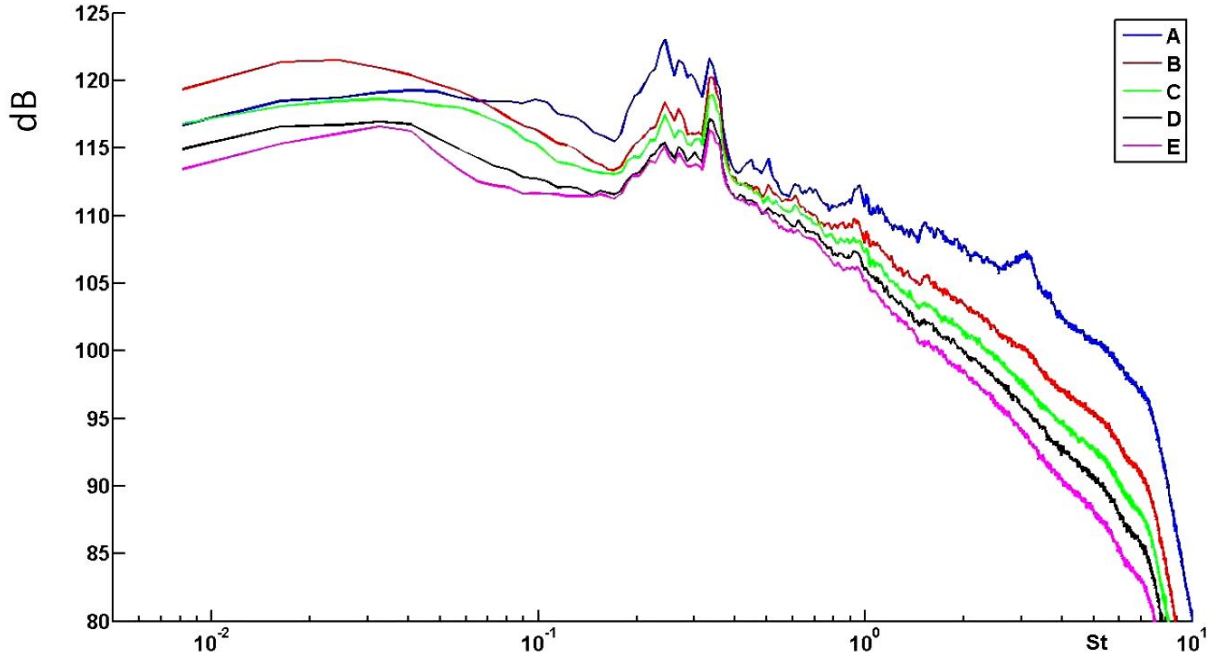

Figure 71: Acoustic Spectra in the maximum directivity control points

In the cone of silence there is a lot of energy at higher Strouhal number. Indeed the SPL is 95 - 100 dB around St=1 (see Figure 72), in this zone the main cause of the noise is probably related to turbulence.

At angles lower than 130°, spectra are dominated by the frequency of the jet instability mode (see Figure 73).

The spectra of the fluid-dynamic part (or pseudo-sound) does not depends strongly on the direction (see Figure 74), but only on the distance from the jet shear layer.

Other near-field spectra are shown in Appendix C.

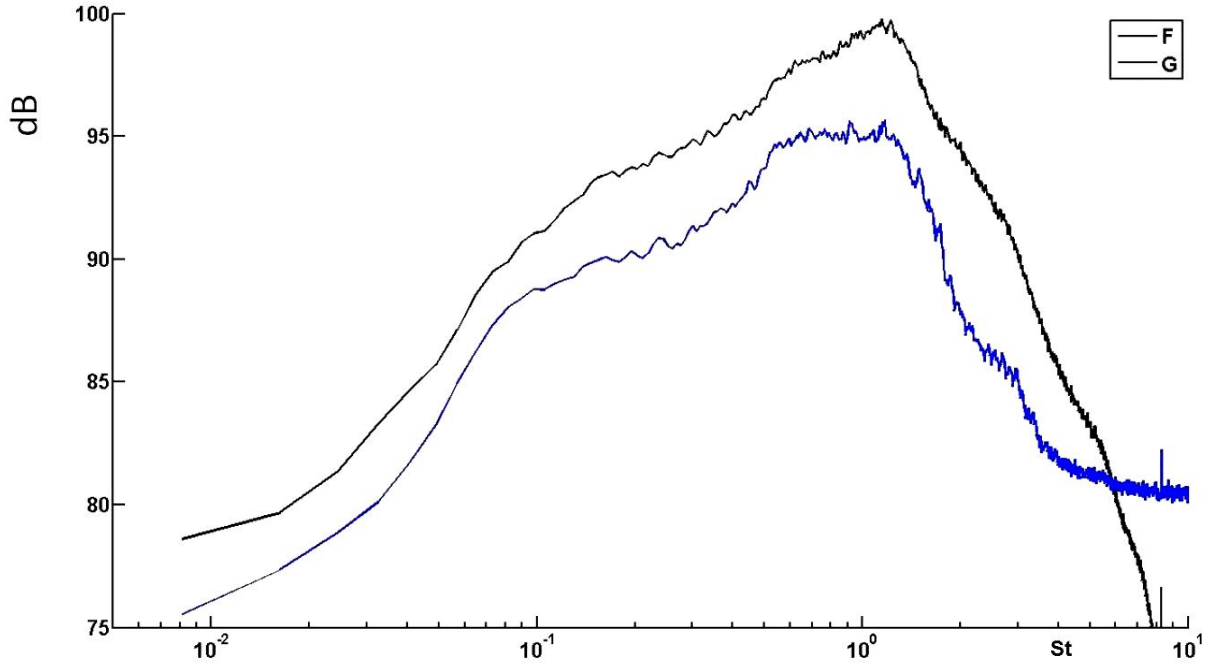

Figure 72: Acoustic spectra in the cone of silence.

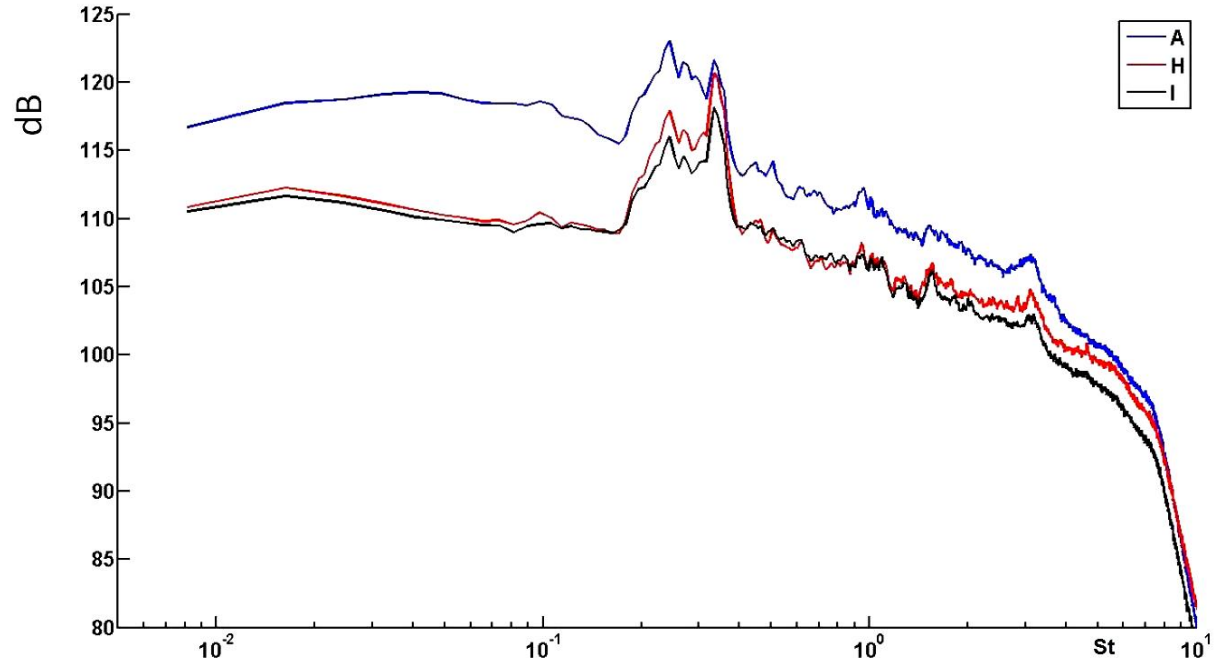

Figure 73: Acoustic Spectra at low angles <130°.

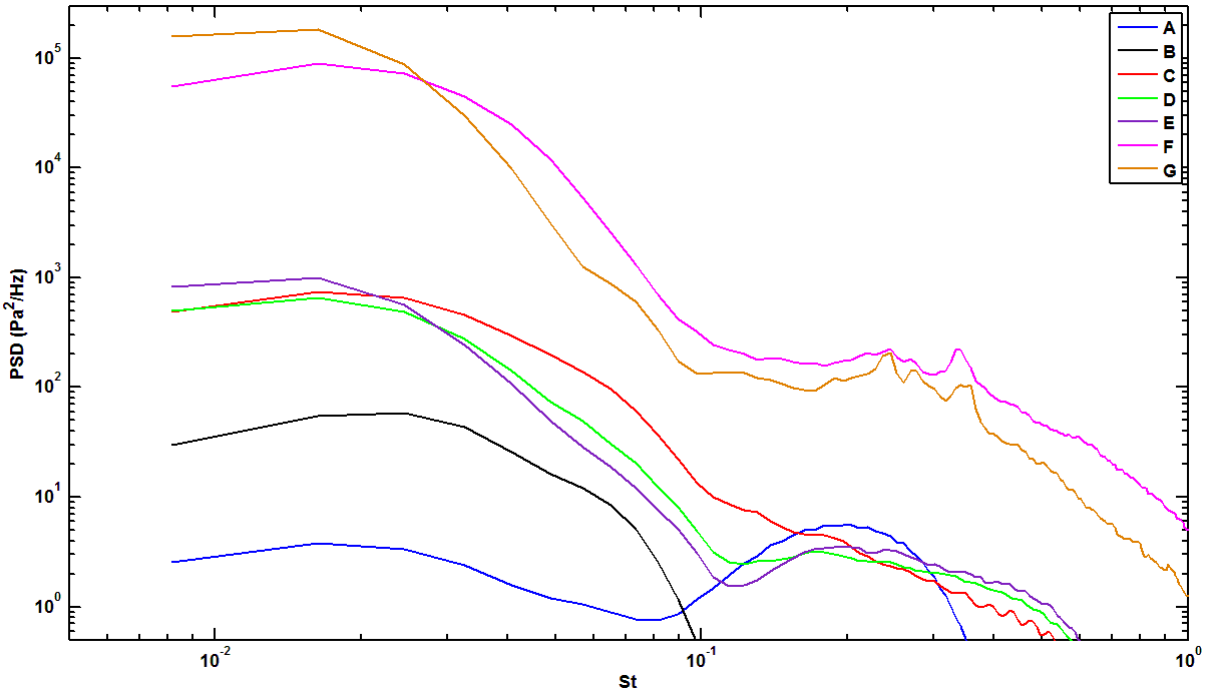

Figure 74: Pseudo-Sound Spectra in the control points

The similitude between the near-field spectra and the far-field spectra is shown in Figure 75. The comparison of two near-field sound spectra at 140 - 150° (B and D points) with the correspondent far-field 150° spectrum, evidences that increasing the distance from the jet the sound pressure level decreases principally below St=0.1 so that the filtered near-field sound spectra became similar to far-field spectra. Figure 75 shows also that the decay law of all the spectra is the same for St> 0.5.

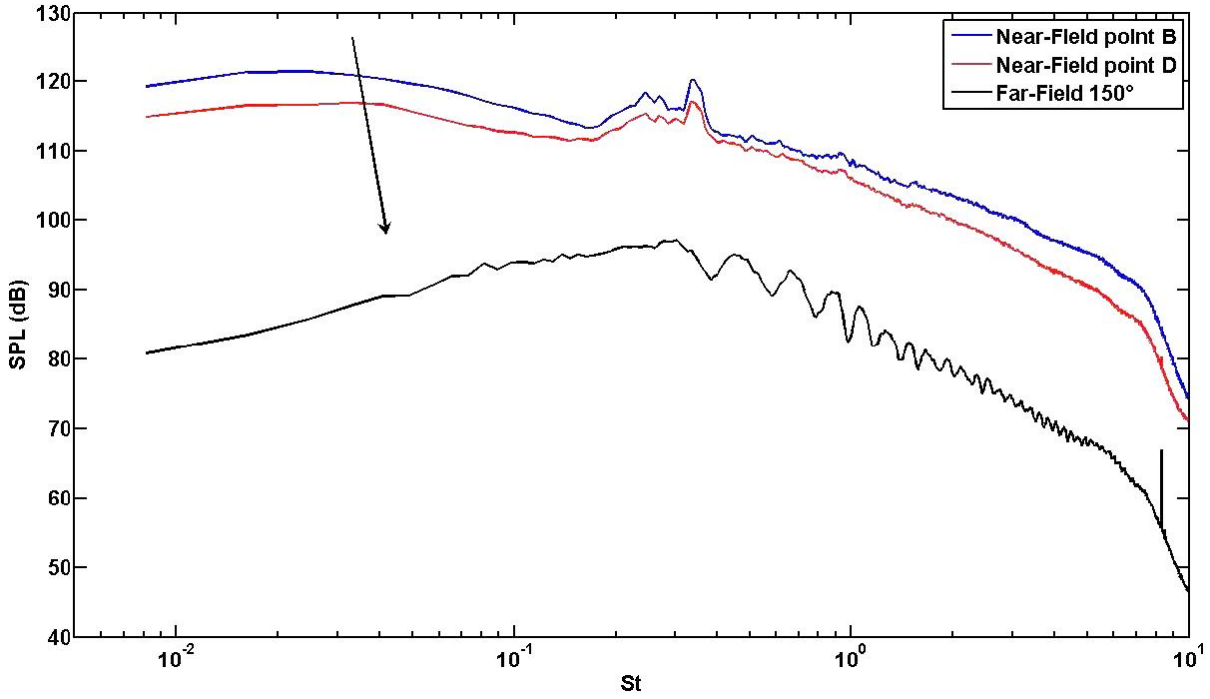

Figure 75: Sound near-field spectra comparison with the far-field 90D spectrum at similar directivity angle

6.3 Mach number effects

Near-field acoustic measurements on the line Y/D=3 are performed to analyze the effects of the Mach number on the near-field spectra (see Figure 60). The Mach number is set at 0.6, 0.7, 0.8 and 1. Figure 76 reports the effects of the Mach number on the unfiltered near-field OASPL, showing that the maximum directivity doesn't change significantly while the OASPL changes. From these measurements it is also possible to evaluate the effect of M on the sound and on the pseudo-sound. The filtering algorithm was applied at some interesting measurement points selected corresponding to 110°, 155° and 165°. Tab 9 shows the coordinates of these points. Figure 77 shows the spectra variation with the Mach number at an angle of 110°. The spectra at Mach 0.5 and 0.6 are similar and after this transition the spectra grow without any significant shape variation.

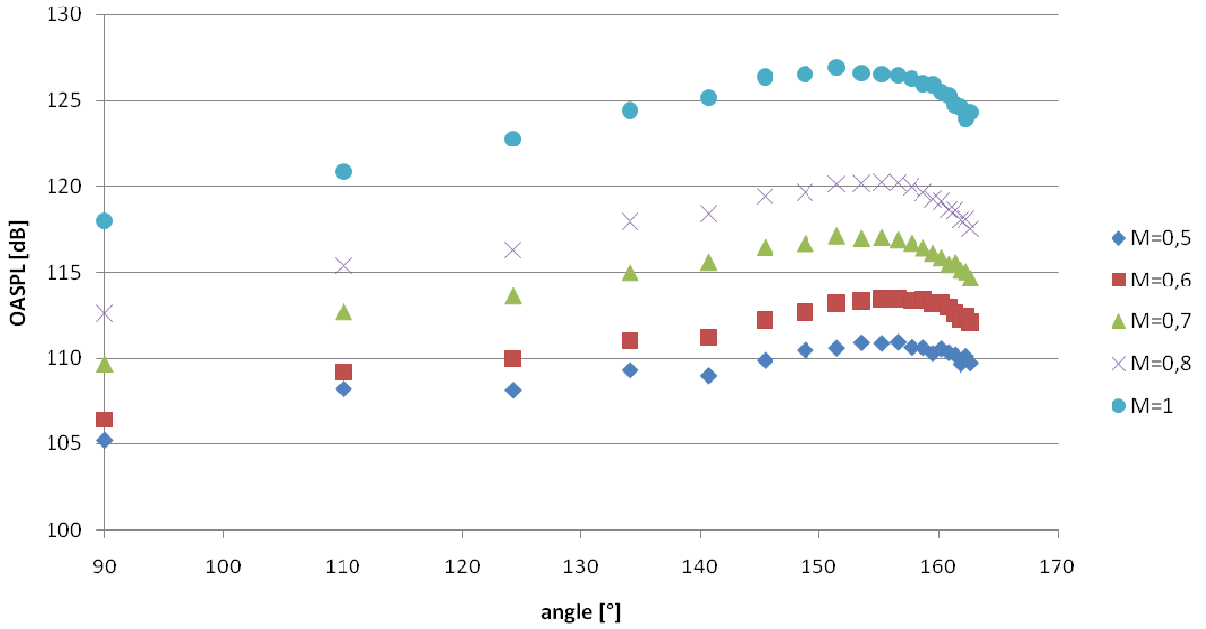

Figure 76: Near-field OASPL variation with the Mach number

X/D	Y/D	Angle
1.2	3.2	110°
10.4	4.8	155°
22	6.7	165°

Tab 9: Coordinates of selected points

Figure 78 shows the spectra variation with the Mach number at an angle of 155°; the full spectra shapes remain quite similar but the amplitude increases especially around St 0.2. In correspondence of lower Strouhal numbers the spectra increase is not relevant. From the previous considerations is evident that the scales around St 0.2 are more sensitive to the Mach variation. Figure 79 shows the spectra variation for the 165° angle, and also for this angle the St near 0.2 are influenced by the Mach variation. Figure 80 shows the effect of the Mach to the sound spectra at 110° obtained by the wavelet filtering procedure. The spectra are quite similar to the original spectra of Figure 77 and they also exhibit the peak around St 0.2 – 0.3.

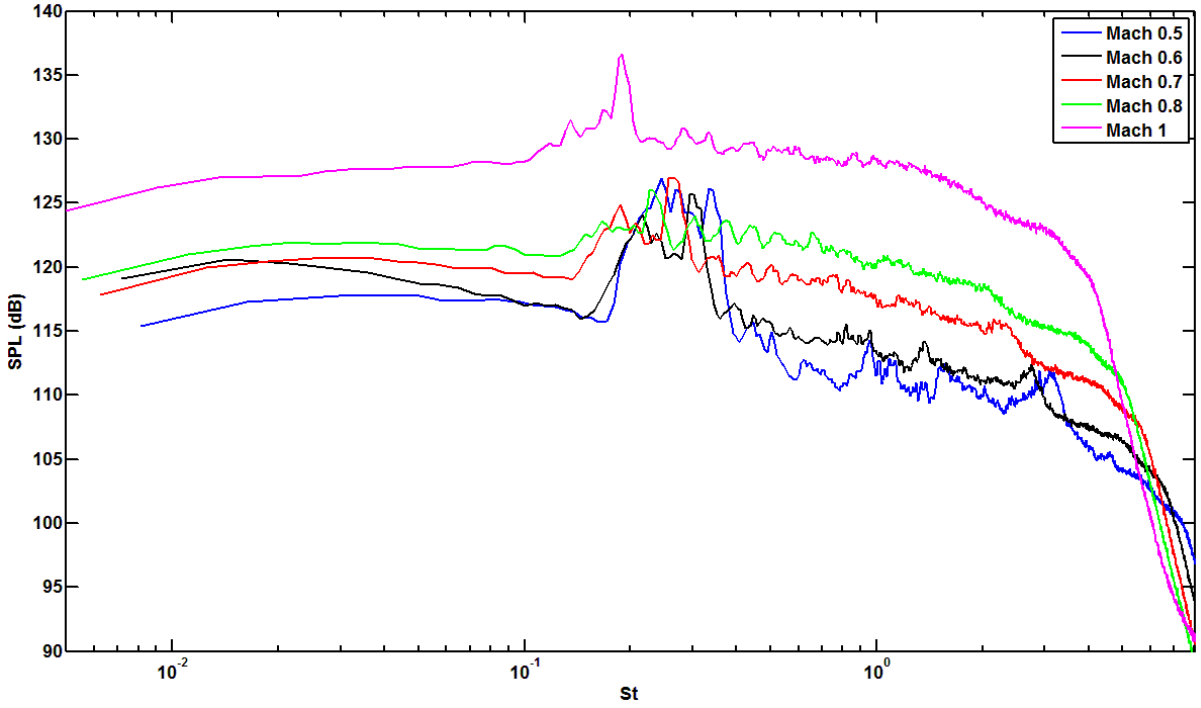

Figure 77: Mach number effect to the near-field spectra at 110°

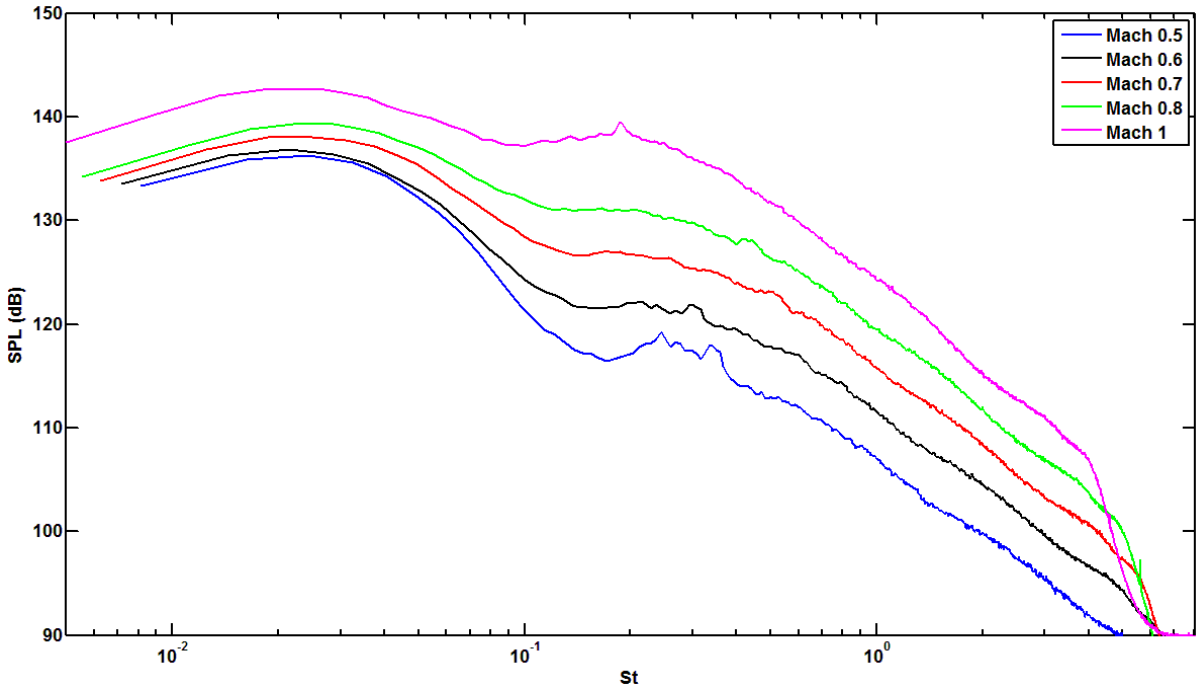

Figure 78: Mach number effect to the near-field spectra at 155°

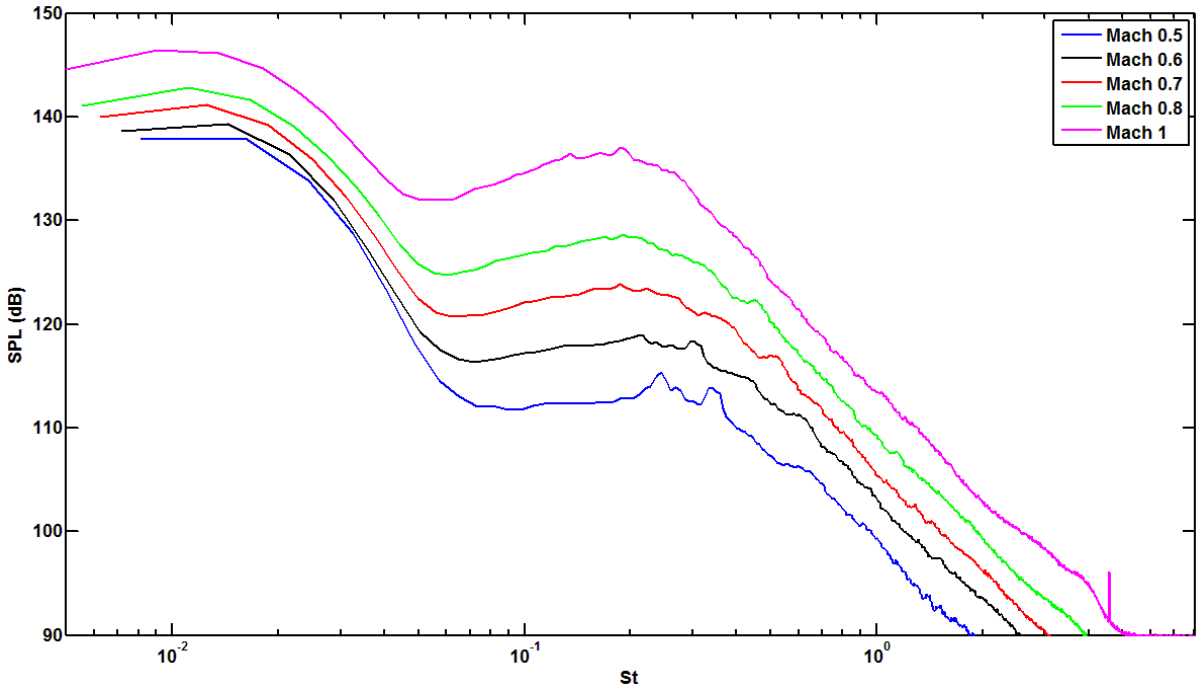

Figure 79: Mach number effect to the near-field spectra at 165°

Analog considerations can be done for Figure 81 and Figure 82. In these figures it is evident the SPL increase at intermediate and low Strouhal numbers with an evident strong increasing between Mach 0.5 and 0.6. So the contribution to the sound increasing is depending by middle and low scales. In fact considering at the same angles the pseudo-sound spectra is evident as the spectra changes a bit with the Mach number; in particular at low angles (see Figure 83) the spectra are similar around St 0.2 and decreases with the Mach number. This decreasing depends by the minor influence of the flow dynamics at low angles, and increasing the jet velocity the induced pressure fluctuations decreases a bit. Figure 84 and Figure 85 show the Mach effects on the pseudo-sound at 155° and 160° angles. Is evident that the shapes of the spectra are similar and the SPL increases only of 5 dB. Thus the Mach effects are evident in particular on the Sound while the pseudo-sound pressure fluctuations change slightly. While the sound increases the pseudo-sound seems unaffected by the Mach and decays very rapidly (Howes 1960) with the distance from the jet axis.

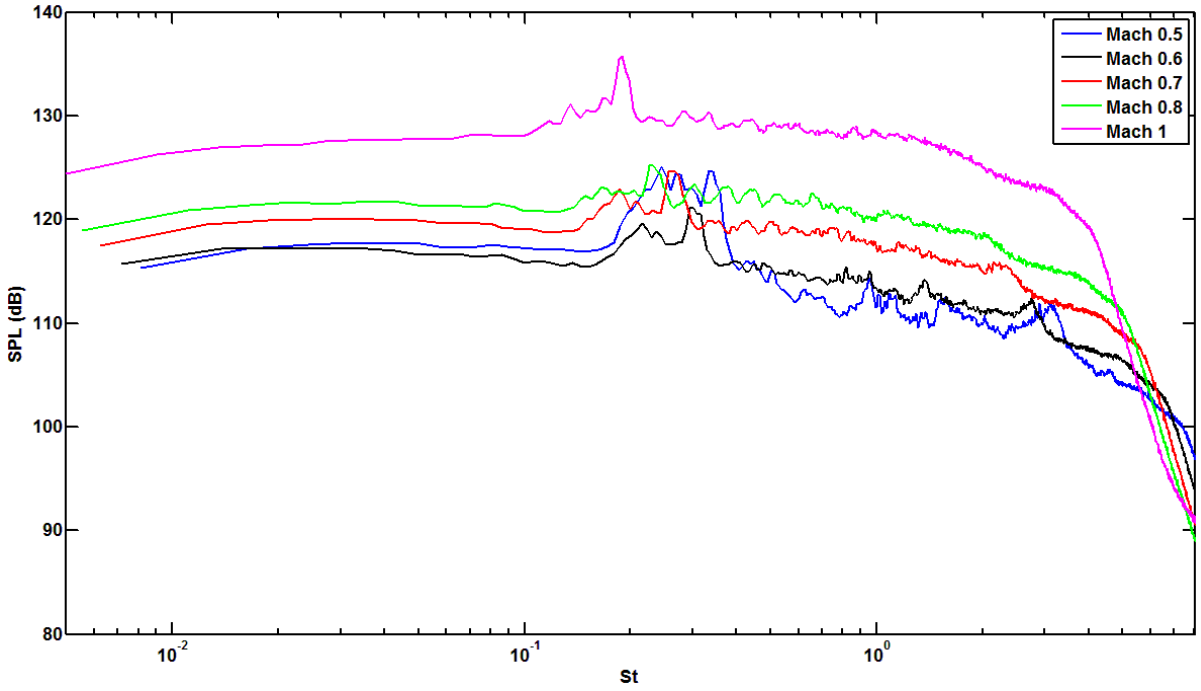

Figure 80: Mach number effect to the near-field SOUND spectra at 110°

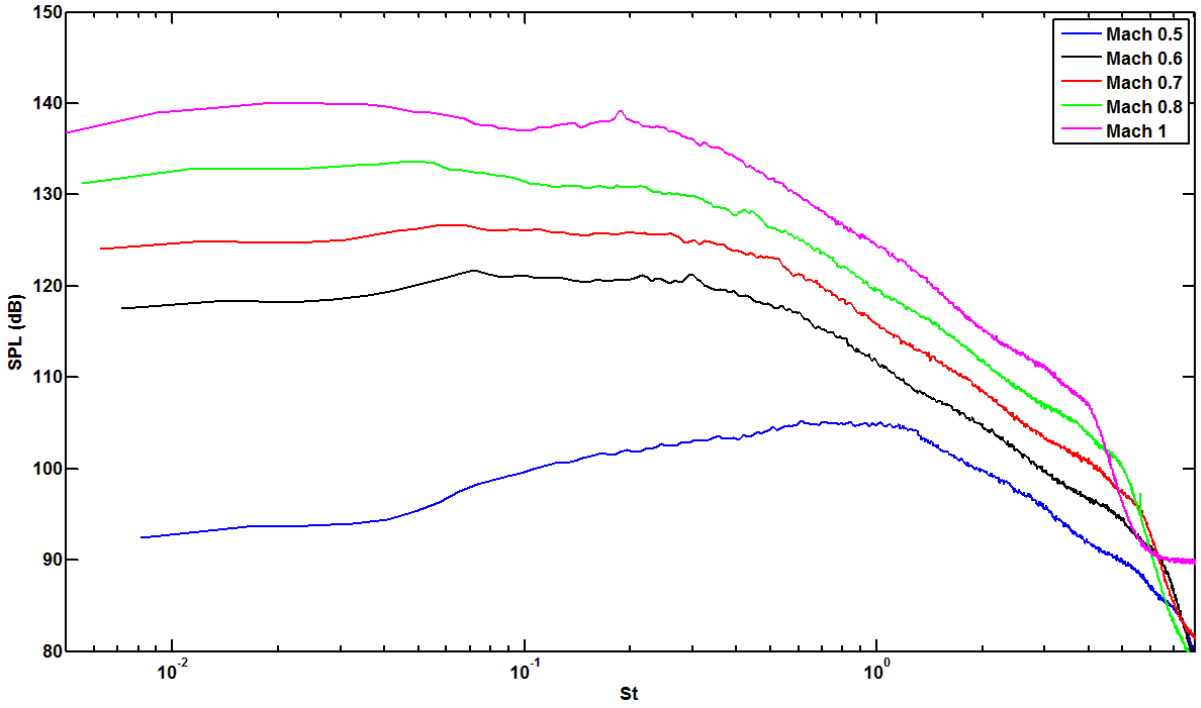

Figure 81: Mach number effect to the near-field SOUND spectra at 155°

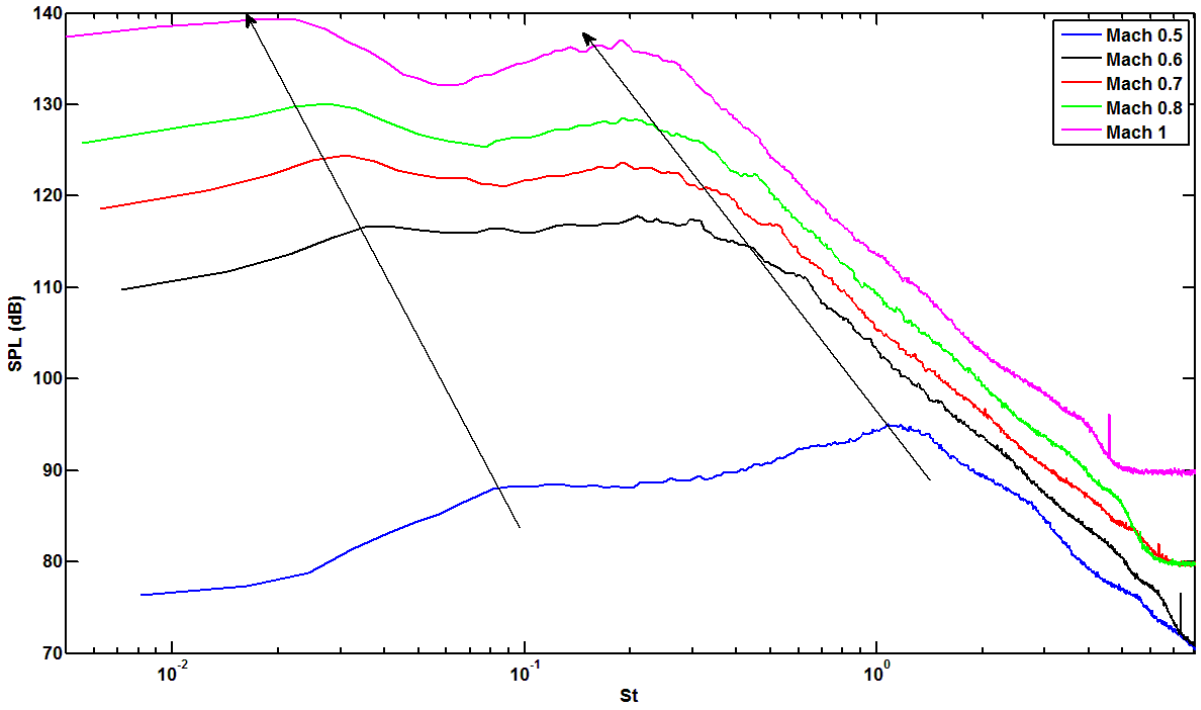

Figure 82: Mach number effect to the near-field SOUND spectra at 165°

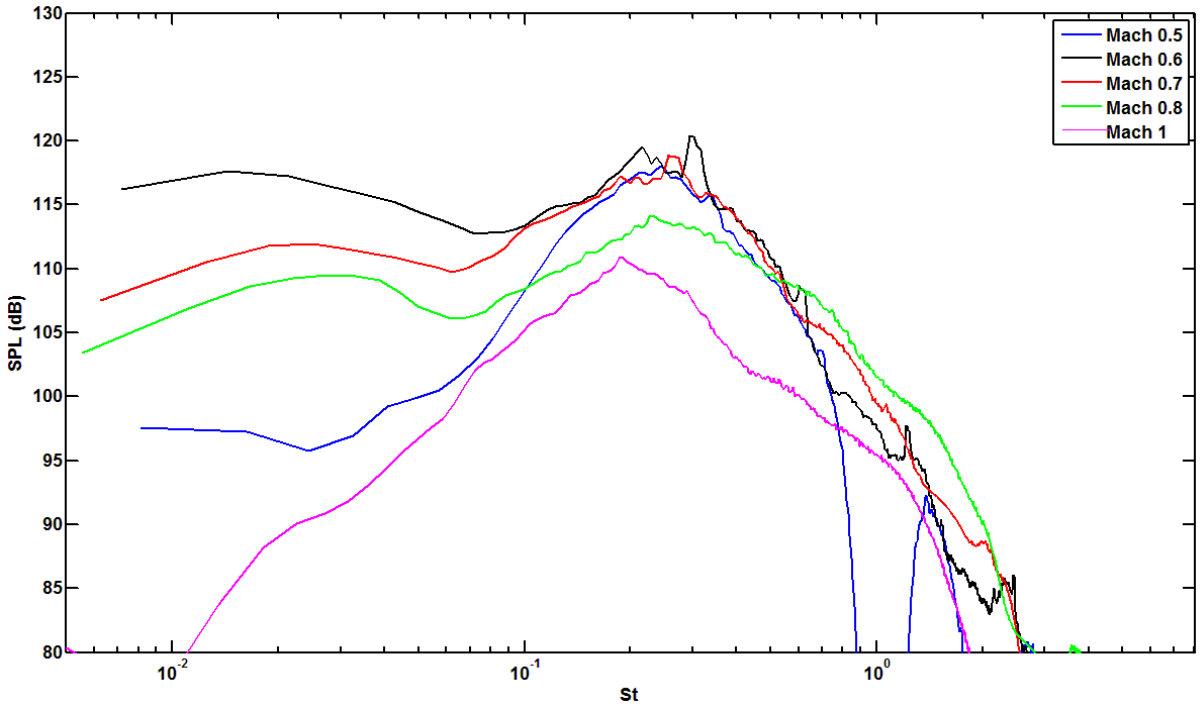

Figure 83: Mach number effect to the near-field Pseudo-Sound spectra at 110°

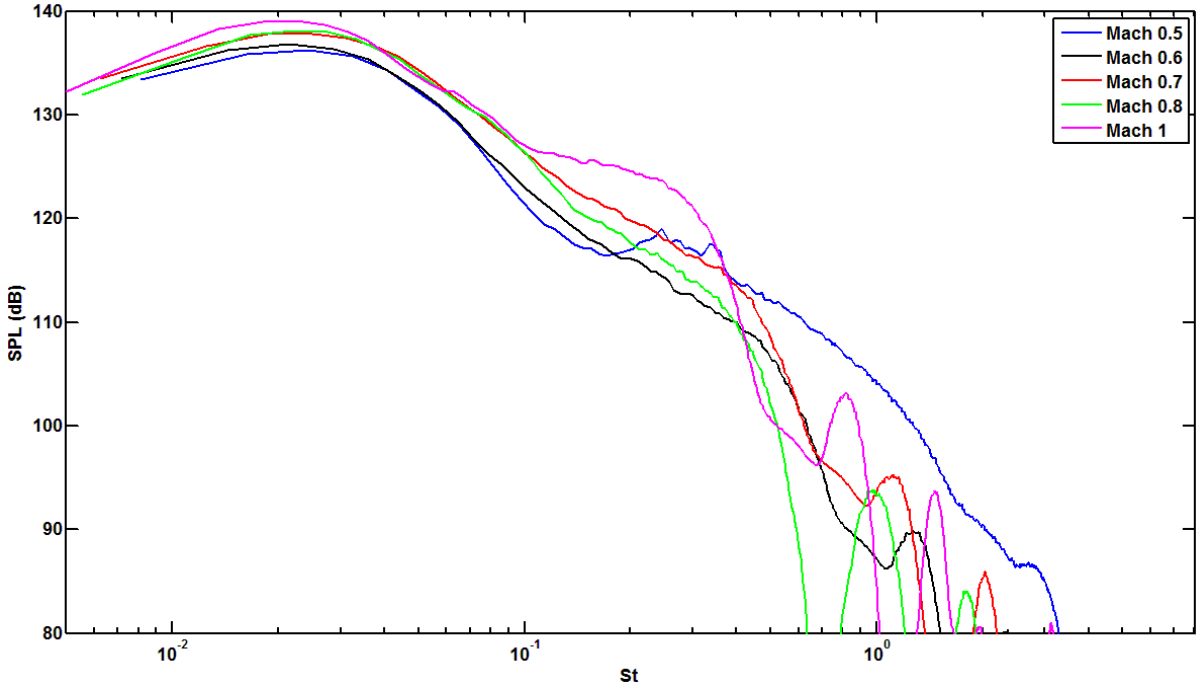

Figure 84: Mach number effect to the near-field Pseudo-Sound spectra at 155°

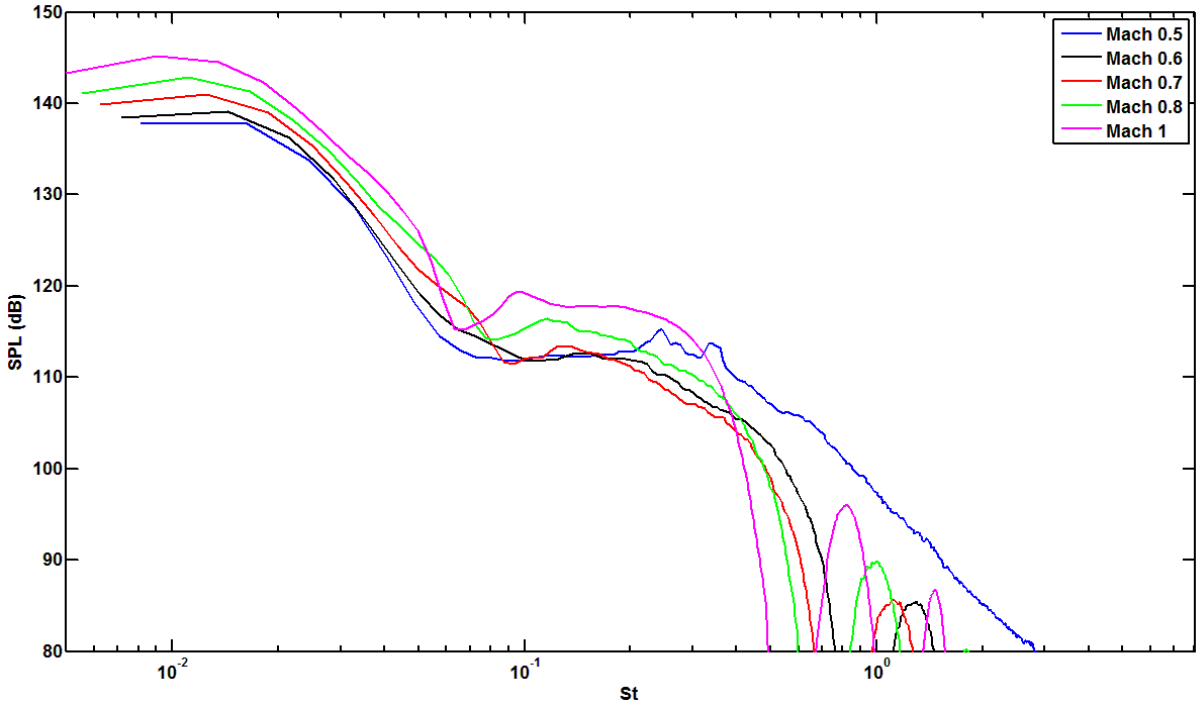

Figure 85: Mach number effect to the near-field Pseudo-Sound spectra at 165°

6.4 Near-field Far-field Correlation

Measurements are performed to verify the correlation of the Sound filtered pressure fluctuations with the far-field. A B&K microphone is mounted in the near-field at X=7D from the nozzle and at a radial distance of 3D from the jet axis. The other microphone is mounted in the far-field at an angle of 150° and a distance of 1.4 m from the first microphone. The jet speed is set to Mach 0.95. The near-field pressure fluctuations are filtered with the wavelet algorithm and the obtained near-field sound and pseudo-sound are correlated with the far-field. Also the propagation velocity is evaluated from the correlation time. Figure 86 shows the filtered spectra compared with the far-field spectrum, and it is evident that at Mach ~1 the sound is much larger than the pseudo-sound; the green lines indicate that the high frequency ranges are very similar. The cross correlation of the far-field pressure fluctuations with the near field filtered and unfiltered parts is shown in Figure 87. The pseudo-sound doesn't correlate with the far-field and the sound has a correlation peak corresponding to a velocity of 348 m/s.

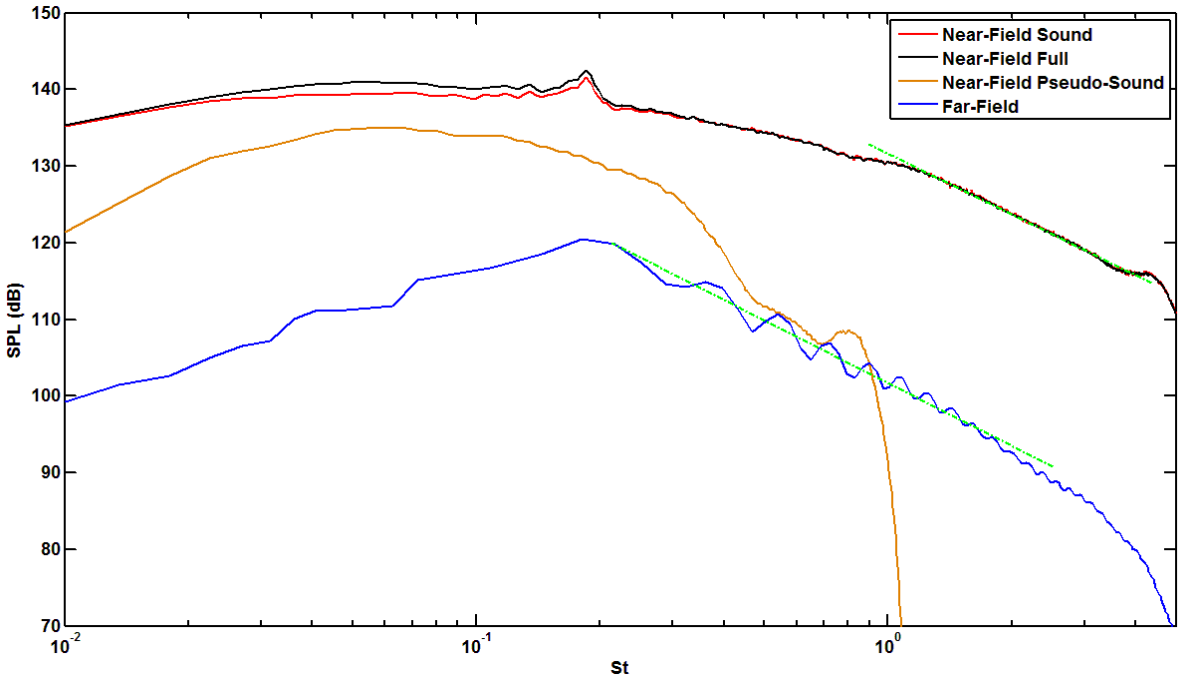

Figure 86: Near-field filtered and Far-field spectra

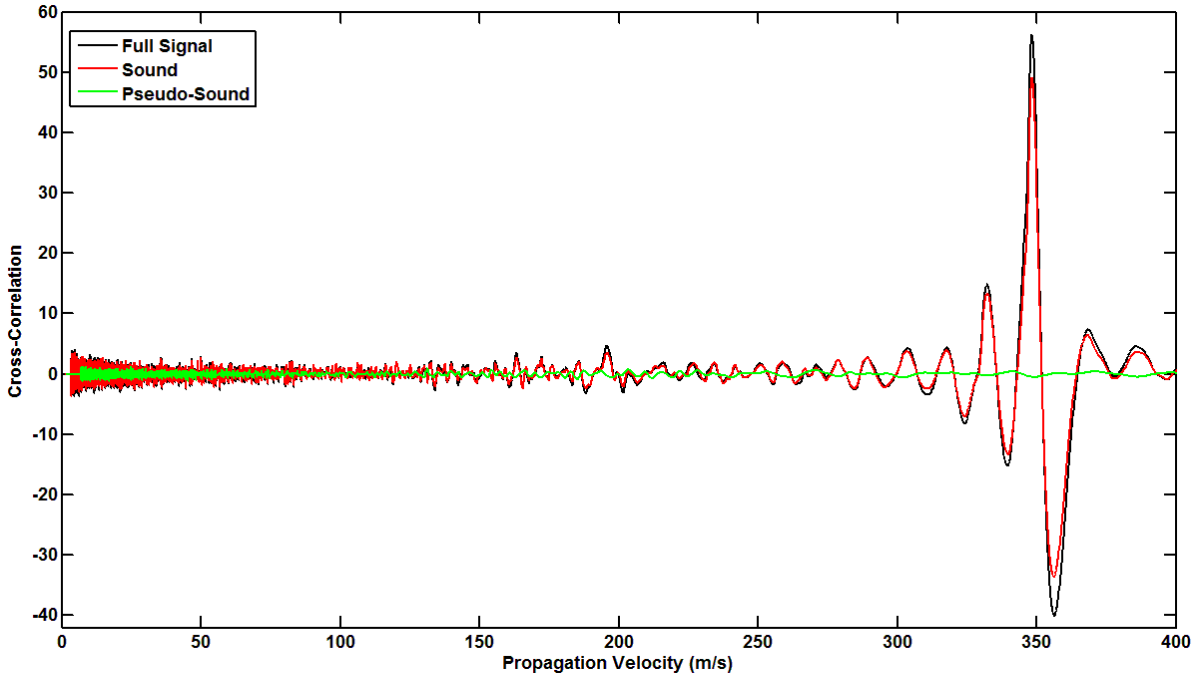

Figure 87: Near-Field pressure fluctuations cross correlation with the Far-Field

7 Identification of Noise Sources

Hot-wire and acoustic simultaneous measurements are performed with the aim of correlating velocity with sound and pseudo-sound pressure fluctuations and to identify their sources in the jet flow.

The B&K microphones are positioned in a transition zone where the energies of the sound and of the pseudo sound are similar, at 7D on the jet axis with a radial distance of about 4D. The jet plane is mapped with a hot-wire probe, on the grid reported in Figure 42, simultaneously with the pressure measurements.

7.1 Hot-wire interferences

In order to quantify the hot-wire interference with the pressure fluctuations also measurements with the microphones with and without the H-W probe were performed. The hot-wire was moved along the jet axis and along the nozzle border line at Mach 0.5 and 0.7. Figure 89 shows the effects of the hot-wire along the centre line. The how-wire influence is not strong and is evident in particular at the highest frequencies and only when the probe is close to the microphones. Figure 90 shows the effects when the hot-wire is moved along the border line. In Appendix D the effects at Mach 0.7 are shown with analogue results. In any case, the influence of the hot-wire on the measured pressure fluctuations can be safely neglected.

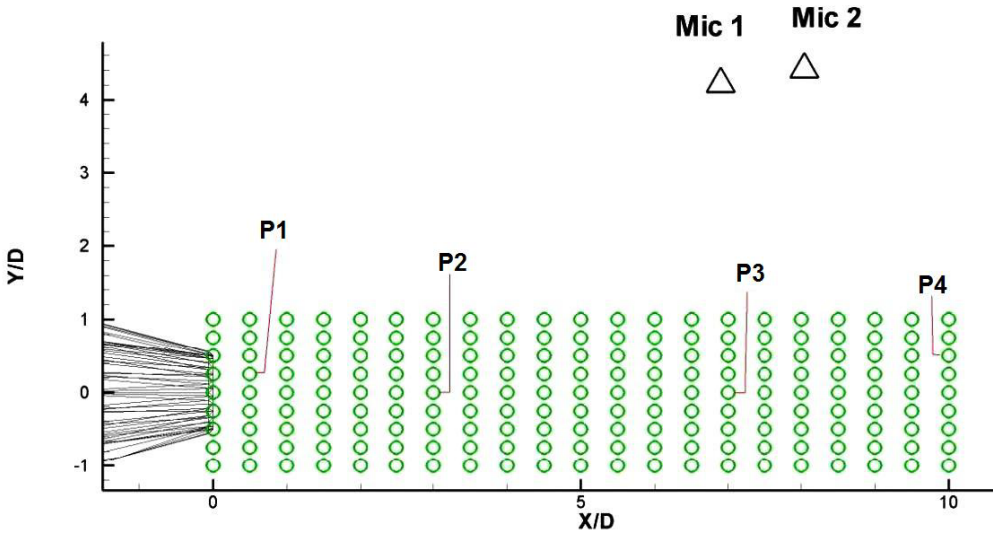

Figure 88: Hot-wire measurement grid and microphones positions.

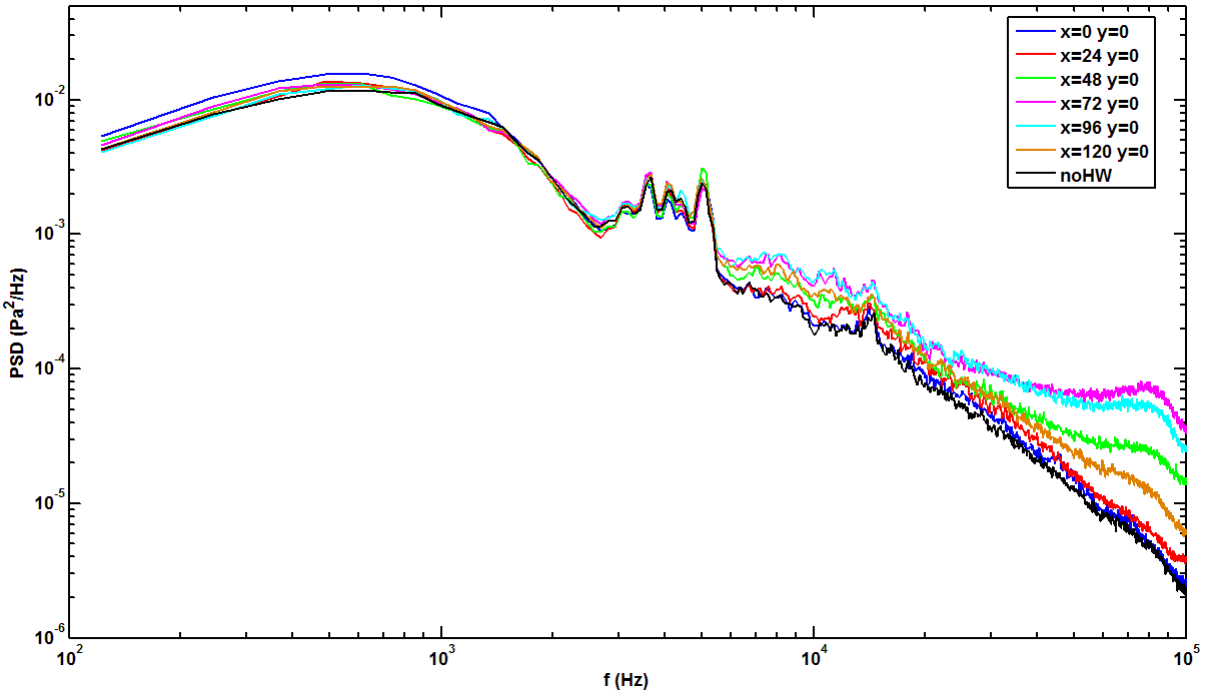

Figure 89: Hot-wire effects at Mach 0.5 along the centre line

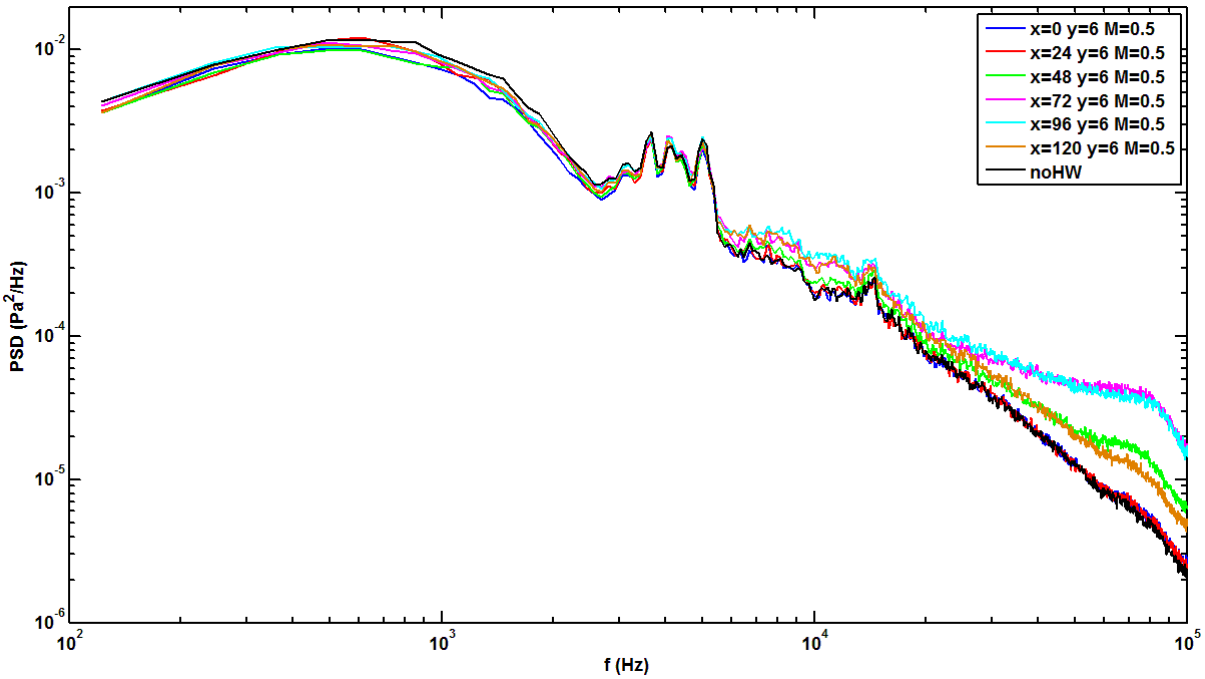

Figure 90: Hot-wire effects at Mach 0.5 along the border line

Some particular positions of the hot-wire probe are marked in Figure 42. The pressure fluctuations, measured at Mach 0.5 with the h-w in the selected positions (P1, P2, P3 and P4), are filtered with the wavelet algorithm and the sound spectra are compared to evaluate hot-wire acoustic interferences. Figure 91 shows a comparison of sound spectra with and without hot-wire. As previously described the interference is more evident at high frequencies; the hot-wire interference is negligible for St < 4 because the SPL variation less than 2%. Figure 92 shows also the spectral effects on the pseudo-sound that are acceptable.

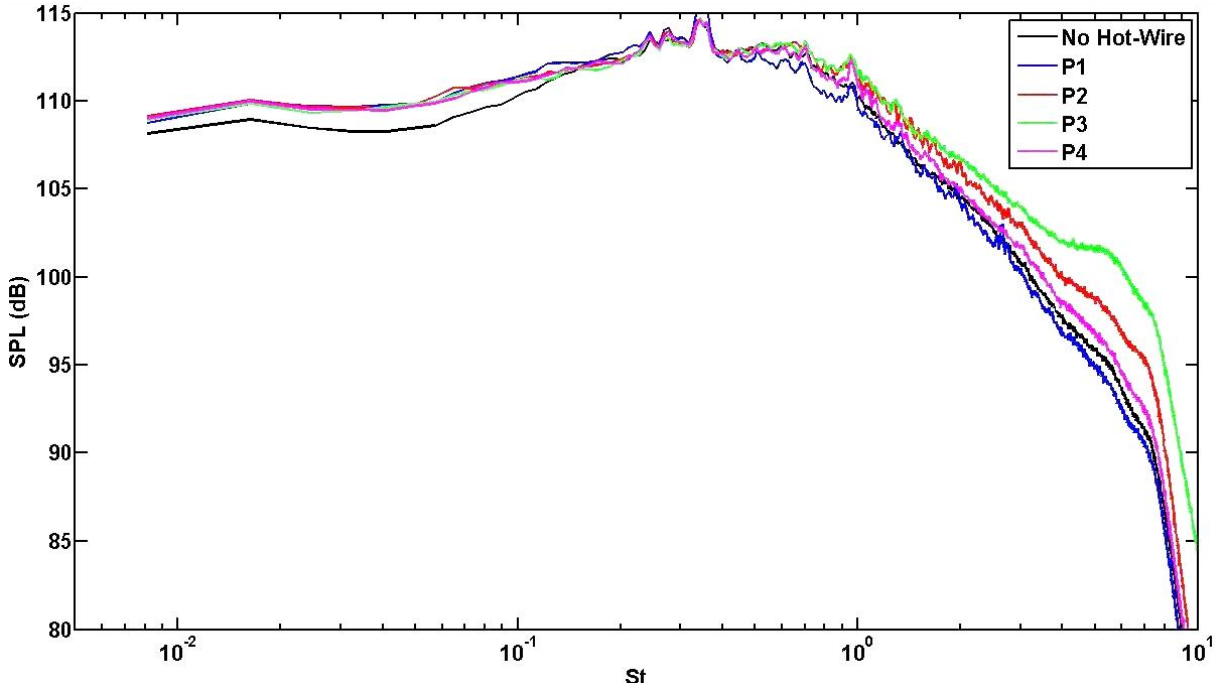

Figure 91: Hot-wire effects at Mach 0.5 on the Sound spectra

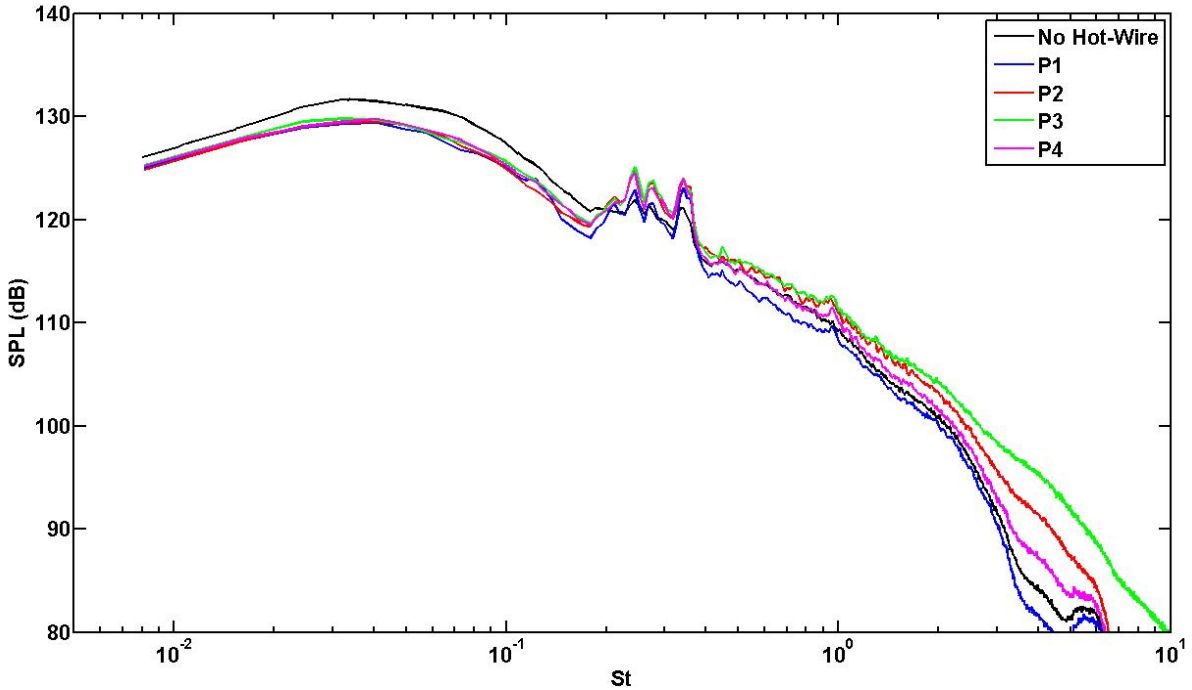

Figure 92: Hot-wire effects at Mach 0.5 on the Pseudo-Sound

7.2 Velocity-Pressure Correlations

Pressure fluctuations and velocity are measured simultaneously on the points of Figure 88 to identify the contribution of the jet zones to the sound emission. Two microphones are used to apply the described wavelet algorithm. The data from the microphones are filtered with the wavelet technique and the sound and pseudo-sound signals are correlated with the anemometric data obtained using the hot-wire. From the correlation peak distribution it is possible to locate the zones of sound emission and the zones that generate the pseudo-sound pressure fluctuations.

As shown in Figure 93, the maximum sound-velocity correlation values are in the potential core, the maximum being at the end of the core that is a zone of strong fluctuations. This confirms the observations of Guj et Al.(2003), Hileman et Al. (2005), Kerhervé et Al. (2008) and of Grassucci et Al. (2010) that locate the maximum noise emission at the potential core end. Regarding the effects of hot-wire on the sound in particular for the more critical P3 position, is evident that it doesn't influence the correlation because there isn't any strong spot of correlation in the correspondence of this point. The maximum sound emission seems to be on the axis around the X=3D position and all the potential core contributes to the sound generation.

Figure 94 shows the cross-correlation of the velocity with the pseudo-sound. This cross-correlation field confirms that all the jet flow contributes with similar levels to the generation of the pressure fluctuations. The values are lower those found for the sound and the differences between the measurement points are weak. In detail there are two zones of higher correlation values: the first is in correspondence of the interaction of the jet with the external flow; the second zone is around 7D (6D < X < 8D).

The zones at the end of the potential core and around X/D =7 have been observed also in the works of Kerhervé et Al. (2008) and of Grassucci et Al. (2010).

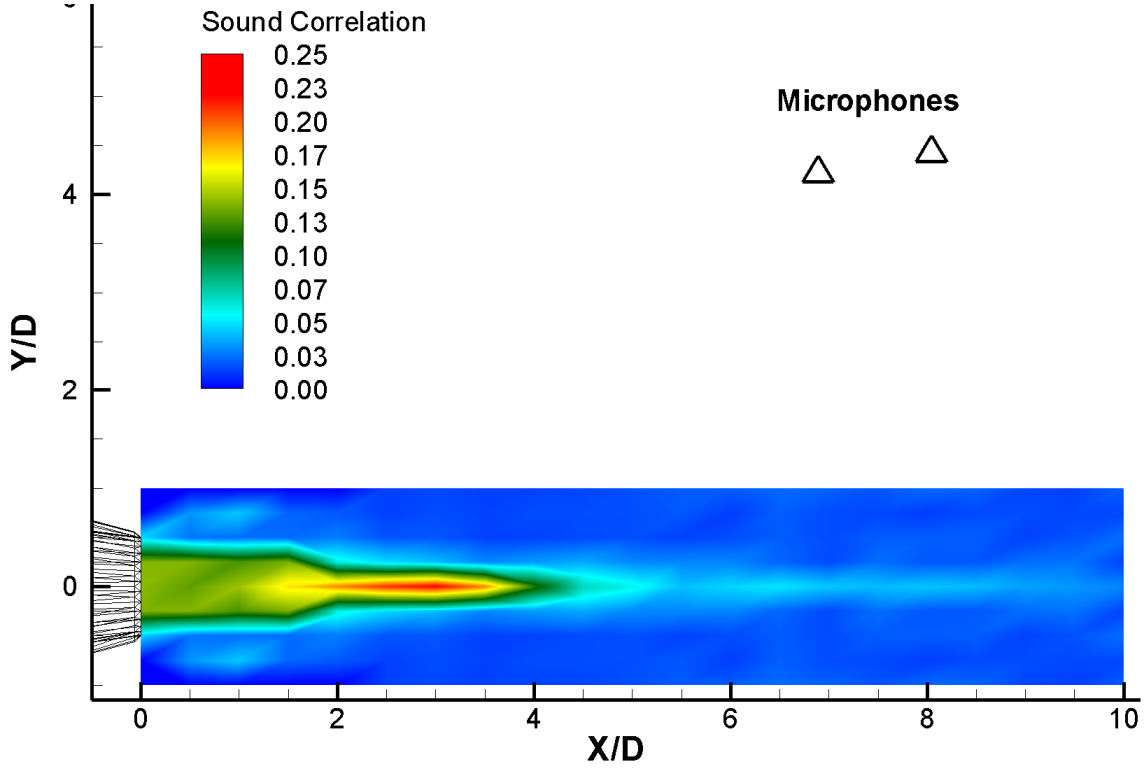

Figure 93: Velocity Sound cross-correlation

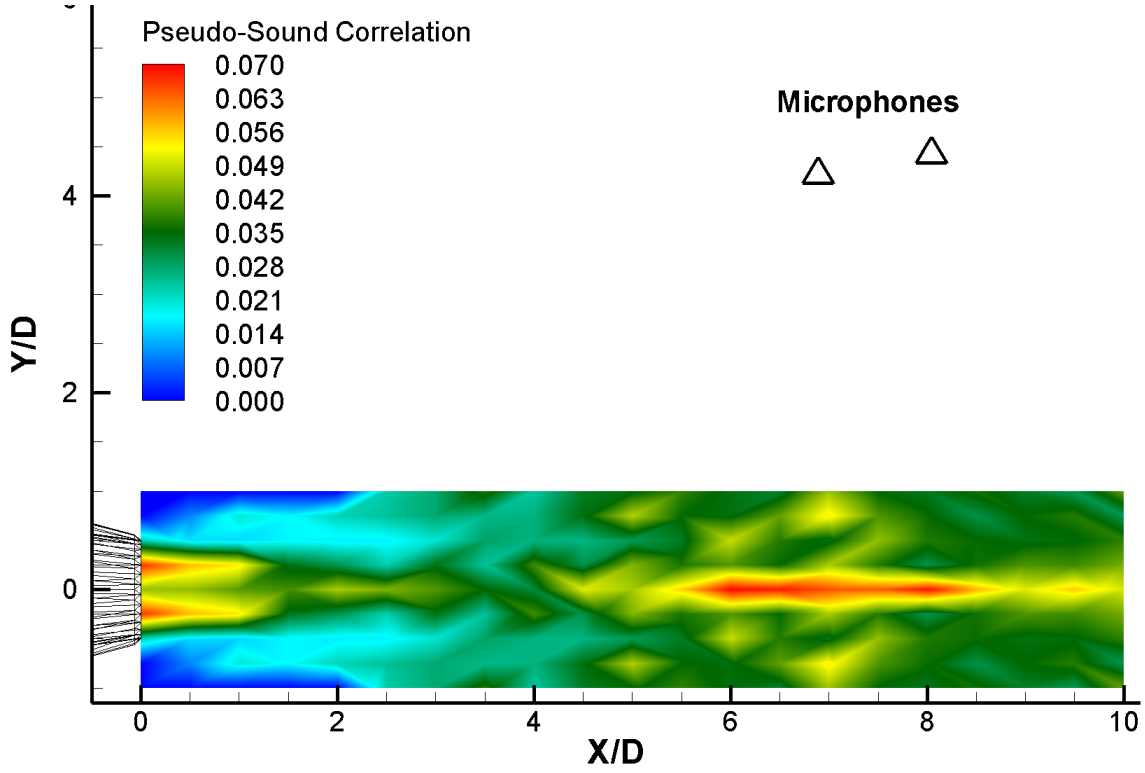

Figure 94: Velocity Pseudo-Sound cross-correlation

The previous mentioned zones need to be further investigated to better understand their contribution to the generation of the pressure fluctuations. Figure 95 shows the velocity auto-correlation function along the jet axis. In the figure is evident how the zone at the end of the potential core (2D - 4D) generates periodic velocity fluctuations. The zone around the nozzle exit instead generates velocity fluctuations with different frequencies.

Figure 96 shows three auto-correlation profiles extracted at 1, 2 and 3 diameters. The profiles at 2 and 3 diameters shows a fluctuation with a period of about $2*10^{-4}$ seconds that corresponds to a Strouhal number of 0.3 corresponding to the characteristic peaks of the jet (e.g. see Figure 64).

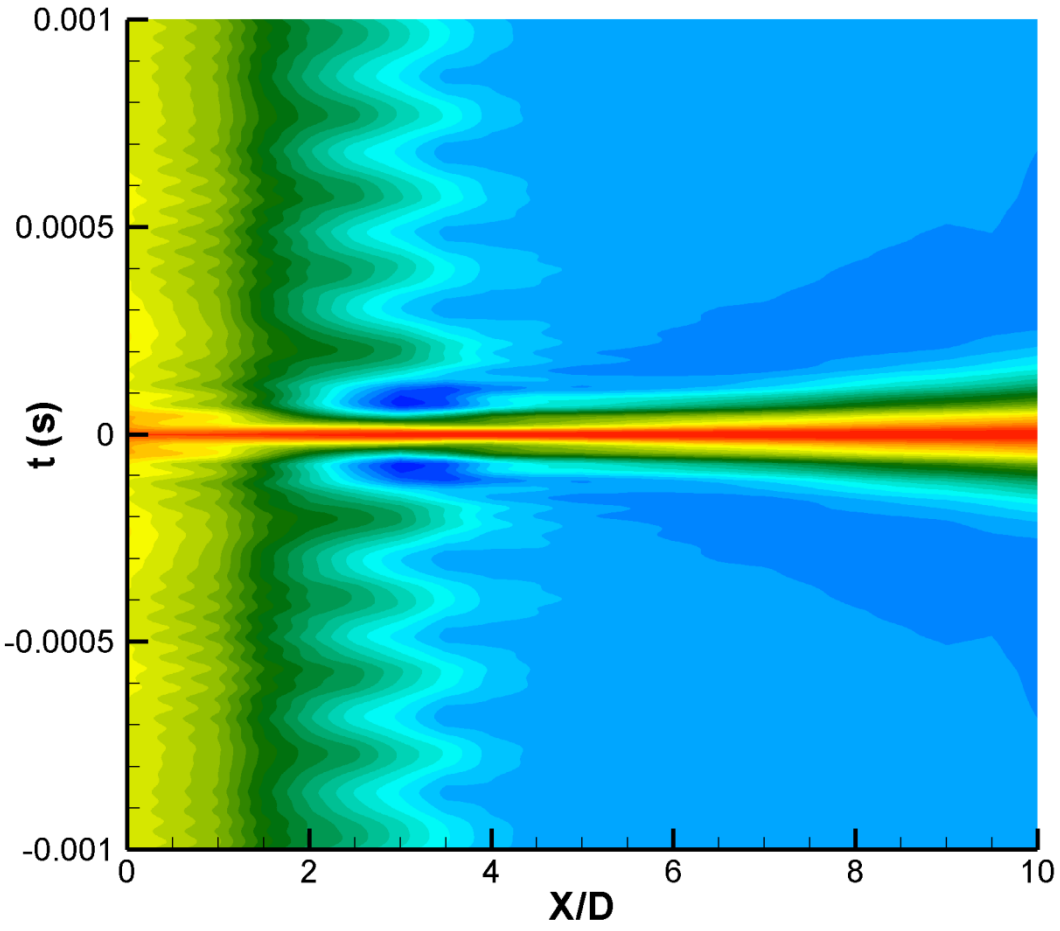

Figure 95: Velocity auto-correlation along the jet centre line

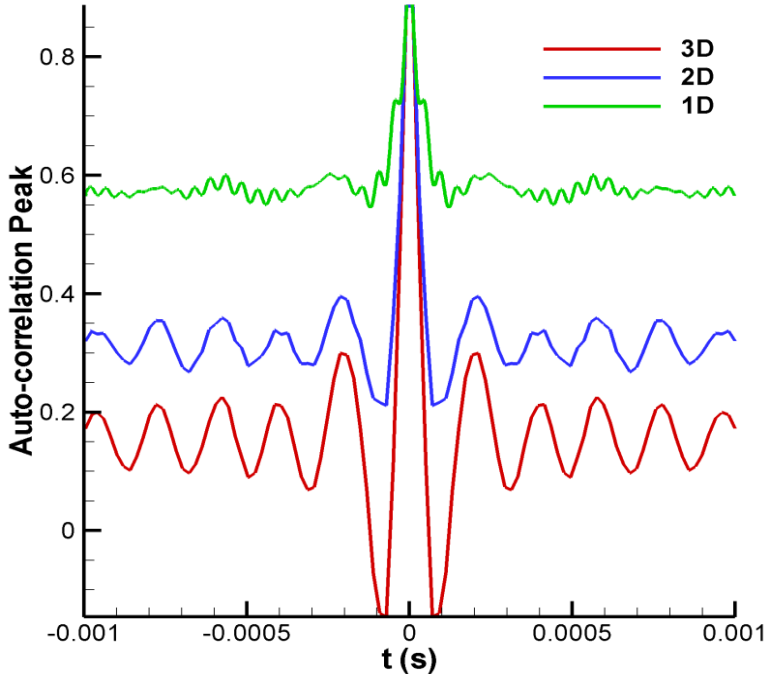

Figure 96: Velocity auto-correlation profiles

The cross-correlation of the velocity with the sound helps to identify the sound emission zones. Figure 97 shows the time-space cross-correlation along the axis of the jet. The cross correlation shows that around 3D the velocity fluctuations give high correlation with the sound. Note that the distance between the two maximum peaks corresponds to a time of $2*10^{-4}$ seconds (Strouhal 0.3). The fluctuations generated in this zone with a St=0.3 propagate as sound in the field. The slope of the correlation lines is proportional to about 170 m/s, corresponding to the flow velocity at Mach=0.5. The time value of the higher correlation peak, for each position X/D, is the propagation time of the fluctuations to propagate from the hot-wire to the microphone and is inversely proportional to the sound speed. For example the maximum peak time at X/D=0 is t=0.00028 s, the distance between this position and the microphone is 0.097 m, the evaluated propagation velocity is 346 m/s. This sound emission zone (2D to 4D) was found also in the work of Tam et Al. (2008) as a maximum noise level measured with an acoustic mirror for angles of 130 to 150°. Figure 98 shows the cross-correlation of the velocity with the pseudo-sound along the jet centre line. The higher pseudo-sound pressure fluctuations are generated in the zone between 6 and 8 diameters. Another slight fluctuation emission zone is present closest to the nozzle.

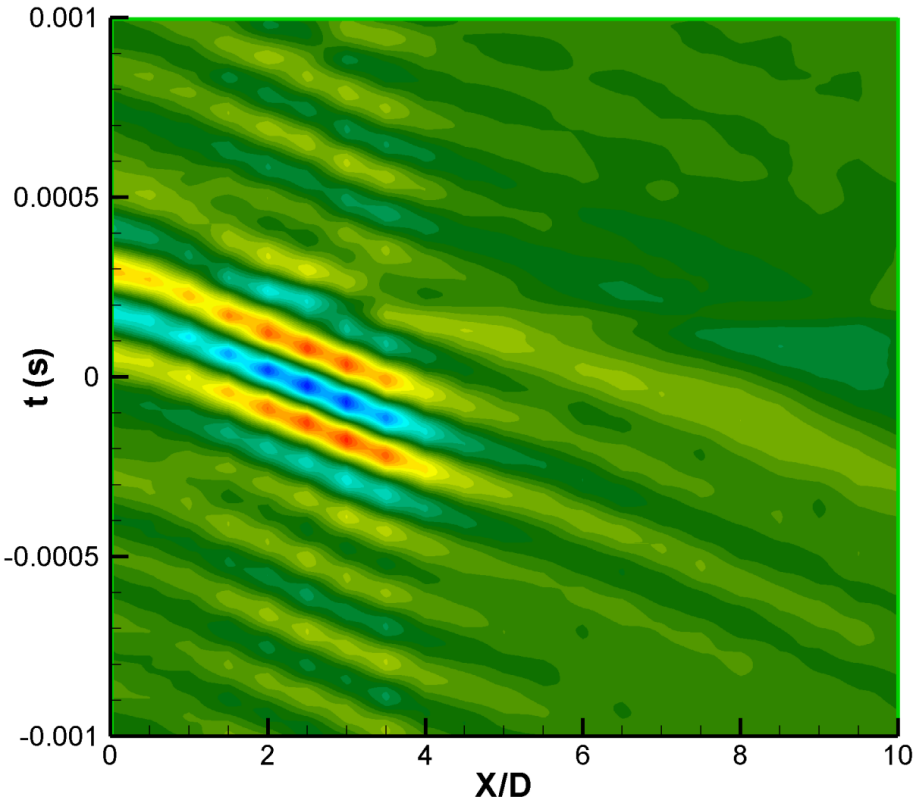

Figure 97: Velocity Sound cross-correlation along the jet centre line

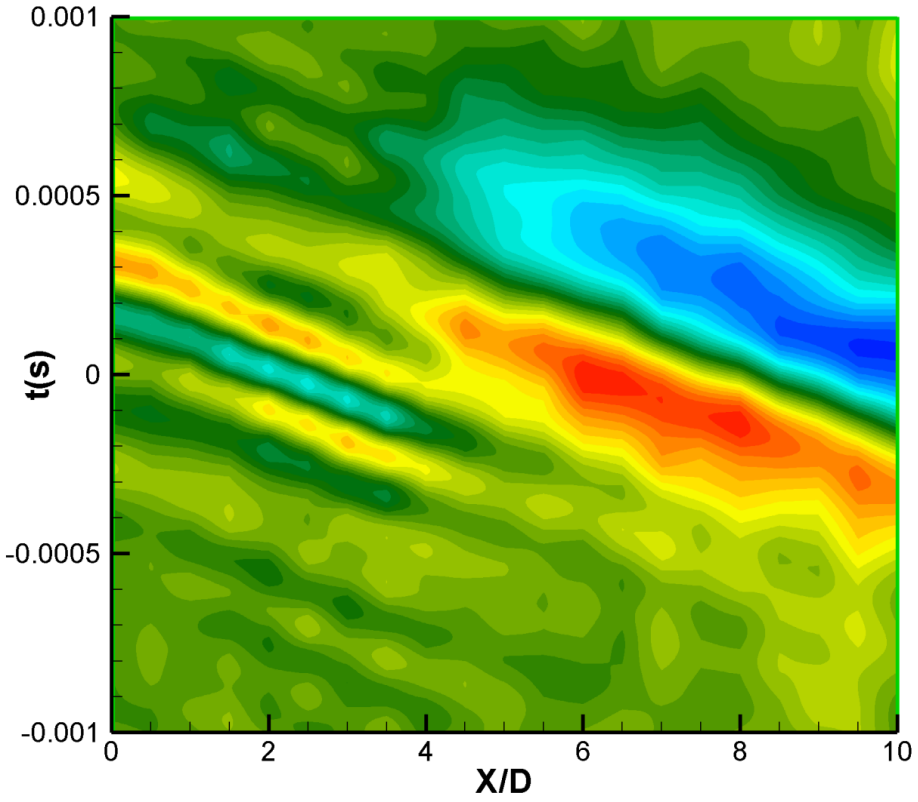

Figure 98: Velocity Pseudo-Sound cross-correlation along the jet centre line

7.3 Potential Core Fluctuations

As shown previously, the maximum noise emission zone for the 150° directivity is located at the end of the potential core. This sound emission can be attributed to the intermittent collapse of the core (Hileman 2005). The intrusion of structures into the potential core described by Jordan (2008) can generate these contractions. By definition, the potential core is *a zone where the jet velocity maintains undisturbed* (Rajaratnam 1976). Starting from this definition it is possible to create an algorithm that evaluates the collapses of the core. Since the jet core flow isn't turbulent, it is reasonable to evaluate the core collapses using a threshold of 98% with respect to the jet undisturbed velocity. When the velocity falls below the threshold the algorithm assigns a value of 1 to a discrete contraction function; this means that the velocity in that point is disturbed. When the velocity is greater than the threshold the function assumes a 0 value. This algorithm creates only an oscillating time history that describes the dynamics of the core. Figure 99 shows the time history of the collapses computed at X/D=3; Figure 100 shows a detail of this core contractions evidencing that the contraction events interest a wide band of frequency scales.

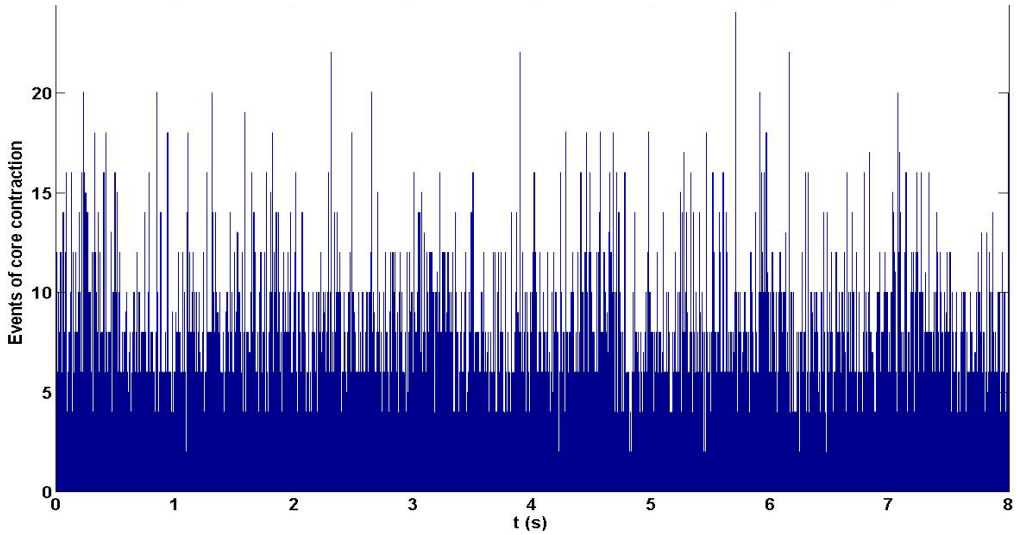

Figure 99: Time history of the potential core contractions

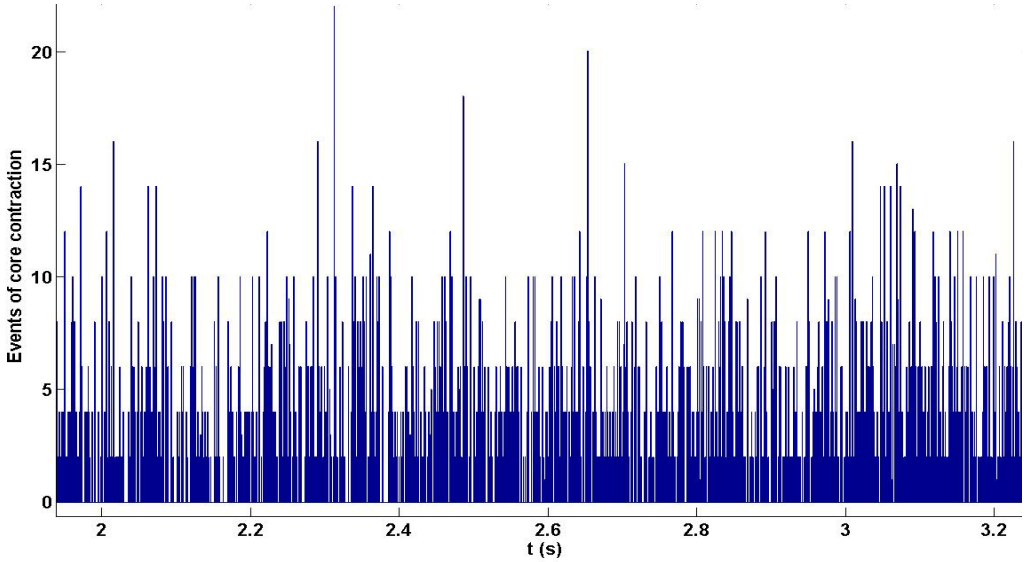

Figure 100: Detail of the core contractions.

Figure 101 shows the spectrum of the discrete contraction function obtained from the algorithm. This function is composed exclusively of 0 and 1 and its spectrum is vertically shifted to compare its shape with the sound and the pseudo-sound spectra in the near-field (X/D=7, Y/D=4). The figure shows a strong similitude of the contraction core spectrum with the sound spectrum and reveals the presence of the peak at St=0.3 also in the contraction spectrum. Figure 98 shows that pseudo-sound fluctuations are partially generated also in the potential core. The low frequency of these fluctuations can affect the spectra of the core contraction causing the discrepancy of the two spectra in Figure 101 for f <1 kHz. From these considerations it is reasonable to assume that the potential core contractions are the main noise production phenomenon on a wide range of frequencies.

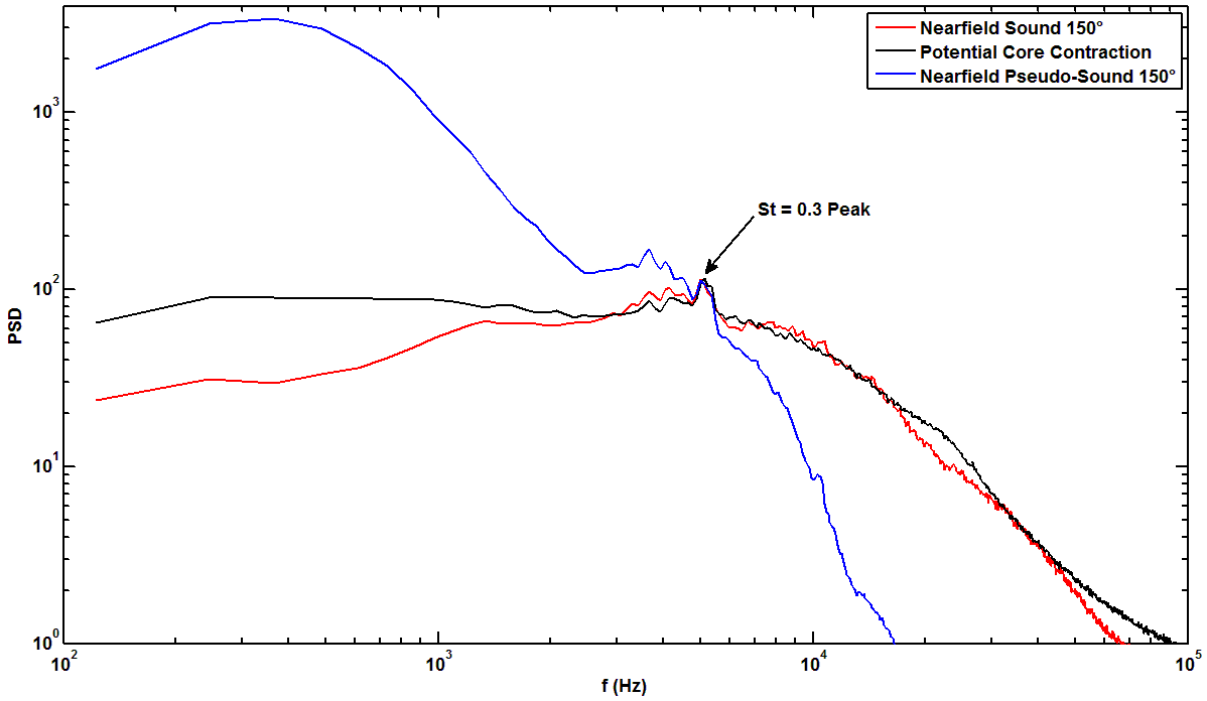

Figure 101: M=0.5; Potential Core contraction spectrum (X/D=3) compared with sound and pseudo-sound spectra at 150°

8 Conclusions

In this work far-field and near-field acoustic measurements were performed on a compressible round jet. The jet velocity and far-field pressure measurements correspond to the standards found in literature.

A wavelet filtering method was implemented for separating sound and pseudo-sound. The wavelets are able to separate intermittent events from the Gaussian background because they are located both in time and in frequency domain. This novel approach, applied to the near-field pressure, reveals to be able to extract common characteristics between near-field and far-field noise.

The directivity of the noise, the shape of the spectra and the presence of the cone of silence are in agreement with the theories and other tests performed on compressible jets. This work extracts also, from the pressure fluctuations, information on the convection velocity of pseudo-sound component in agreement with theories.

The shape of the pseudo-sound spectra doesn't depend by the position of the measurement point in the near-field and only the energy level depends by the distance from the jet. On the contrary the near-field sound spectra show shapes and energy distributions that depend on the angular position with respect to the jet. This confirms that the directivity depends on the frequency since different wavelengths propagate acoustic energy on preferential directions. The Mach number affects more the sound spectra than the pseudo-sound that increase only of a few dB when the Mach increases from 0.5 to 1. Moreover the large scales sound spectra increase more than the low scales and don't change the shape of the spectra.

The wavelet approach gives also separated signals without the loss of the phase information; this feature permits to perform simultaneous velocity and acoustic measurements using hot-wire and microphones in the near field. The signal from the microphones is split in sound and pseudo-sound. These signals are cross-correlated with velocity data. The correlation

peaks indicates the zones of the jet that influence the sound and the pseudo-sound pressure fluctuations. The main sound generation position is at the end of the potential core as observed in literature. The core contractions are the main cause of the sound emission and present spectral components similar to the sound spectra. The autocorrelation of the jet velocity and the sound-velocity cross-correlation show a characteristic frequency peak evident also in all the measured spectra. Pseudo-sound pressure fluctuations are influenced by some zones on the jet axis; the main zone, as shown also in literature, is between 6 – 8 D.

A specific analysis of the core contraction events using a threshold algorithm makes reasonable to assume that the potential core contractions are an important noise production mechanism.

8.1 Future Works

These investigations give interesting results and confirm some theories. The data acquired during the present work needs deeper analysis for example conditioning the hot-wire measurements with the sound pressure events. Further investigations are needed to correlate also the low directivity angle spectra with the jet flow-dynamics.

PIV technique is suggested for future investigations to verify the correlation of the core contraction events with the sound and pseudo-sound emissions. This velocimetry technique can be applied synchronized with microphones to condition the velocity measurements with the sound events. The PIV may provide a complete view of the core dynamic in the presence of acoustic events. At the same time the PIV can be conditioned with the pseudo-sound events obtaining also a two-dimensional representation of the dynamics that cause the convective pressure fluctuations.

The filtering technique developed in this work can be used for the investigation of noise reduction method such chevron nozzles or micro-jets. The comprehension of the noise generation mechanisms is necessary for the optimization of these methods.

In this framework, future applications can include the real time filtering of the pressure fluctuations for the active control of the noise emissions.

Appendix A: Duct and Nozzle Design

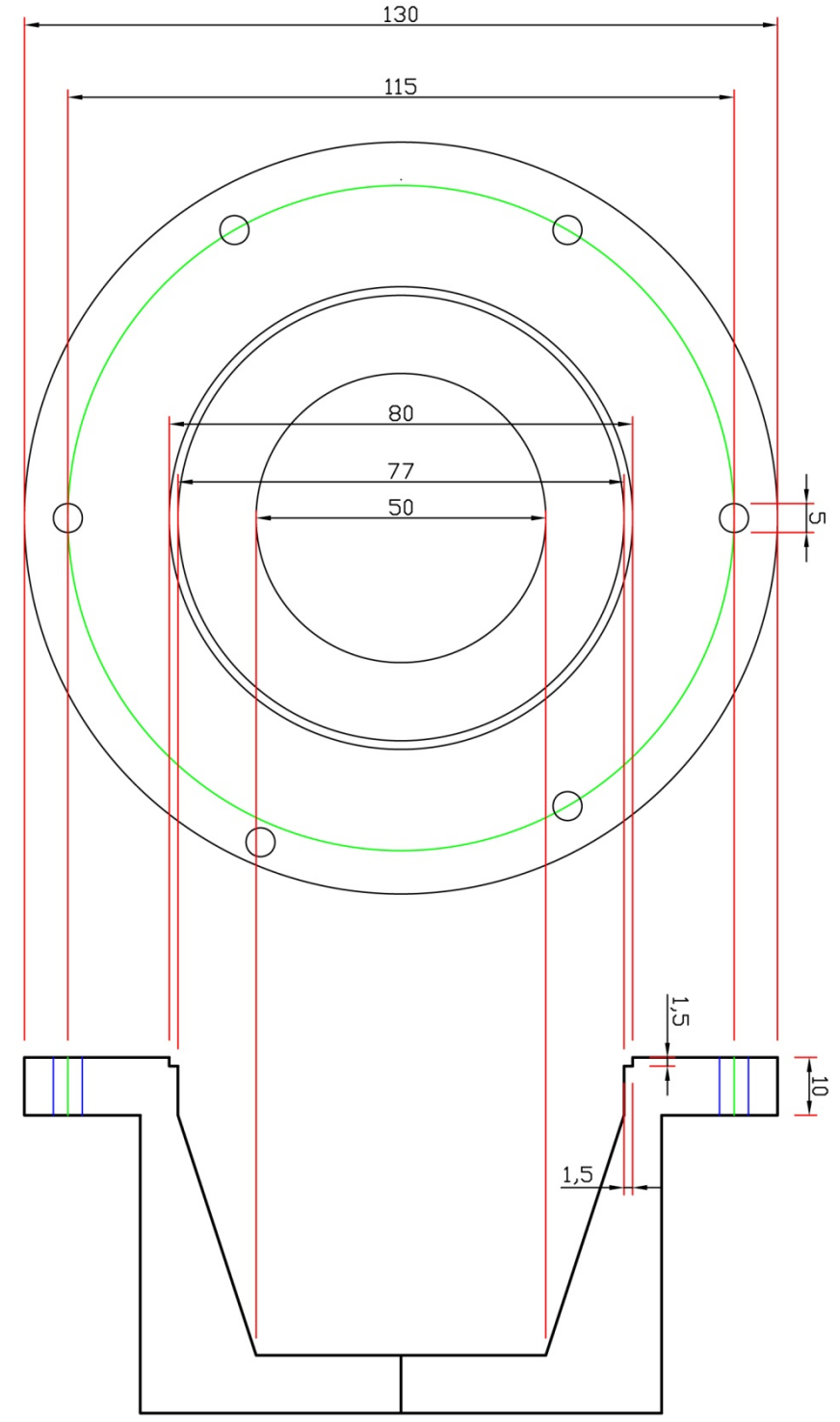

Figure 102: Divergent of the A section without the compressed air duct.

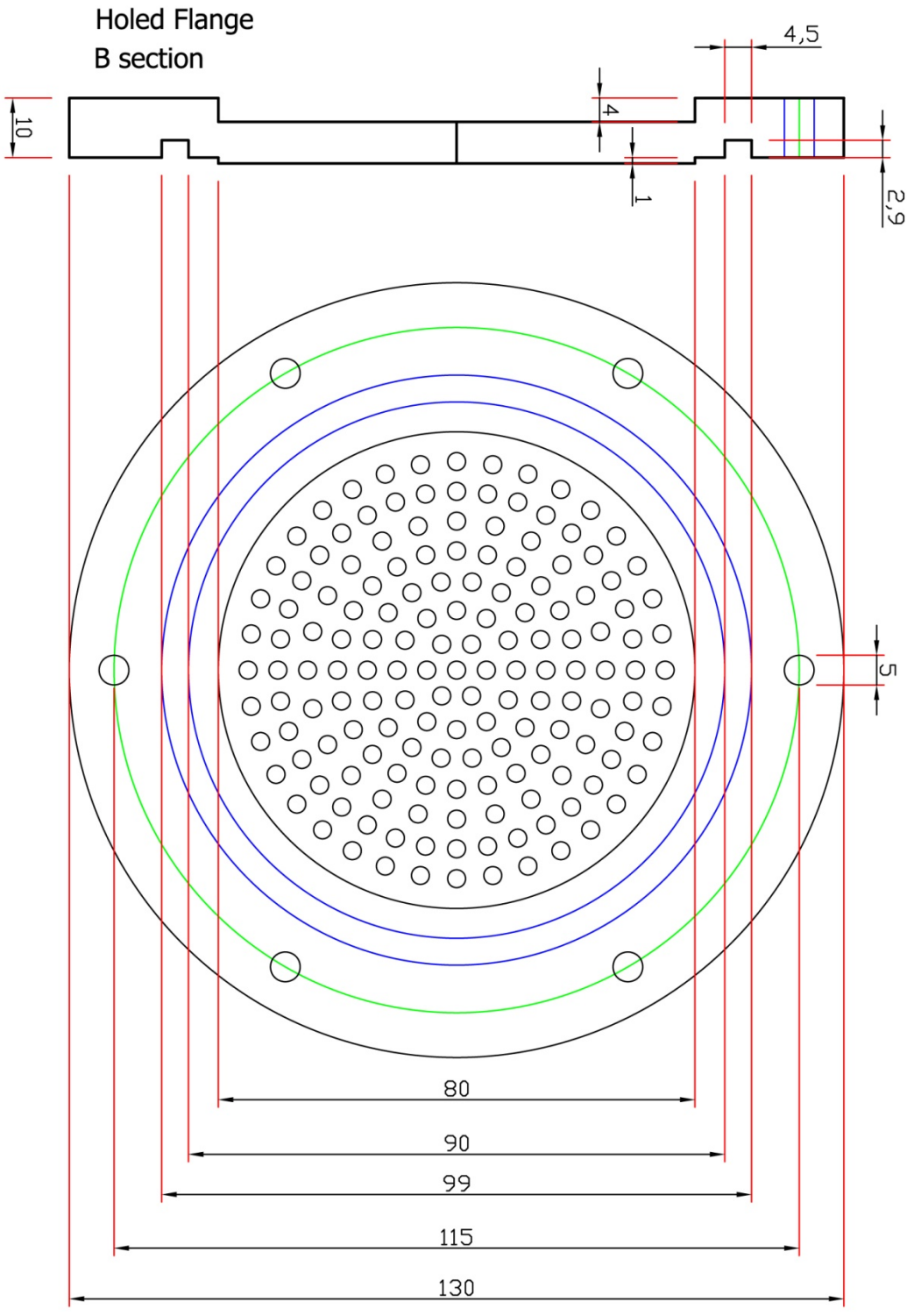

Figure 103: Holed Flange of the duct section [B].

F Section

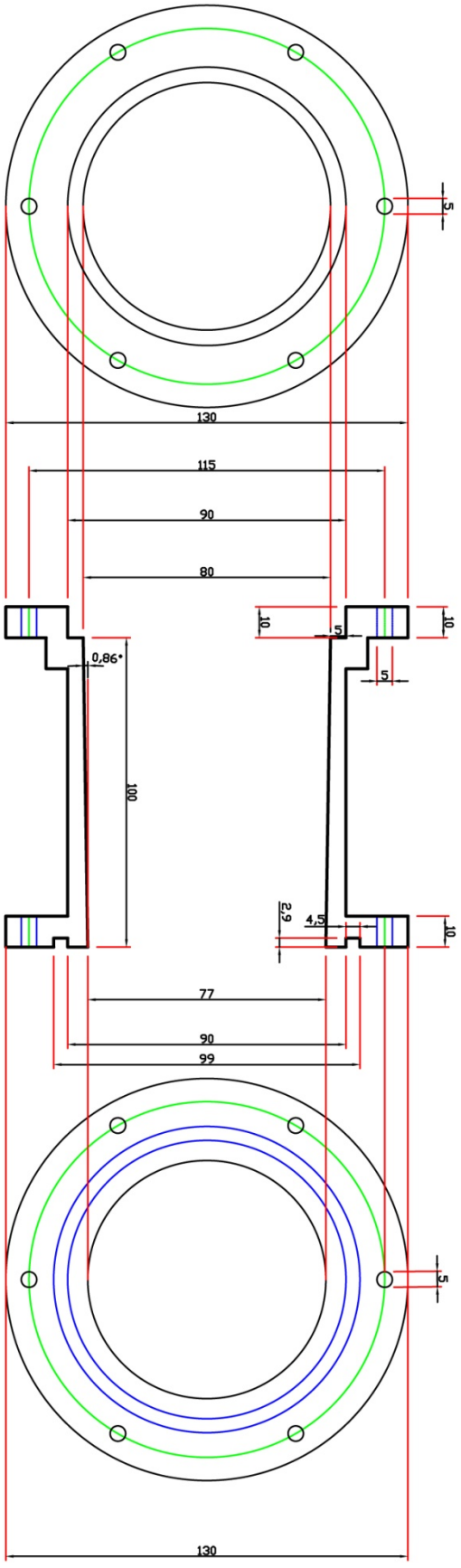

Figure 104: F Design and dimensions of the F section.

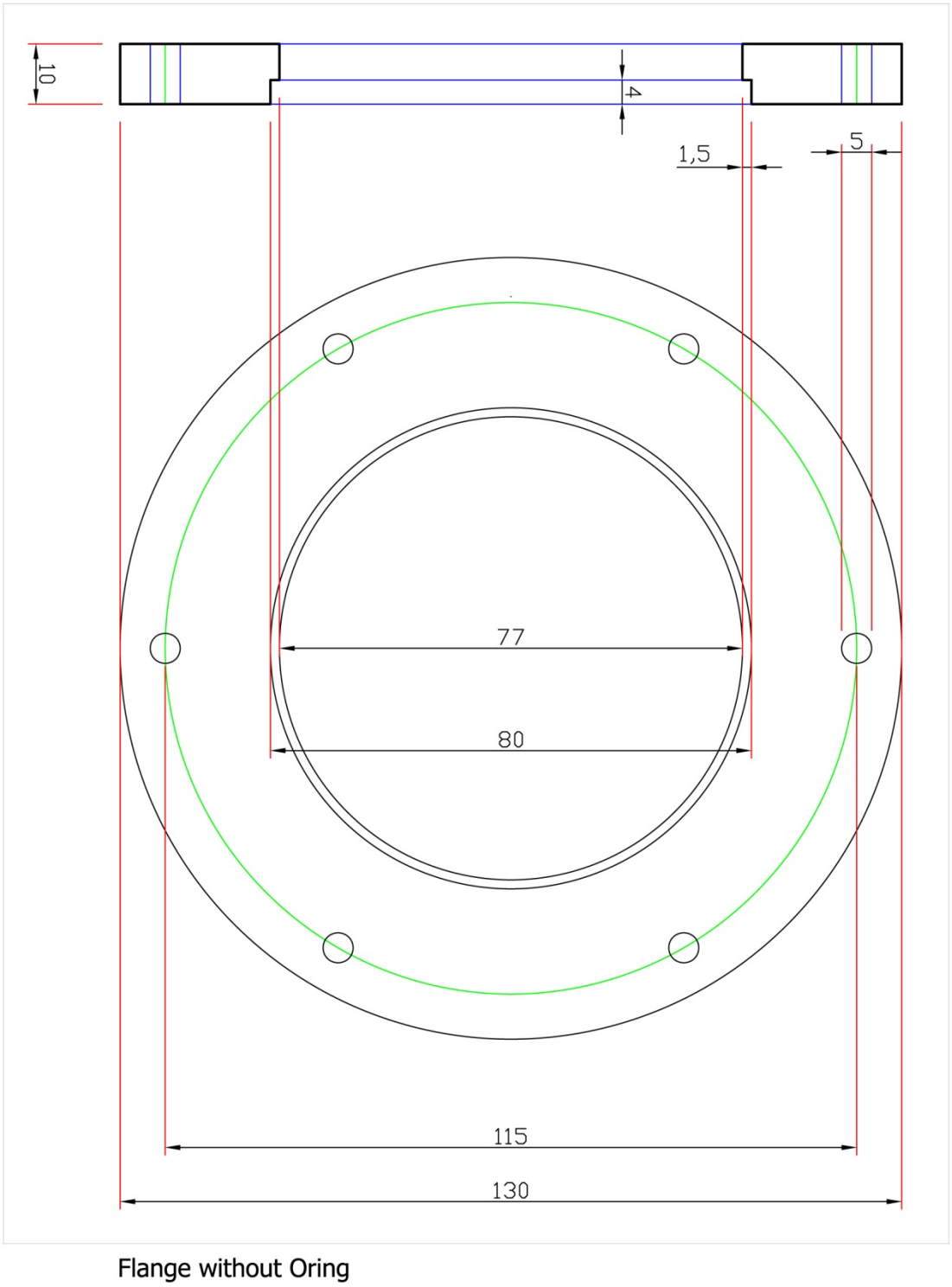

Figure 105: Junction Flange without O-ring.

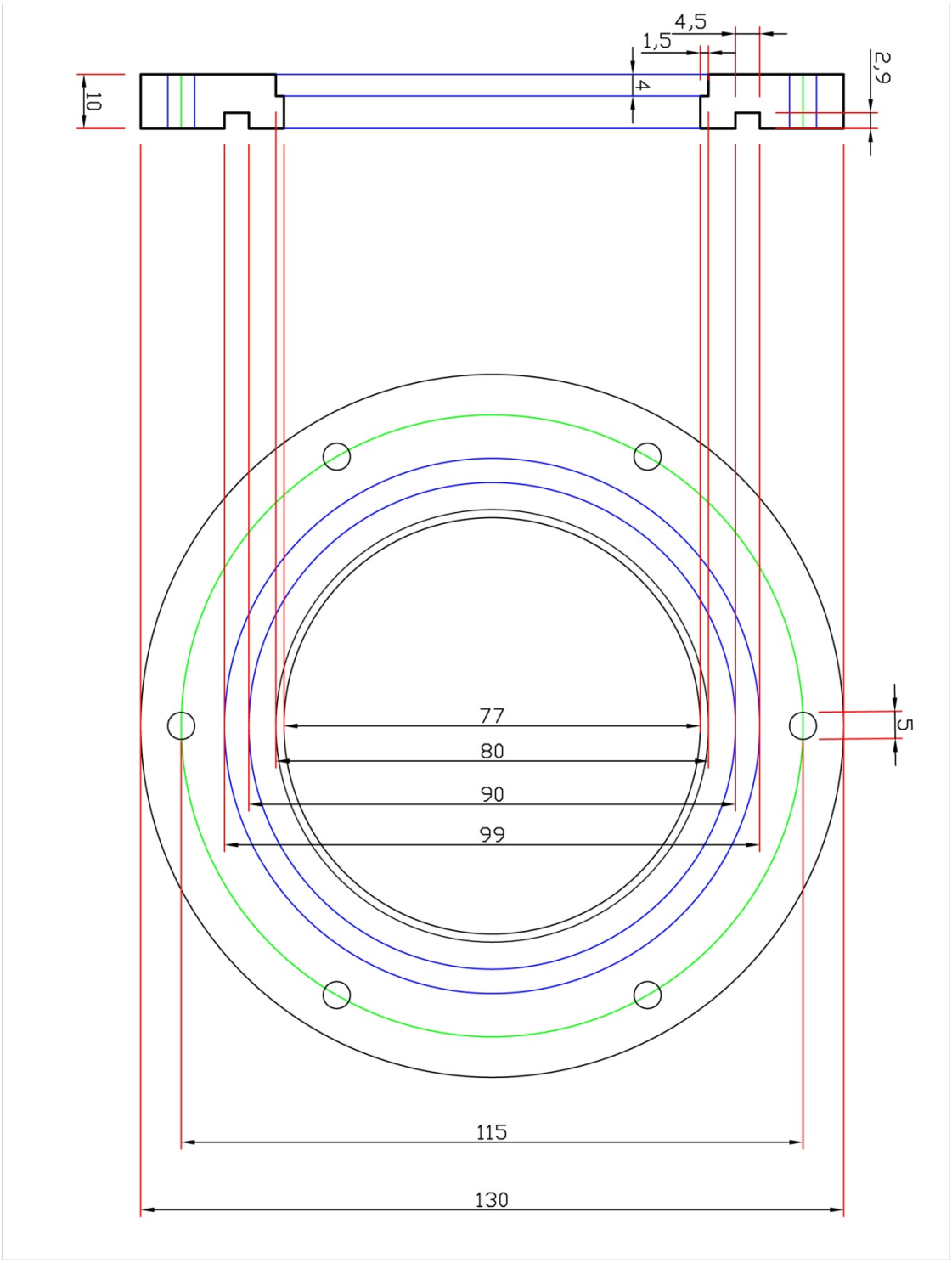

Figure 106: Junction Flange with O-ring.

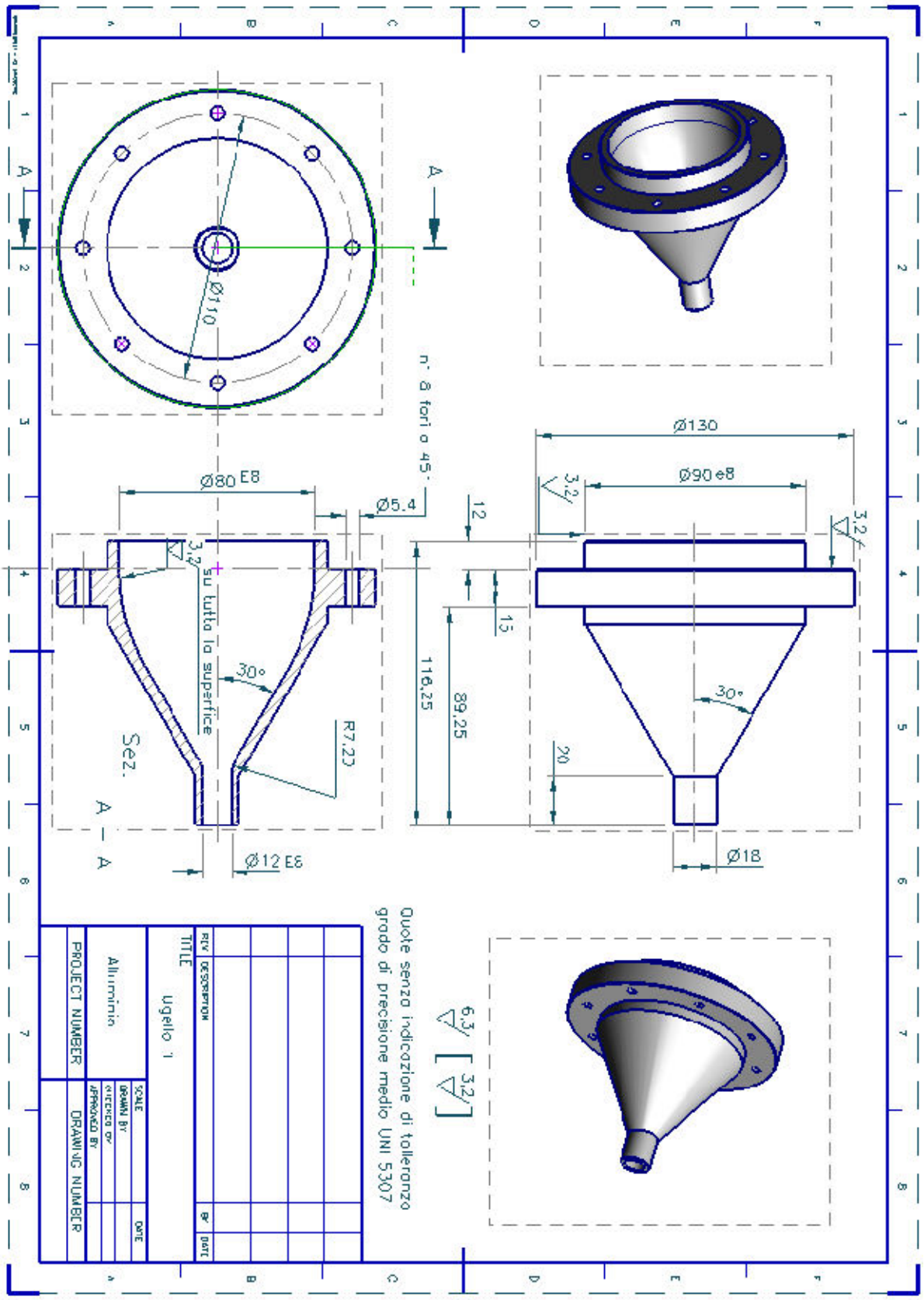

Figure 107: Nozzle design.

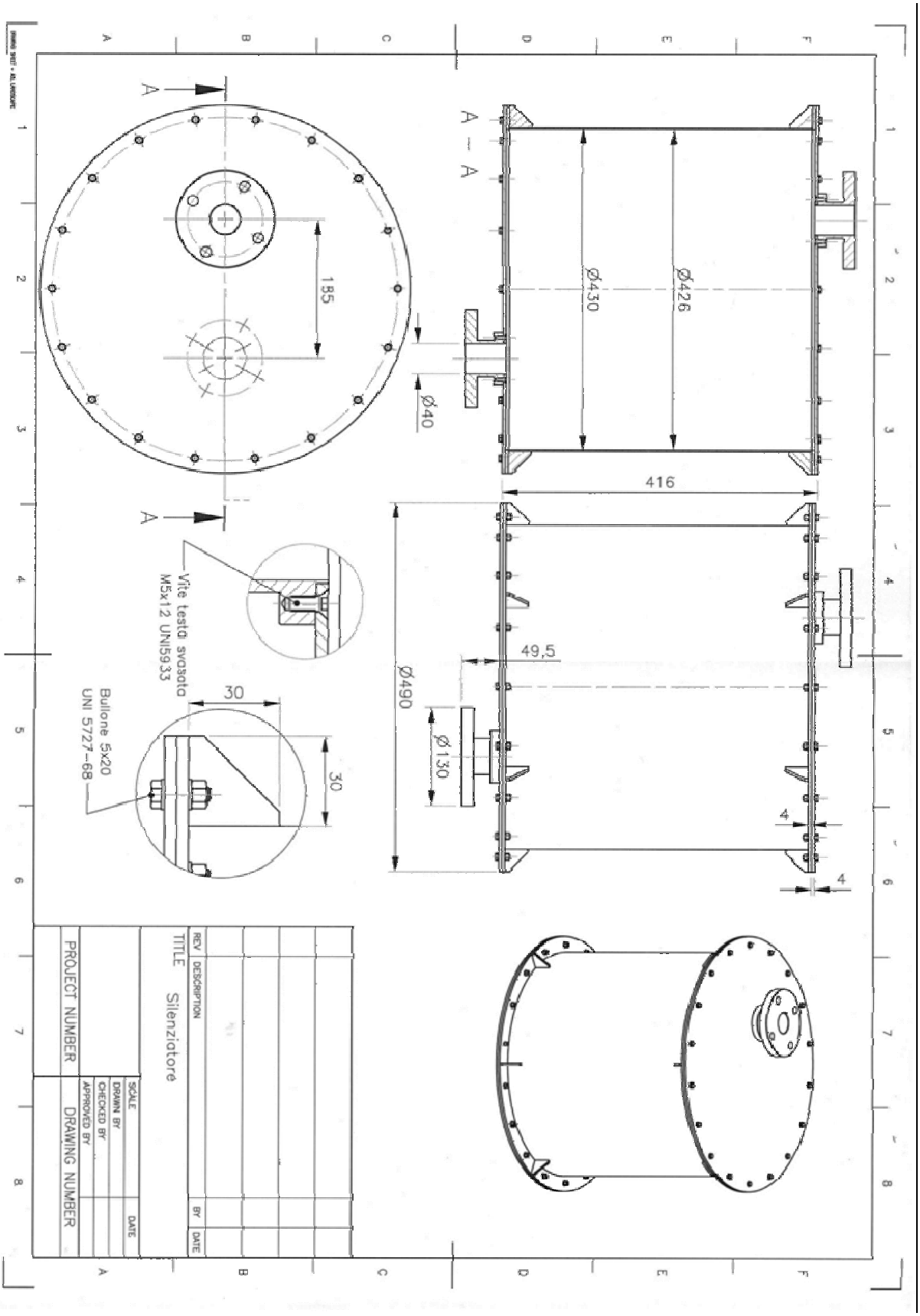

Figure 108: Muffler design.

Appendix B: Far-field Spectra

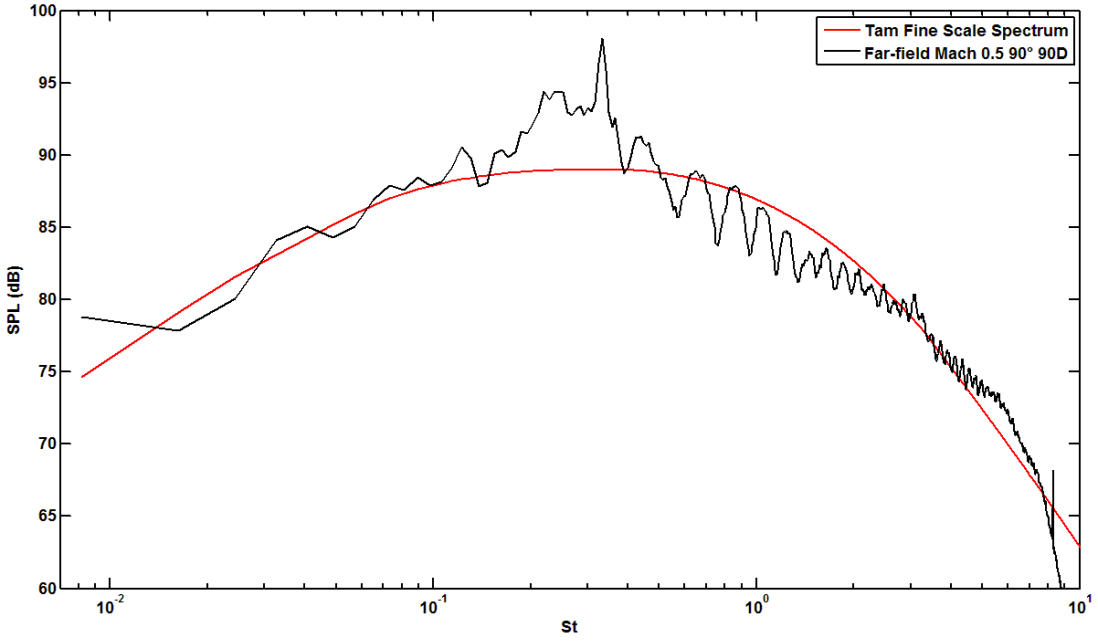

Figure 109: Far-field Spectrum at Mach 0.5, direction 90°, distance 90 diameters; comparison with Tam fine scale spectrum

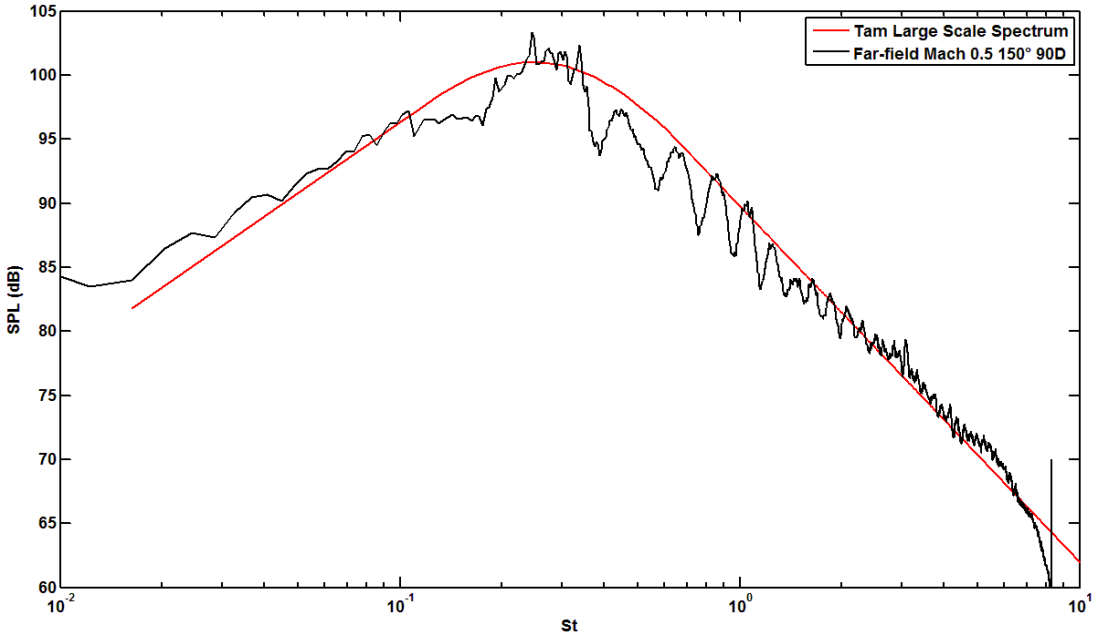

Figure 110: Far-field Spectrum at Mach 0.5, direction 150°, distance 90 diameters; comparison with Tam large scale spectrum

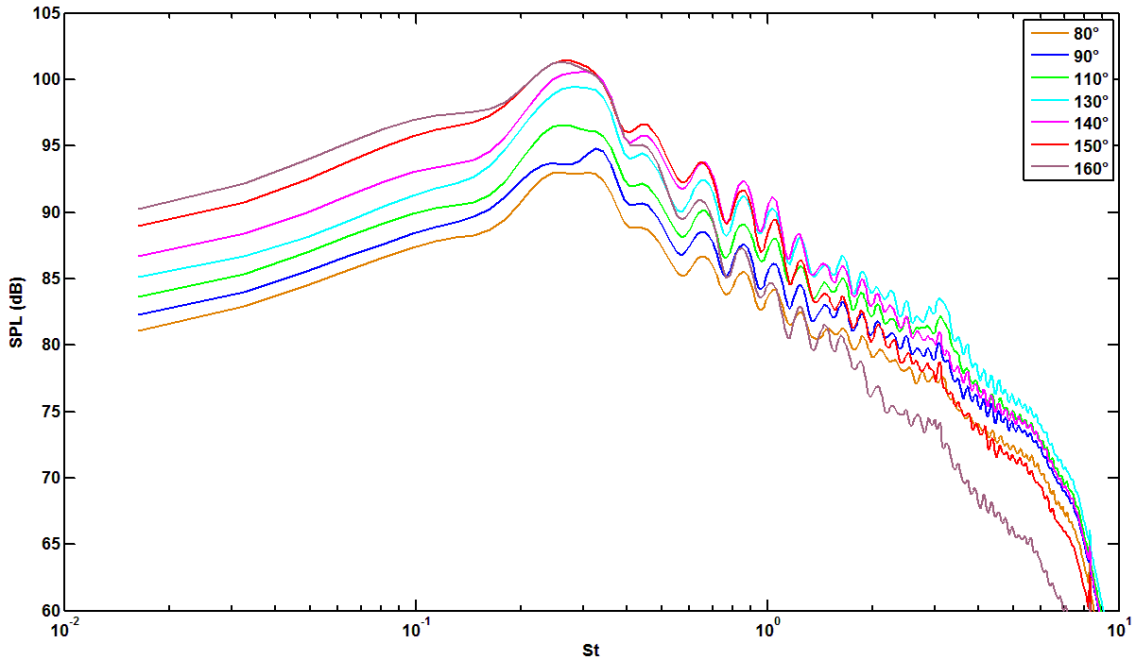

Figure 111: Far-field spectra comparison at Mach 0.5; distance 90 diameters.

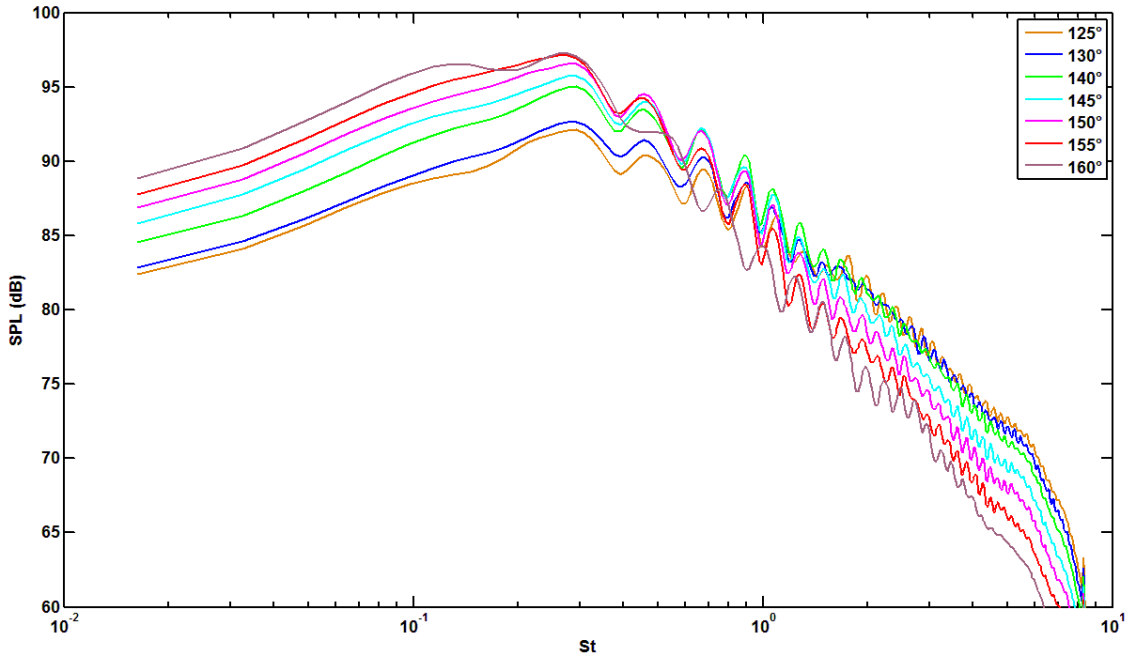

Figure 112: Far-field spectra comparison at Mach 0.5; distance 120 diameters.

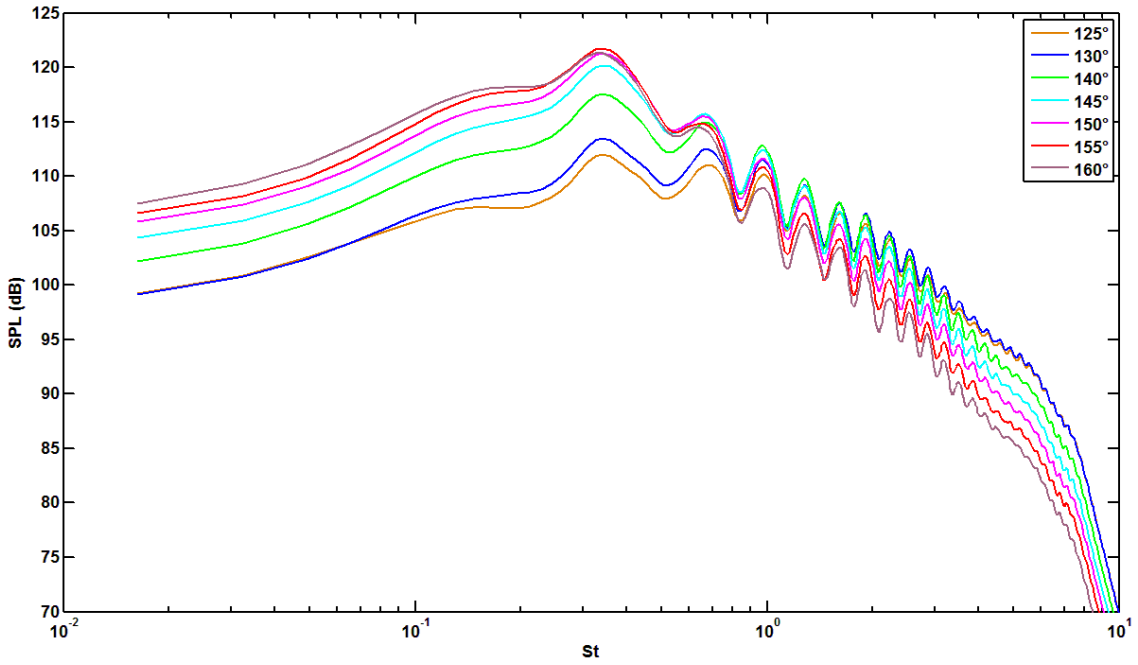

Figure 113: Far-field spectra comparison at Mach 1; distance 120 diameters.

Appendix C: Near-field Spectra

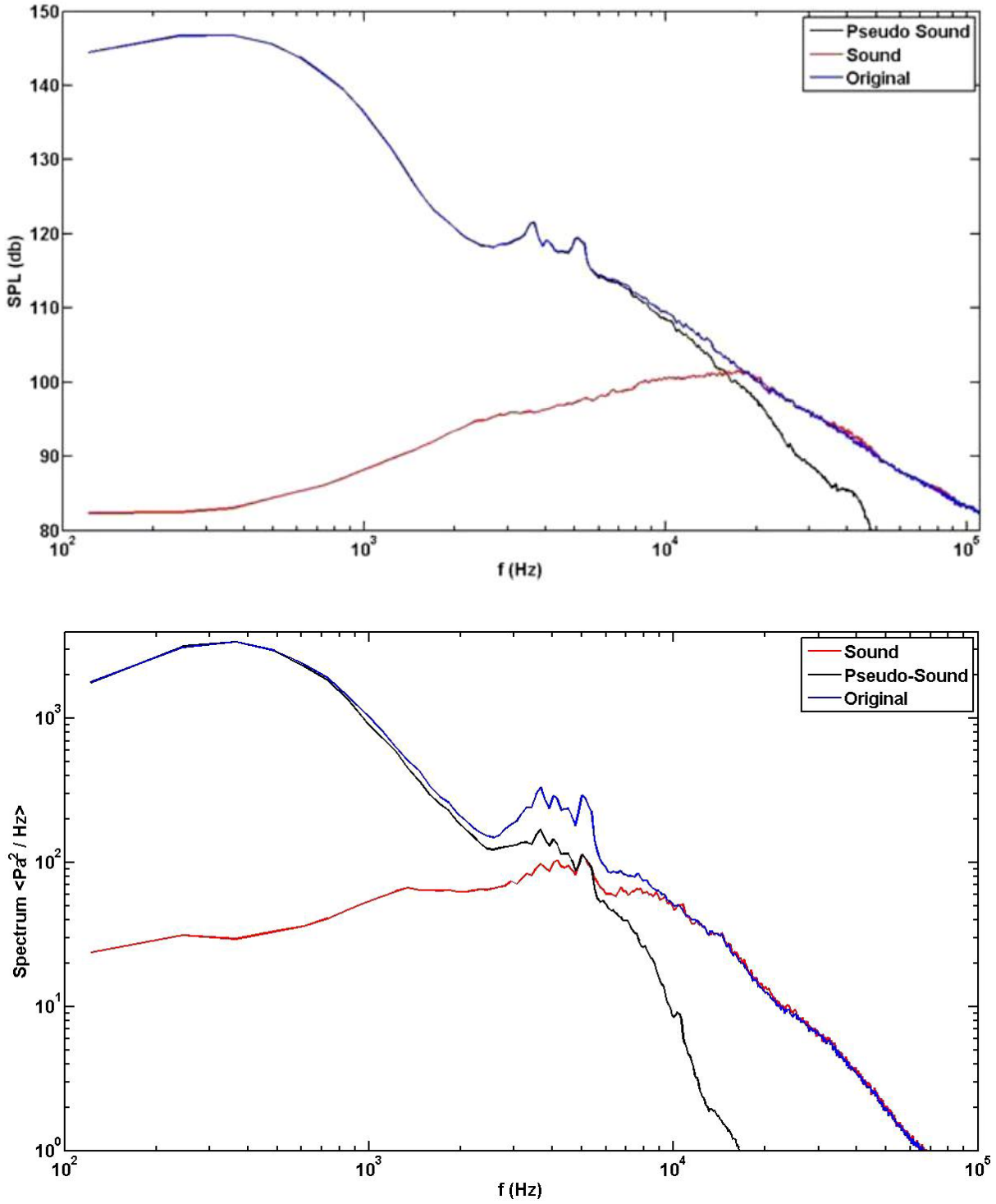

Figure 114: Filtering of Sound and Pseudo-Sound from near-field signals

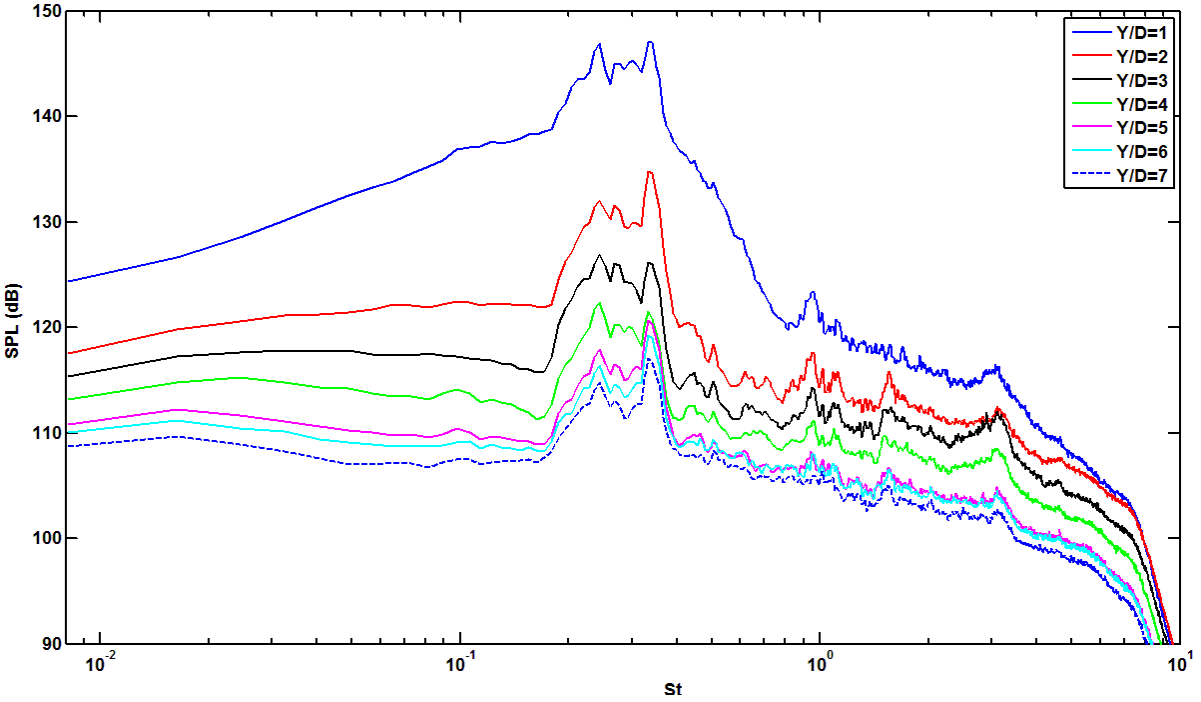

Figure 115: Near-Field Total Spectra at X/D = 1.16

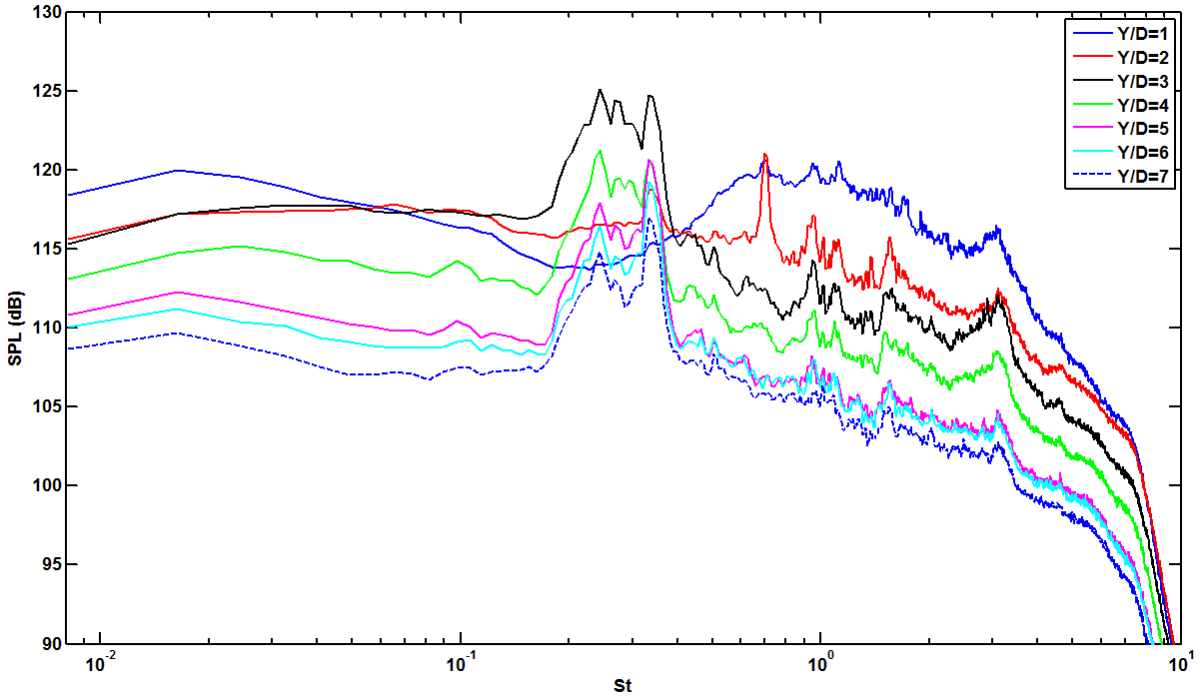

Figure 116: Near-Field Sound Spectra at X/D = 1.16

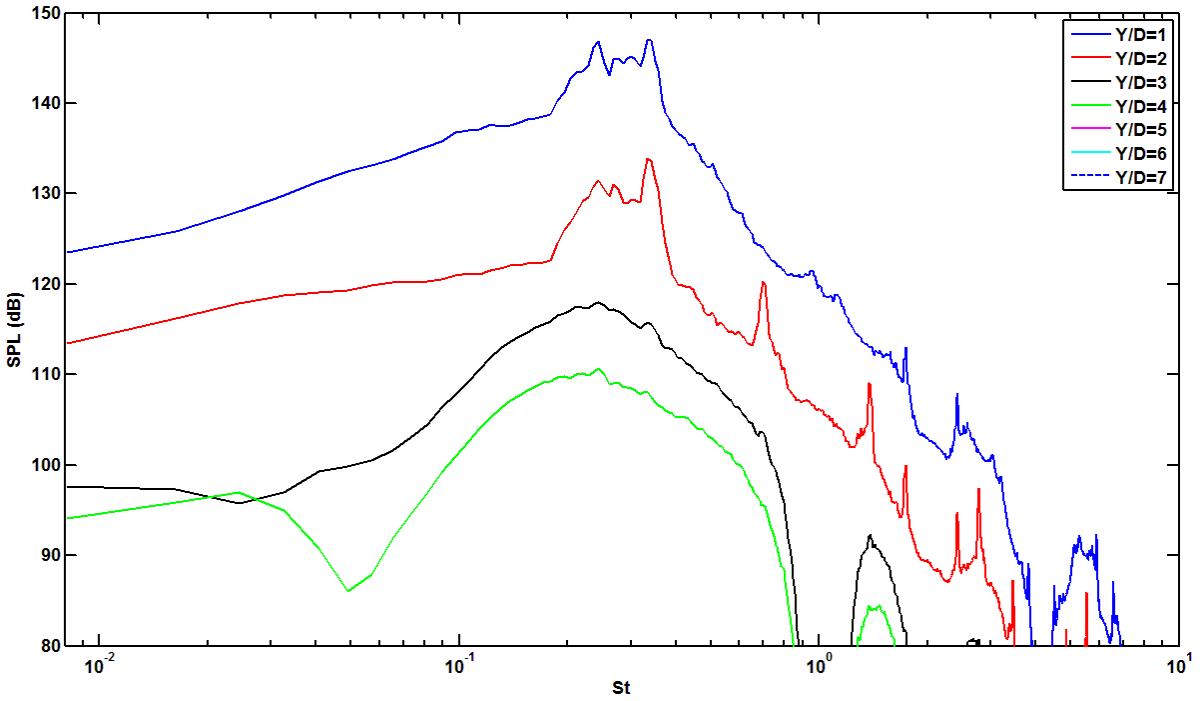

Figure 117: Near-Field Pseudo-Sound Spectra at X/D = 1.16

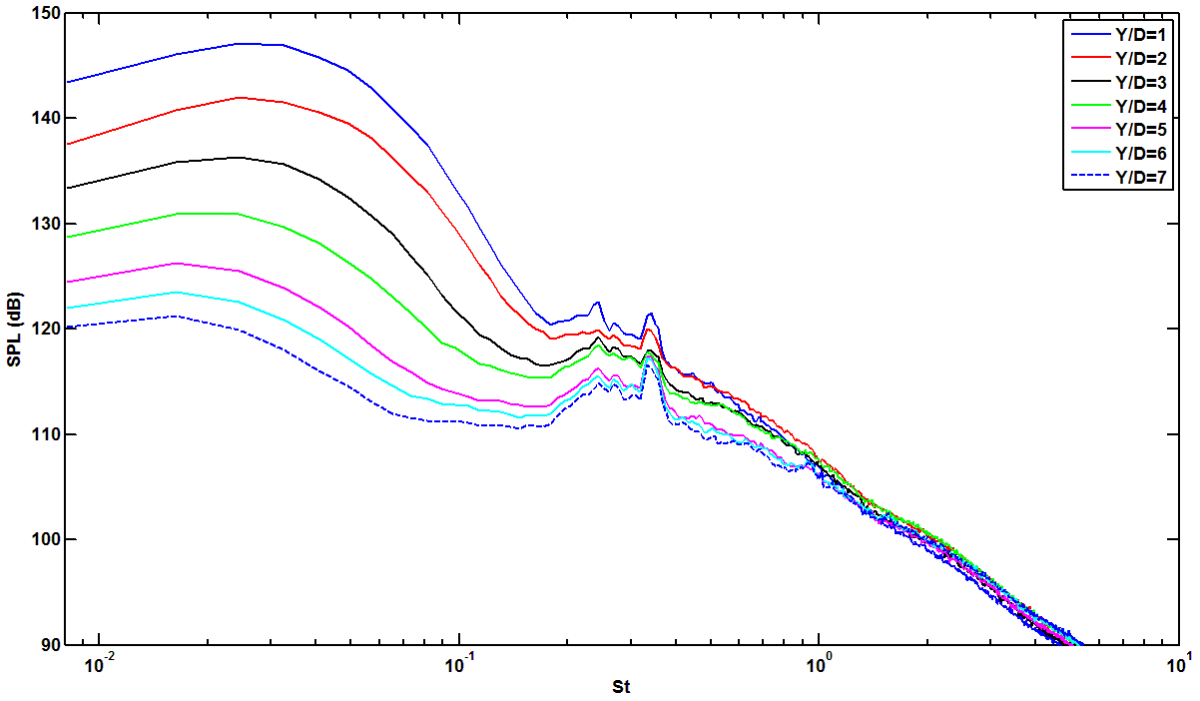

Figure 118: Near-Field Total Spectra at X/D = 12.83

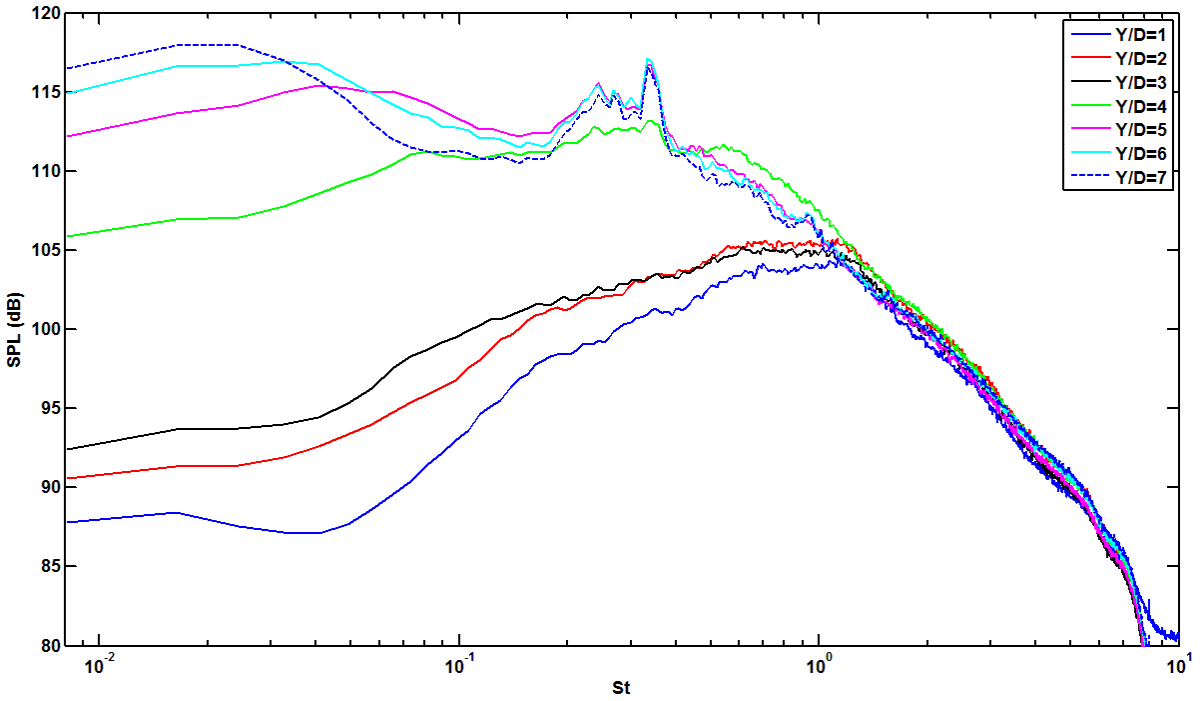

Figure 119: Near-Field Sound Spectra at X/D = 12.83

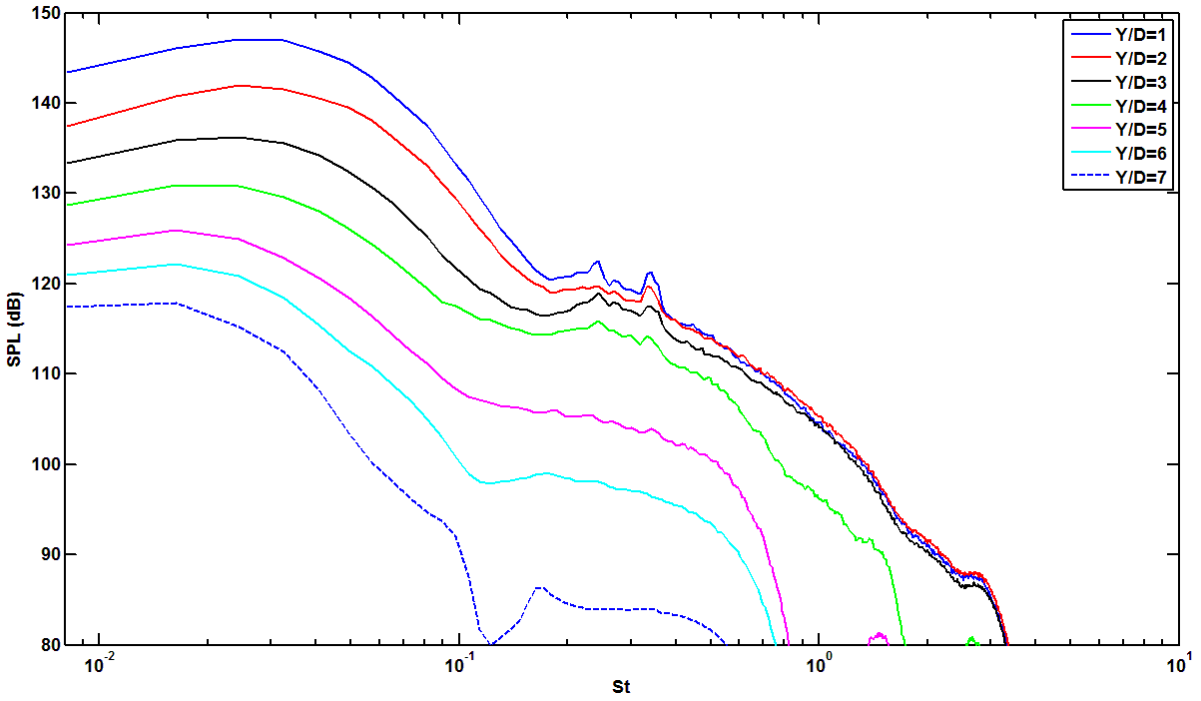

Figure 120: Near-Field Pseudo-Sound Spectra at X/D = 12.83

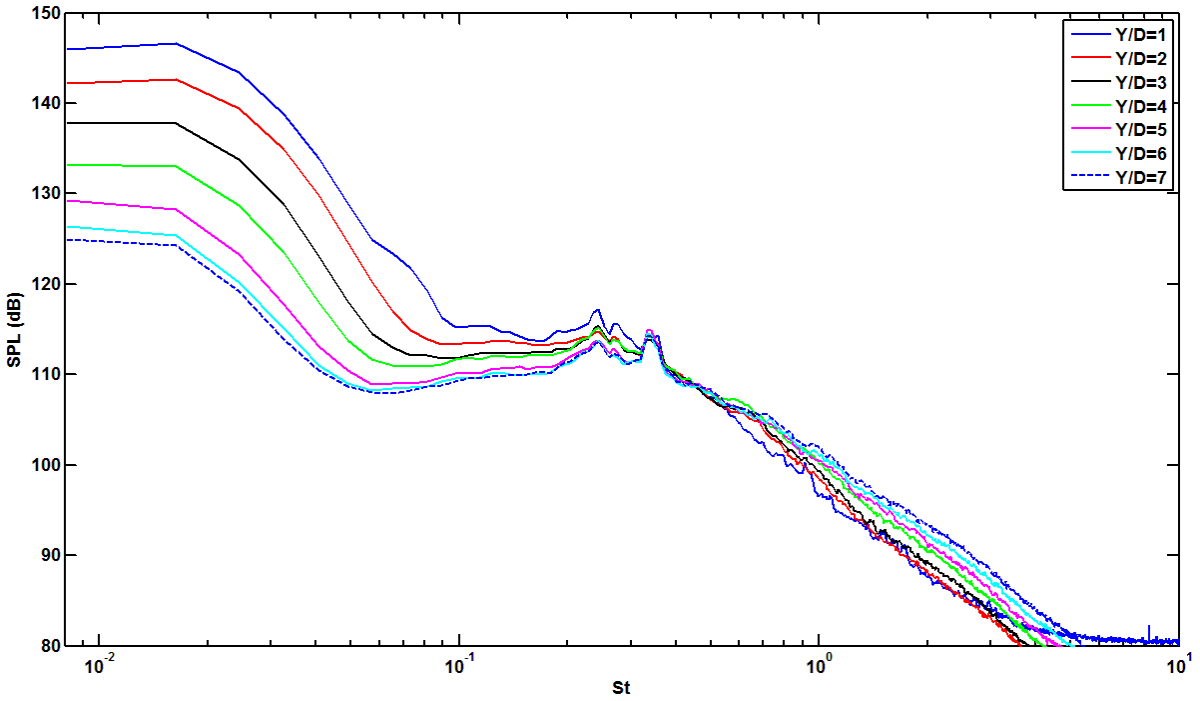

Figure 121: Near-Field Total Spectra at X/D = 22.16

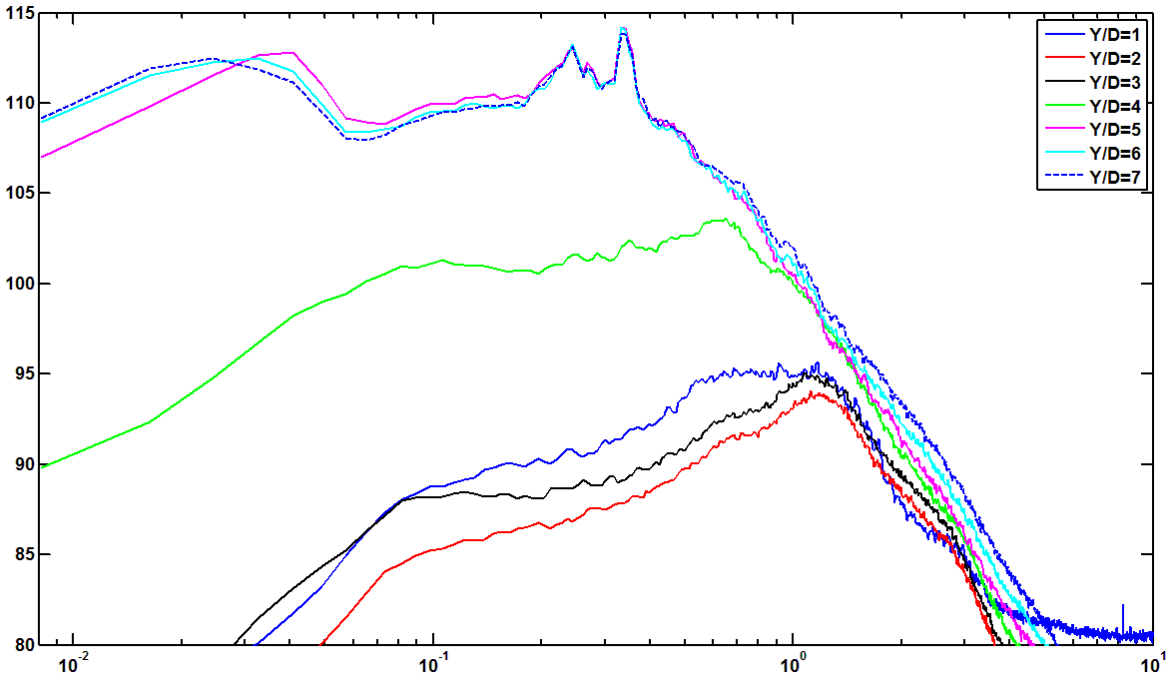

Figure 122: Near-Field Acoustic Spectra at X/D = 22.16

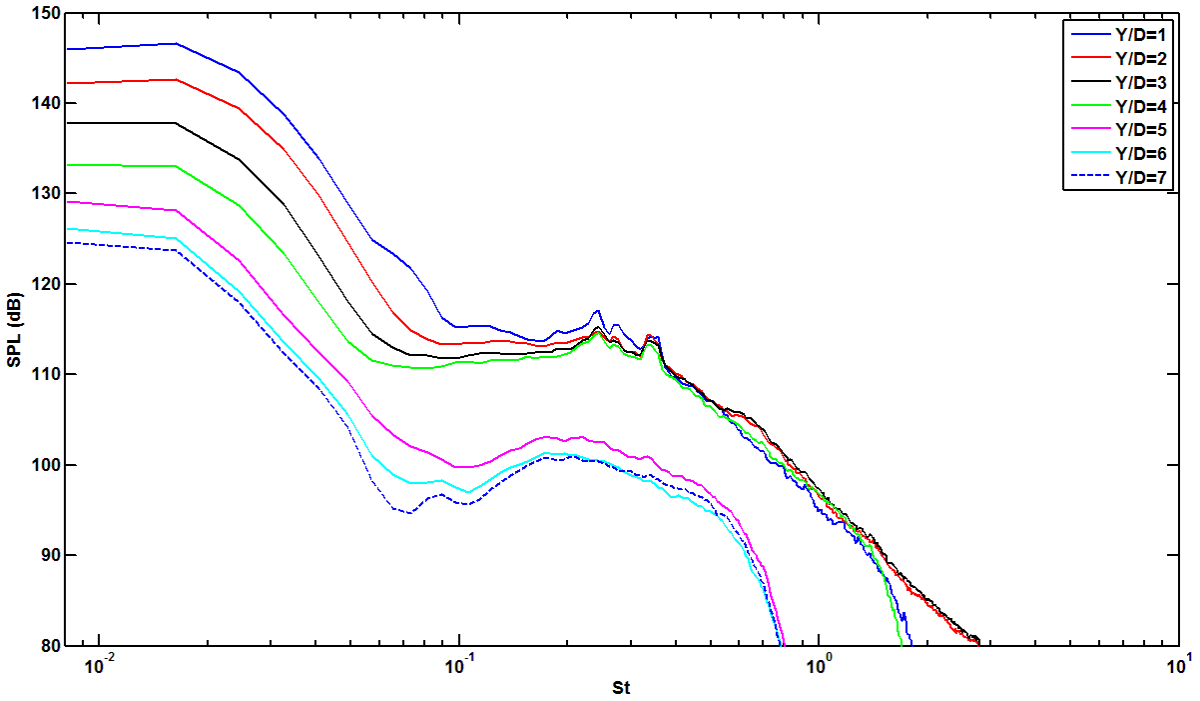

Figure 123: Near-Field Pseudo-Sound Spectra at X/D = 22.16

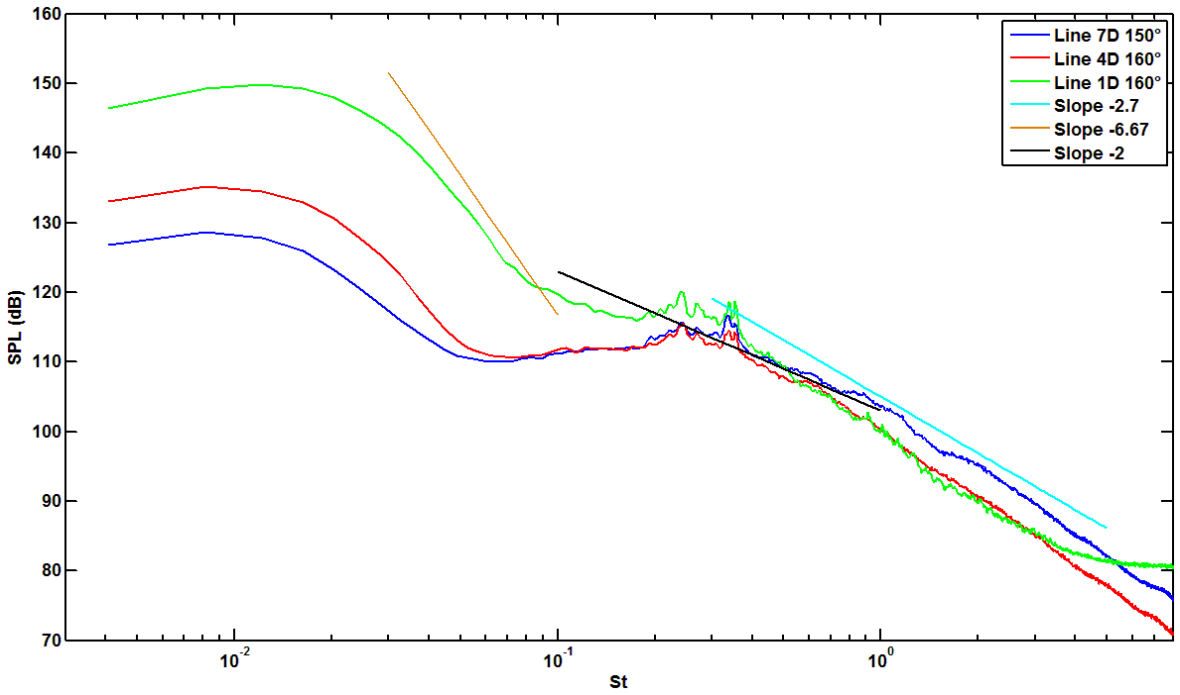

Figure 124: Near-field spectra with characteristic slopes.

Appendix D: Near-field, Hot-Wire measurements

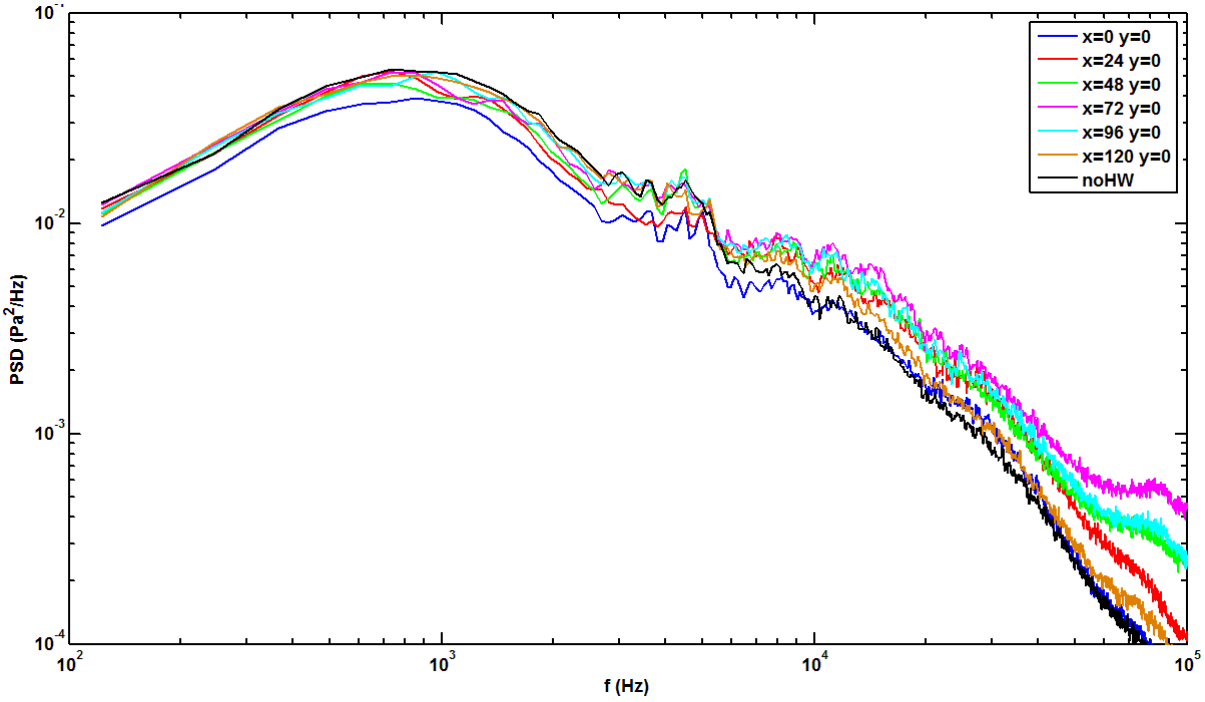

Figure 125: Hot-wire effects at Mach 0.7 along the centre line

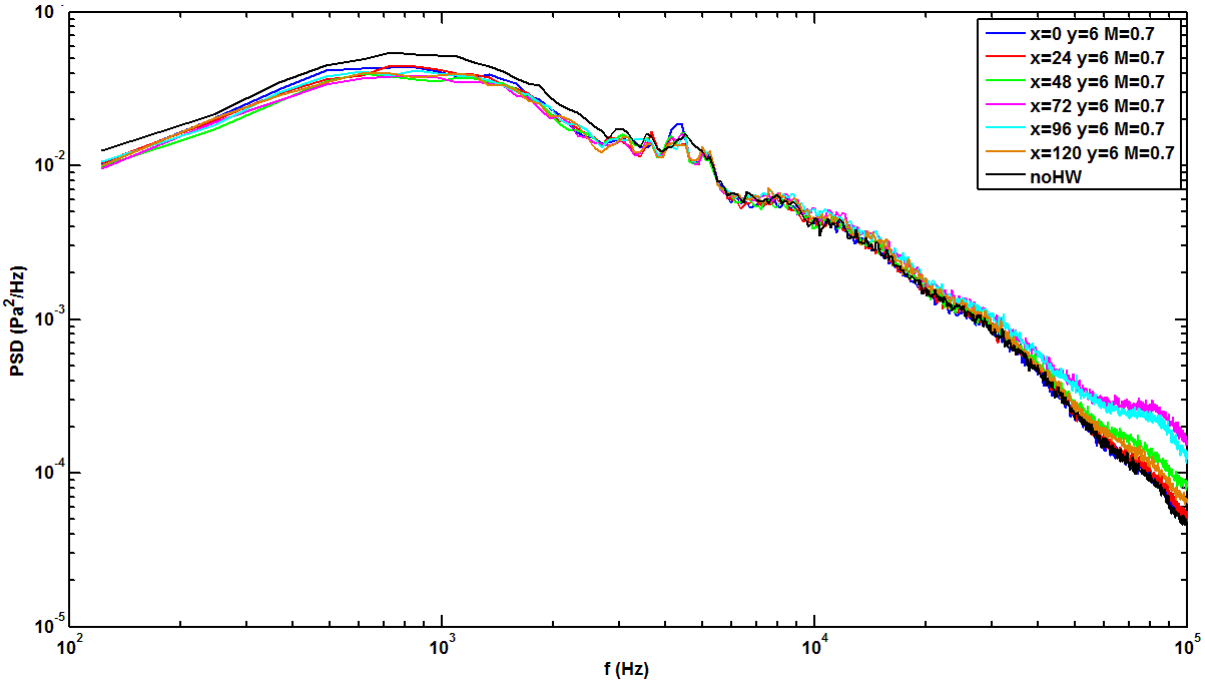

Figure 126: Hot-wire effects at Mach 0.7 along the border line

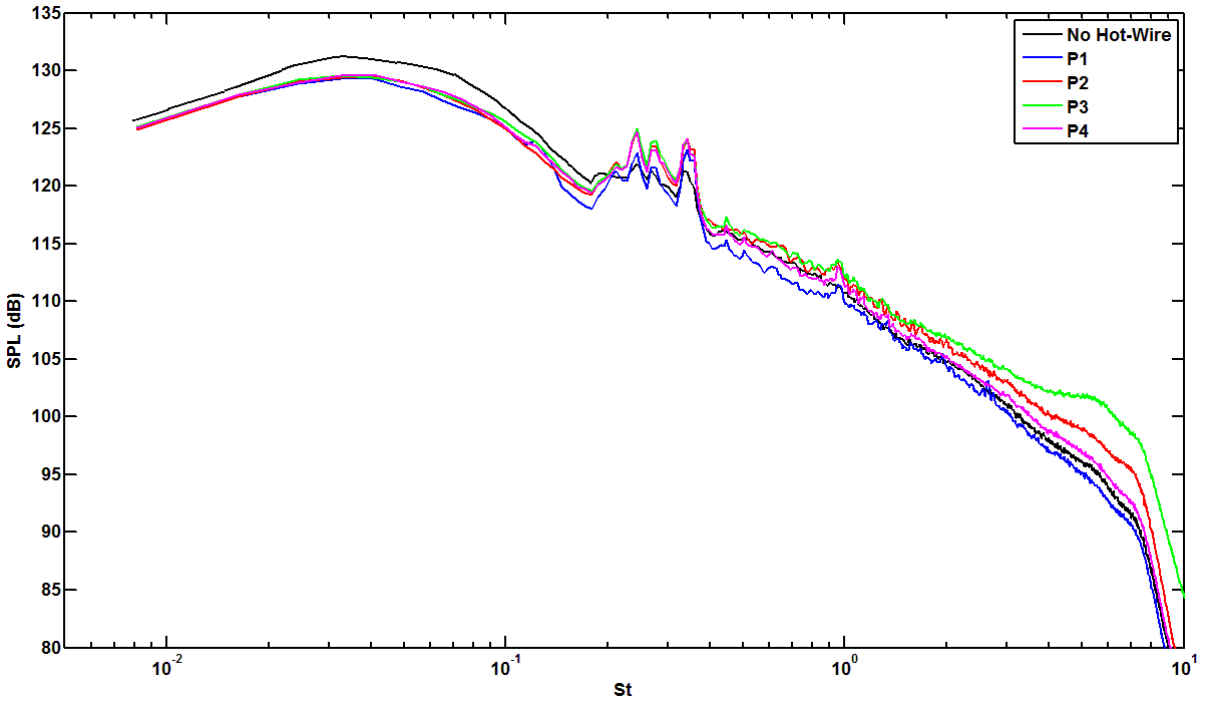

Figure 127: Hot-wire influence at Mach 0.5 on the pressure fluctuations

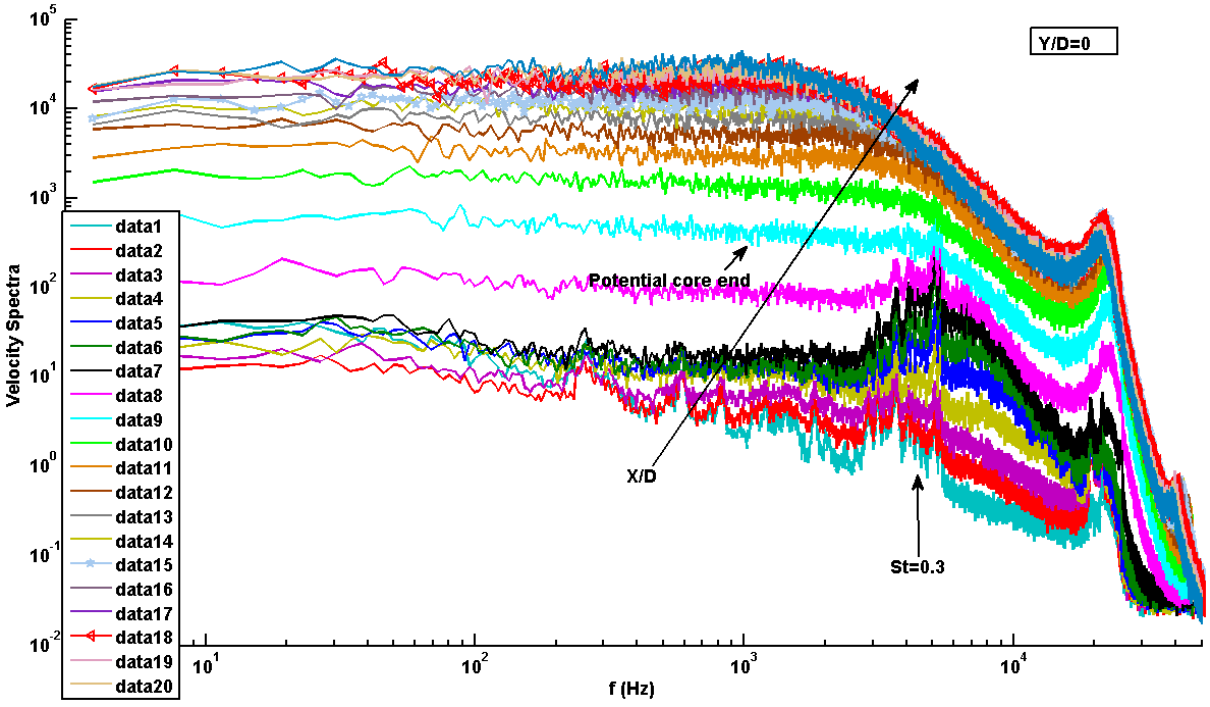

Figure 128: Velocity Spectra of the hot-wire measurements on the jet axis (Y/D=0)

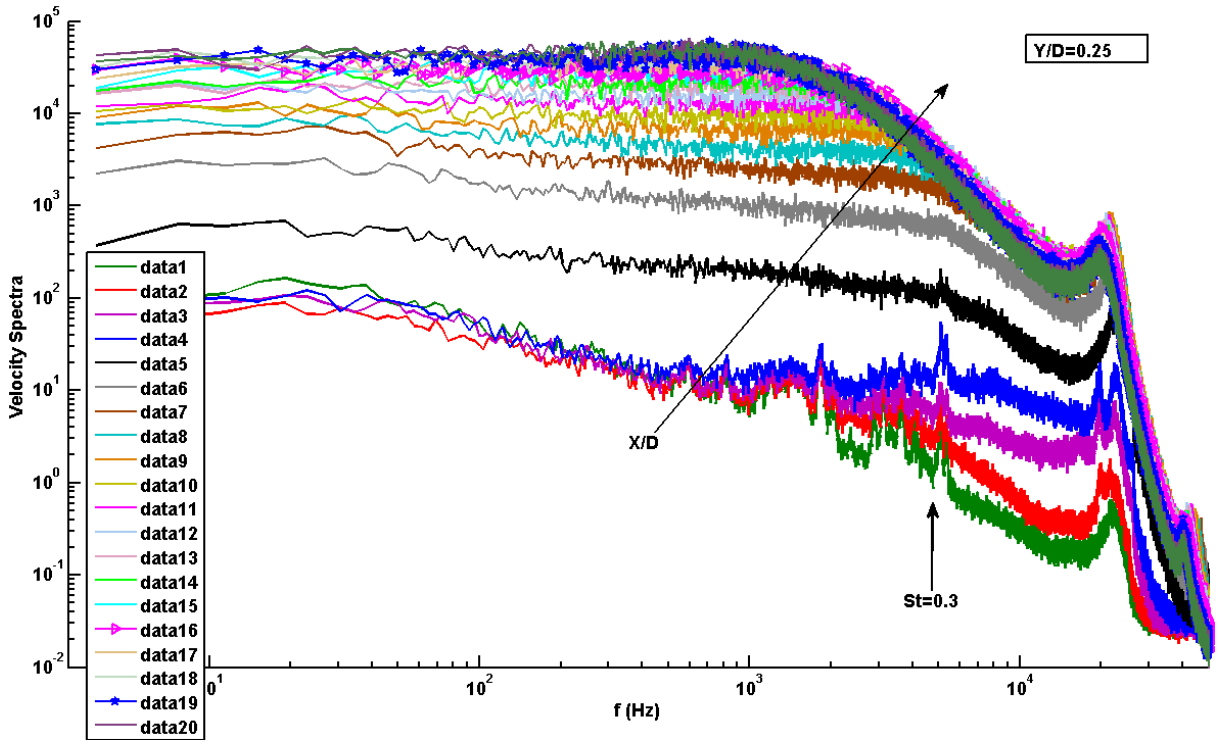

Figure 129: Velocity Spectra of the hot-wire measurements on the line Y/D=0.25

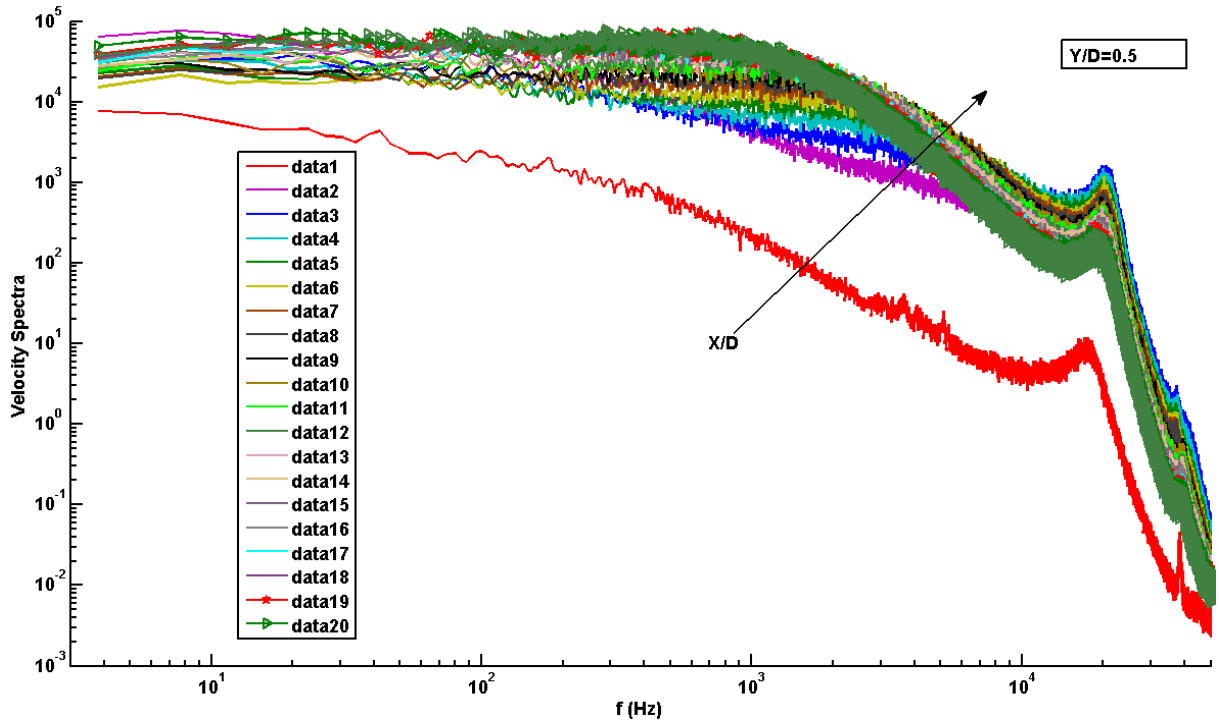

Figure 130: Velocity Spectra of the hot-wire measurements on the jet leap line (Y/D=0.5)

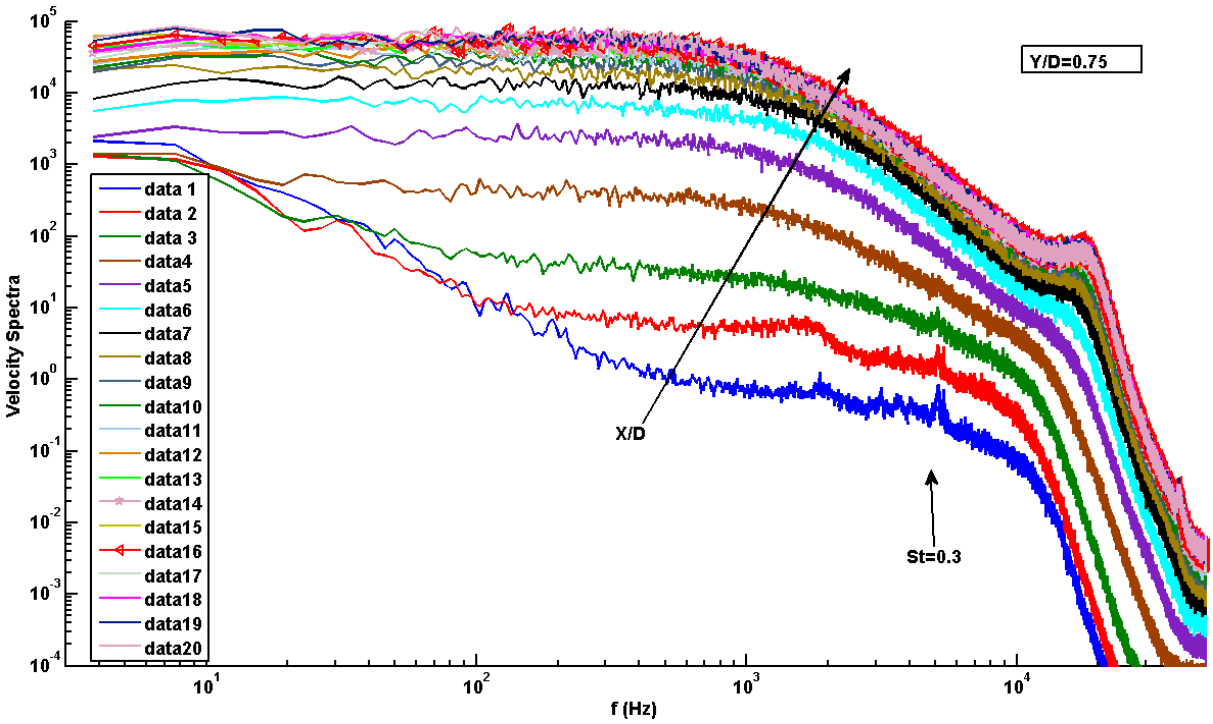

Figure 131: Velocity Spectra of the hot-wire measurements on the line Y/D=0.75

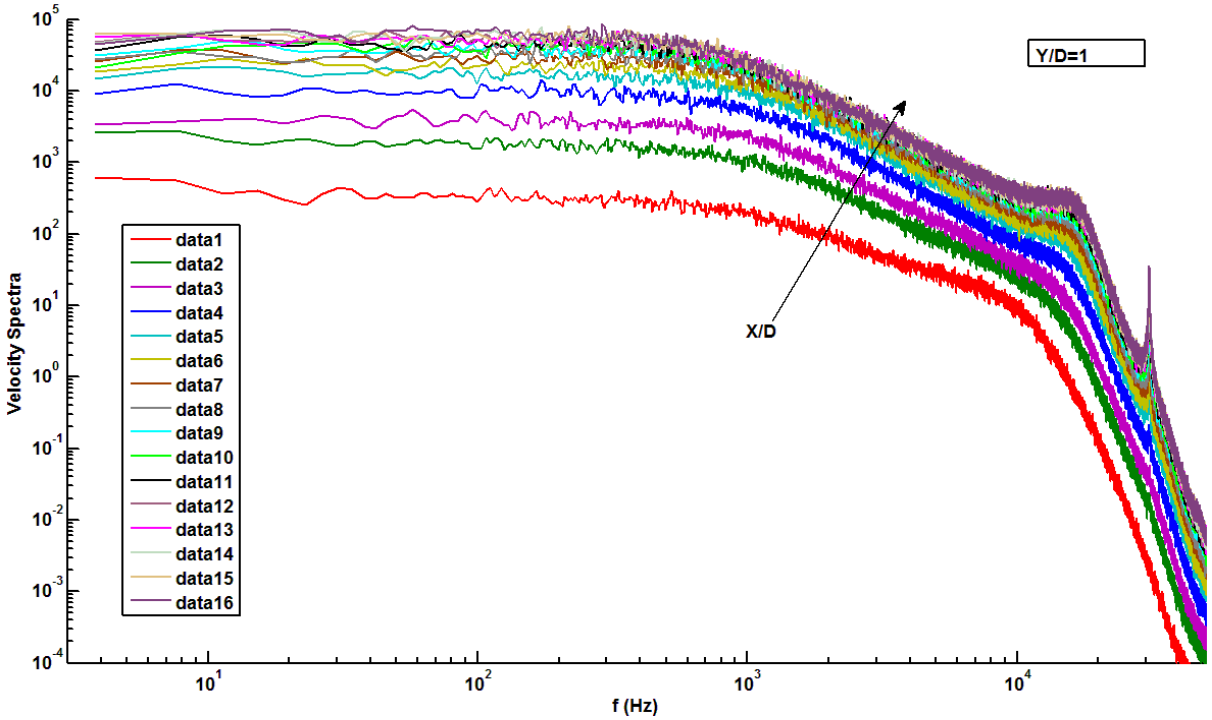

Figure 132: Velocity Spectra of the hot-wire measurements on the line Y/D=1

Bibliography

Albertson et. Al., 1950, for these data see Rajaratnam 1976

Atvars J., Schubert L.K., Ribner H.S., 1964, "Refraction of Sound from a Point Source Placed in an Air Jet"; The Journal of the Acoustical Society of America 37

Agrawal A., Prasad A. K, 2003, "Integral Solution for the Mean Flow Profiles of Turbulent Jets, Plumes, and Wakes"; Journal of Fluids Engineering 125, 813 – 822

Ahuja K.K., 2003, "Designing clean jet-noise facilities and making accurate jet-noise measurements"; International Journal of Aeroacoustics, 2.3

Becker H.A., Hottel H.C. and Williams G.C., 1967, "The Concentration Field of a Free Jet"; Journal of Fluid Mechanics

Bell L.H., Bell D.H., 1994, "Industrial Noise Control: Fundamentals and Application, second edition, revised and expanded"; Marcel Dekker Inc

Bodony D. J., 2005, "The prediction and understanding of jet noise"; Center for Turbulence Research Annual Research Briefs, Stanford

Camussi R., Guj G., 1997, "Orthonormal wavelet decomposition of turbulent flows: intermittency and coherent structures"; Journal of Fluid Mechanics, Vol. 348

Camussi R., Guj G., 2000, "Wavelet analysis of turbulence data: coherent structures identification and intermittency"; Non Linear Instability, Chaos and Turbulence, Vol. II, L. Debnath e D.N. Rihani editors, Wit Press, Computational Mechanics Publications

Camussi R., 2002, "Coherent structures identification from Wavelet analysis of PIV bidimensional velocity fields"; Experiments in Fluids, Vol. 32

Camussi R., Felli M., 2005, "Far field pressure fluctuations and coherent structures in a low mach number turbulent jet flow"; International Journal of Aeroacoustics, Volume 3, Number 4

Camussi R., Robert G., Jacob M. C., 2008, "Cross-Wavelet analysis of wall pressure fluctuations beneath incompressible turbulent boundary layers"; Journal of Fluid Mechanics, Vol. 617

Camussi R., Jacob M. C., Grilliat J., Caputi Gennaro G., 2010, "Experimental study of a tip leakage flow: wavelet analysis of pressure fluctuations"; Journal of Fluid Mechanics, Vol. 660

Cenedese A., Doglia G., Romano G. P., De Michele G., Tanzini G., 1994, "LDA and PIV Velocity Measurements in Free Jets"; Experimental and Thermal Fluid Science 9

Coiffet F., Jordan P., Delville J., Gervais Y., Richaud F., 2006, "Coherent structures in subsonic jets: a quasi-irrotational source mechanism"; International Journal of Aeroacoustics, 5(1)

Donoho D. & Johnstone I., 1994, "Ideal spatial adaptation via wavelet shrinkage"; Biometrika, 81

Dowling D.R. and Dimotakis P.E., 1990, "Similarity of the concentration field of gas-phase turbulent jets"; Journal of Fluid Mechanics, 218

Ebrahimi I., and Kleine R., 1977, "Konzentrationsfelder in isothermermen Luft-Freistrahlen"- "Concentration fields in isothermal free air jets"; Forsch. Ing. 43

Farge M., 1992, "Wavelet transforms and their application to turbulence"; Annual Review Fluid Mechanic, 24

Fisher M. J., Morfey C. L., 2009, "Jet Noise"; Aeroacoustics Lecture Series, Chap. 14, University of Southampton

Ffowcs-Williams J., 1992, "Noise source mechanisms" – in: "Modern methods in analytical acoustics" – Lecture notes, Springer, Berlin Heidelberg New York

Frisch U. and She Z.S., 1991, "On the probability density function of the velocity gradients in fully developed turbulence"; Fluid Dynamics Research, 8

Glushko V.P., 1935, "Ракеты, их устройство и применение" *[Rakety, ikh ustroistvo i prime nenie]*, "Missiles, organization and use"; Moscow-Leningrad.

Grandmaison E.W. and Becker H.A., 1982, "Turbulent mixing in free swirling jets"; The Canadian Journal of Chemical Engineering, 60

Graps A., 1995, "An introduction to wavelets"; IEEE computational Science and Engineering, 2

Grassucci D., Kerhervé F., Jordan P., Camussi R., Grizzi S., 2010, "Using Wavelet transforms and Linear Stochastic Estimation to study nearfield pressure and turbulent velocity signatures in free jets"; AIAA Paper 2010-3954, Stockholm

Grizzi S., Falchi M., Romano G.P., 2006, "Stereo PIV investigation of a round jet"; XIV AIVELA annual meeting, Rome

Guj G., Carley M., Camussi R., Ragni A., 2003, "Acoustic identification of coherent structures in a turbulent jet"; Journal of Sound and Vibration, 259

Guitton A., Jordan P., Laurendeau E., Delville J., 2007, "Velocity dependence of the near pressure field of subsonic jets: understanding the associated source mechanisms"; AIAA Paper, 2007-3661

Hileman J.I., Thurow B.S., Caraballo E.J., Samimy M., 2005, "Large-scale structure evolution and sound emission in high-speed jets: real-time visualization with simultaneous acoustic measurements"; Journal of Fluid Mechanics, 544

Hinze and Zijnen, 1949, for these data see Rajaratnam 1976

Horstman C.C. and Rose W.C., 1975, "Hot-wire anemometry in transonic flow"; NASA TM X-62,495

Howes W.L., 1960, "Similarity of far noise fields of jets"; NASA TR R-52

Hussein H. J., Capp S. P., George W. K., 1994, "Velocity measurements in a high-Reynolds-number, momentum-conserving, axisymmetric, turbulent jet"; Journal of Fluid Mech. 258

Jordan P. and Gervais Y., 2008, "Subsonic jet aeroacoustics: associating experiment, modelling and simulation"; Experiments in Fluids, 44

Jullien F., 1978, "The Effect of Conduction Error on the Hot Wire Measurements in a Turbulent Flow Near a Wall"; Letters in Heat and Mass Transfer, 5

Juvé D., Sunyach M., Comte-Bellot G., 1980, "Intermittency of the noise emission in subsonic cold jets"; Journal of sound and vibration, 71(3)

Kerhervé F., Guitton A., Jordan P., Delville J., Fortuné V., Gervais Y. and Tinney C., 2008, "Identifying the dynamics underlying the large scale jetnoise similarity spectra"; 14th AIAA CEAS Conference, 2008-3027

Kopiev V.F. and Chernyshev S.A., 1997, "Vortex Ring eigen-oscillations as a source of sound"; Journal of Fluid Mechanics, 341

Kopiev V.F., Zaitsev M., Chernyshev S.A., Kotova A.N., 1999, "The role of large-scale vortex in a turbulent jet noise"; AIAA paper 99-1839

Kopiev V.F., Zaitsev M., Chernyshev S.A., 2006, "Comparison of vortex ring noise theory with excited jet acoustic measurements"; 10th CEAS-ASC workshop, Trinity College, Dublin, Ireland

Lee I. and Sung H. J., 2002, "Multiple-arrayed pressure measurement for investigation of the unsteady flow structure of a reattaching shear layer"; Journal of Fluid Mechanics, 463

Lighthill M. J., 1952, "On Sound Generated Aerodynamically: I. General Theory"; Proceedings of the Royal Society of London, Series A: Mathematical and Physical Sciences, 211

Lighthill M. J., 1954, "On Sound Generated Aerodynamically: II. Turbulence as a source of sound"; Proceedings of the Royal Society of London, Series A: Mathematical and Physical Sciences, 222

Lilley G.M., 1995, "Jet Noise Classical Theory and Experiments"; in Aeroacoustics of Flight Vehicles, Vol. 1, Ed. H. H. Hubbard, Acoustical Society of America

Michalke A. and Fuchs H.V., 1975, "On turbulence and noise of an axisymmetric shear flow"; Journal of Fluid Mechanics, 70 (1)

Panchapakesan N.R. and Lumley J.L., 1993, "Turbulence measurements in axisymmetric jets of air and helium. Part 1. Air jet"; Journal of Fluid Mechanics, 246

Panchapakesan N.R. and Lumley J.L., 1993; "Turbulence measurements in axisymmetric jets of air and helium. Part 2. Helium jet"; Journal of Fluid Mechanics, 246

Pope S. B., 2000, "Turbulent Flows"; Cambridge University Press

Rajaratnam N., 1976, "Turbulent Jets"; Elsevier Publishing Co., Amsterdam and New York

Ribner H.S., 1964, "The Generation of Sound by Turbulent Jets"; Advances in Applied Mechanics Volume VIII, Academic Press, New York, London

Ribner H. S., 1981, "Perspectives on Jet Noise"; AIAA Journal, Vol. 19 No. 12, December

Ribner H.S., 1996, "Effects of jet flow on jet noise via an extension to the Lighthill model"; Journal of Fluid Mechanics Digital Archive, 321 (-1)

Romano G.P., Antonia R.A., 2001, "Longitudinal and transverse structure functions in a turbulent round jet: effect of initial conditions and Reynolds number"; Journal of Fluid Mechanics, 436

Ruppert-Felsot J., Farge M., Petitjeans P., 2009, "Wavelet tools to study intermittency: application to vortex bursting"; Journal of Fluid Mechanics, 636

So R.M.C., Zhu J.Y.Z., Otugen M.V., Huang B.C., 1990, "Some measurements in a binary gas jet"; Experiments in Fluids, 9

Tam C.K.W., Golebiowski M., Seiner J.M., 1996, "On the Two Components of Turbulent Mixing Noise from Supersonic Jets"; AIAA paper 96-1716

Tam C.K.W., 1998, "Jet Noise since 1952"; Theoretical and Computational Fluid Dynamics, 10

Tam C.K.W. and Aurialt L., 1999, "Jet Noise from fine-scale turbulence"; AIAA Journal, 37(2)

Tam C.K.W., Viswanathan K., Ahuja K.K., Panda J., 2008, "The sources of jet noise: experimental evidence"; Journal of Fluid Mechanics, 615

Tanna H.K., 1977, "An experimental study of jet noise"; Journal of Sound and Vibration, 50

Tinney C.E., Jordan P., 2008, "The near pressure field of co-axial subsonic jets"; Journal of Fluid Mechanics, 611

Trupel, 1976, for the Trupel observations see Rajaratnam 1976

Viswanathan K., 2004, "Aeroacoustics of hot jets"; Journal of Fluid Mechanics, 516

Viswanathan K., 2009, "Best practices for accurate measurement of pure jet noise", International Journal of Aeroacoustics

Weisgraber T. H., Liepmann D., 1998, "Turbulent structure during transition to self-similarity in a round jet"; Experiments in Fluids 24

Acknowledgments

Sono finalmente giunto ai ringraziamenti, una pratica dovuta e al contempo piacevole. Ho provato a scriverli in inglese ma avevano un sapore troppo formale, forse proprio per la mia limitata conoscenza della lingua. Quando si sente il bisogno di ringraziare qualcuno è già così difficile trovare le giuste parole nella propria lingua, figurarsi in un'altra.

In primis sento il bisogno di dire GRAZIE a mia madre e ai miei fratelli, a tutto il resto dei miei familiari e ai molti amici, perché, quando sono preso dagli impegni, non sono propriamente la persona più semplice da gestire. Grazie con tutto il cuore.

Un sentito grazie va al Prof. Roberto Camussi per i suoi consigli, la sua pazienza e la sua velocità nel correggere e adeguare il mio inglese maccheronico.

Sento di dover dedicare un pensiero e un abbraccio all'Ing. Daniele Grassucci, studente e collega ma soprattutto Amico. Grazie per le chiacchierate sulle wavelet e per tutto il resto.

Come non potrei ringraziare il Dott. Massimo Falchi e il Dott. Mario Felli? Colleghi rari da trovare. Grazie di tutto.

Un ringraziamento particolare va soprattutto all'Ing. Emiliano Binotti, collega da sempre. Ora come non mai un abbraccio e un ringraziamento ricordando "Sacco e Carro".

Un doveroso ringraziamento va anche al Dott. Fabio di Felice per il tempo che mi ha concesso per ultimare questo lavoro e a tutti i membri dell'unità scientifica.

Penso inoltre sia doveroso ringraziare i vari tesisti che, nel corso di questi tre anni, si sono alternati al mio fianco per studiare questo "Getto Rumoroso" e a tutti quelli che sono passati per il laboratorio anche solo per farsi due chiacchere. Grazie a: Silvia Volpe, Michele de Tullio, Valerio Fedele, Davide Marucci, Mauro Davoli e Danilo "Muffler" Tonelli.

Un grazie anche a tutti quelli che in un modo o nell'altro hanno reso piacevole quest'avventura. Grazie ad Alessandra, Mary, Alessandro, Max e a tutti quelli che ho dimenticato di nominare.